La Compil' des publications en 4 tomes

HAMID

Hamid Sadouki

Tome 3: Crack des fissures

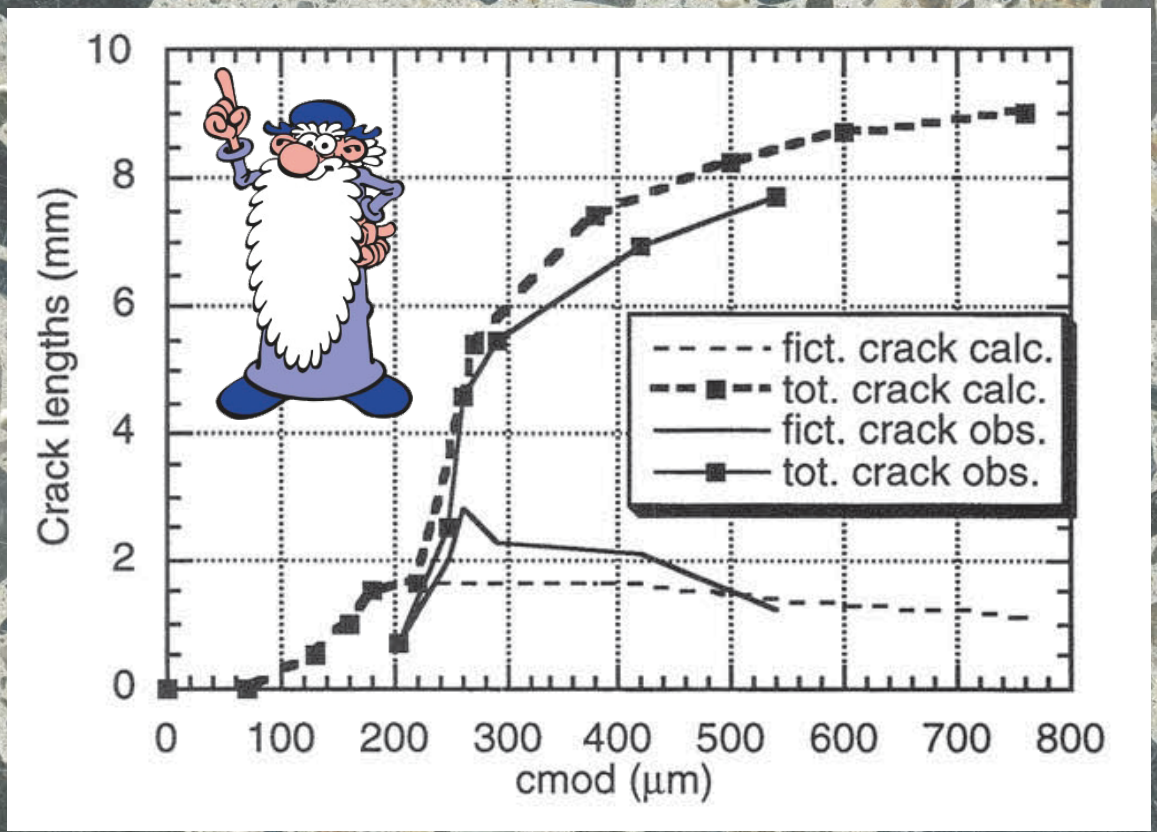

MCS éditions

Liste des publications

Tome 3 - Crack des fissures

1. Steiger T., Sadouki H., Wittmann F. H., 1995. Simulation and observation of the fracture process zone. *Fracture Mechanics of Concrete Structures (FRAMCOS-2)*, Aedificatio Publishers, Vol. I. 157-168.

2. Trunk B., Sadouki H., Wittmann F. H., 1995. Size effect and stability of fracture. *Fracture Mechanics of Concrete Structures (FRAMCOS-2)*, Aedificatio Publishers, Vol. I. 607-618.

3. Martinola, G., Sadouki, H., & Wittmann, F. H., 1996. Numerisches Modell zur Beschreibung der Eigenspannungen und der Rissbildung in Beschichtungssystemen. *Materials science and restoration IV*. 393-407.

4. Sadouki, H., Van Mier, J. G. M., 1997. Simulation of hygral crack growth in concrete repair systems. *Materials and Structures*, *30*(9): 518-526.

5. Martinola, G., Sadouki, H., 1998. Combined experimental and numerical study to assess shrinkage cracking of cement-based materials. *International journal for restoration of buildings and monuments*, 4: 479-506.

6. Sadouki H., Issifou Z., Wittmann F. H., 2000. Damage and Crack Formation in Wood under Mechanical Action. *Maintenance and Restrengthening of Materials and Structures - Wooden Structures*, Aedificatio Publishers. 47-54.

7. Martinola, G., Sadouki, H., Wittman, F.H., 2001. Numerical model for minimizing risk of damage in repair system. *ASCE Journal of Materials in Civil Engineering*, 13(2): 121-129.

8. Wittmann, F. H., Martinola, G., Sadouki, H., 2002. Material properties influencing early cracking of concrete. *Proc. Control of cracking in Early age concrete*, CRC Press. 3-18.

9. Ben Ftima, M., Sadouki, H., Brühwiler, E., 2016. Development of a computational multi-physical framework for the use of nonlinear explicit approach in the assessment of concrete structures affected by alkali-aggregate reaction. *Proc. 9th International Conference on Fracture Mechanics of Concrete and Concrete Structures FraMCoS-9*, DOI 10.21012/FC9.221.

Article n°1

SIMULATION AND OBSERVATION OF THE FRACTURE PROCESS ZONE

T. Steiger, H. Sadouki, and F.H. Wittmann,
Laboratory for Building Materials, Swiss Federal Institute of Technology
Zürich, Switzerland

Abstract
The determination of the extension of the fracture process zone in composite materials such as cement or polymer mortar is rather difficult. Non destructive techniques must be applied in order to observe the evolution of the deterioration of the material. Fracture tests carried out in an environmental scanning electron microscope allow us to observe the development of the fracture process zone and crack propagation under increasing load. The experimental results will be compared with results obtained by numerical simulation based on the fictitious crack model.

1 Introduction

Today the fictitious crack model (FCM) is widely used to predict crack formation in composite materials such as concrete. One basic assumption of this approach is the formation of a fictitious crack. It is assumed that within the fictitious crack depending on the the actual width, tensile forces can still be transmitted. So far few attempts exist to observe the existence of a fictitious crack in order to validate numerical predictions.

Knab (Knab et al. (1986)) has summarized some useful techniques which had been applied to observe the fracture process zone. Hu (1990,

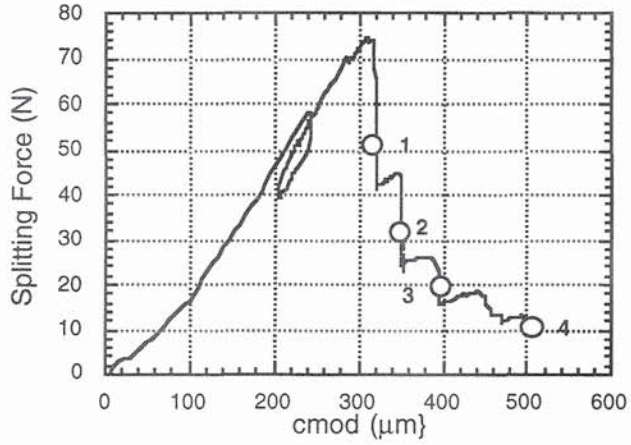

Fig. 2. Measured load-displacement curve of polymer mortar with points indicating the states at which micrographs of Fig. 4 have been taken

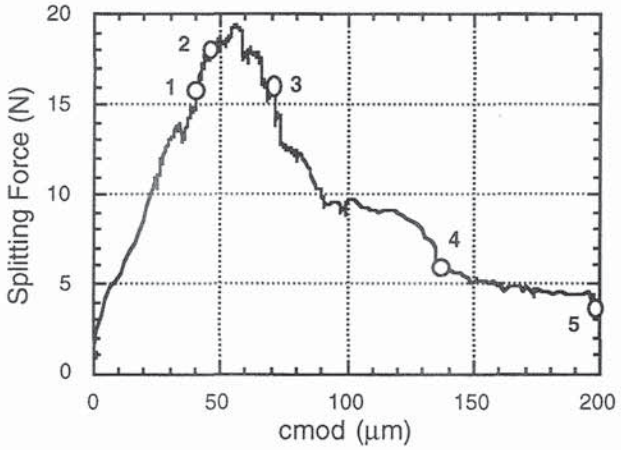

Fig. 3. Measured load-displacement curve of cement mortar with points indicating the states at which micrographs of Fig. 5 and Fig. 6 have been taken

3.2 Widening of the fictitious crack

To observe the widening of the fictitious crack in polymer mortar it was decided to follow the crack evolution at a point approximately 1.8mm apart from the notch tip. Immediately after the maximum in the force-displacement diagram had been passed a first photo is taken (Fig 2.1). A continuous crack can be observed. It is quite obvious that, per unit of length of the fictitious crack an average load can be transfered by the still existing bridges. A further stage of deterioration is marked with point 2 in Fig. 2. The corresponding opening is shown in Fig. 4.2. The micrographs shown in Fig. 4.3 and 4.4 correspond to the situation marked with 3 and 4 in Fig. 2

2.3 Preparation of specimens

We prepared mixes with two different types of binder: an epoxy resin hardener system and a portland cement. Crushed grains of a maximum size of 200μm were embedded in the cement and polymer mortar. For both mortars the volume concentration of aggregates was chosen to be 35%. This corresponds to the composition of fine mortar in concrete.

The specimens used to carry out in-situ experiments have been cast in standard moulds (160*160*40mm). With a diamond bladed saw the final geometry of the WOD-specimen (30*30*5mm) was cut. Using a special saw the notch was cut (notch width of 0.5mm). The ligament has a length of 10mm. In Fig. 1 the geometrical shape of the specimens is given.

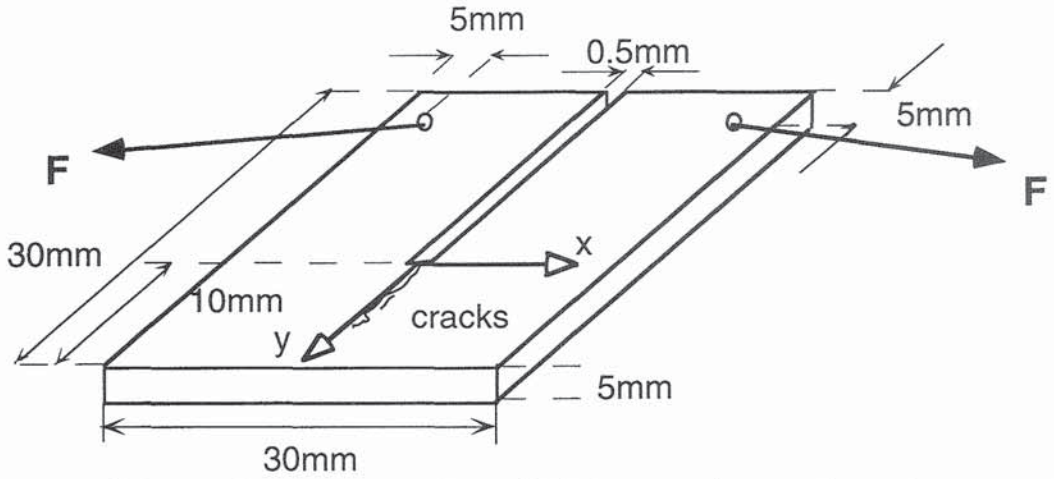

Fig. 1. Schematic representation of WOD-specimens for polymer and cement mortar

3 Experimental Results

3.1 Force-displacement diagrams

In Fig. 2 the force-displacement diagram of a polymer mortar as being tested under electron microscopical observation is shown. The indicated numbers point out the corresponding levels along the softening branch at which microphotos have been taken.

In Fig. 3 the equivalent force-displacement diagram as observed on cement mortar specimen is plotted. From these experimental results the fracture energy and the strain-softening relation have been determined by inverse analysis.

1993) has successfully applied the multi-cutting technique in order to determine the effective length of the fracture process zone. By optical interferometry Rastogi and Denarié (1994) have also observed the extension of the fracture process zone. A similar technique has been applied by Hack et al. (1995).

Mindess and Diamond (1980) and Diamond et al. (1983) were probably the first to observe crack formation directly in an electron microscope. In this way characteristic features along the crack path can be observed.

With the aim to observe mechanisms of load transfer and mechanisms of energy consumption in the fracture process zone and to quantitatively follow the evolution we carried out tests on polymer and cement mortar in an Environmental Scanning Electron Microscope (ESEM). We applied the load by a specially developed device which allows us to fracture specimens under wedge opening displacement (WOD). The experimental results should serve as a basis for comparison with results of numerical simulations. The numerical model used in this comparative study is based on the (FCM) according to Hillerborg et al. (1976).

2 Experimental set-up and preparation of specimen

2.1 Low vacuum scanning electron microscopy

The specimen chamber of the microscope is operated with a controlled environment (Danilatos and Robinson (1979)), while the optical column is kept under high vacuum. The relatively high gas pressure in the specimen chamber allows us to work without additional preparation of the surface (Ollivier (1985)). In this instrument non-conductive surfaces can be observed. During testing the specimen chamber was kept at about 1-2 Torr and about 25°C. The primary electrons were accelerated by 17keV in the case of the cement mortar specimens and 18 keV in the case of the polymer mortar specimens.

2.2 In-situ testing machine

Wedge splitting tests were run on a special in-situ testing machine mounted on a coordinate table in order to control the position of observation. The test device consists of a stiff frame to support the specimen and the loading wedge (wedge angle α=15°), a strain gauge and a load cell. Loading and unloading of the specimen is carried out by remote control. The position of the specimen is approximately kept constant due to a contrarotating system. The splitting force and the displacement were continuously recorded during testing.

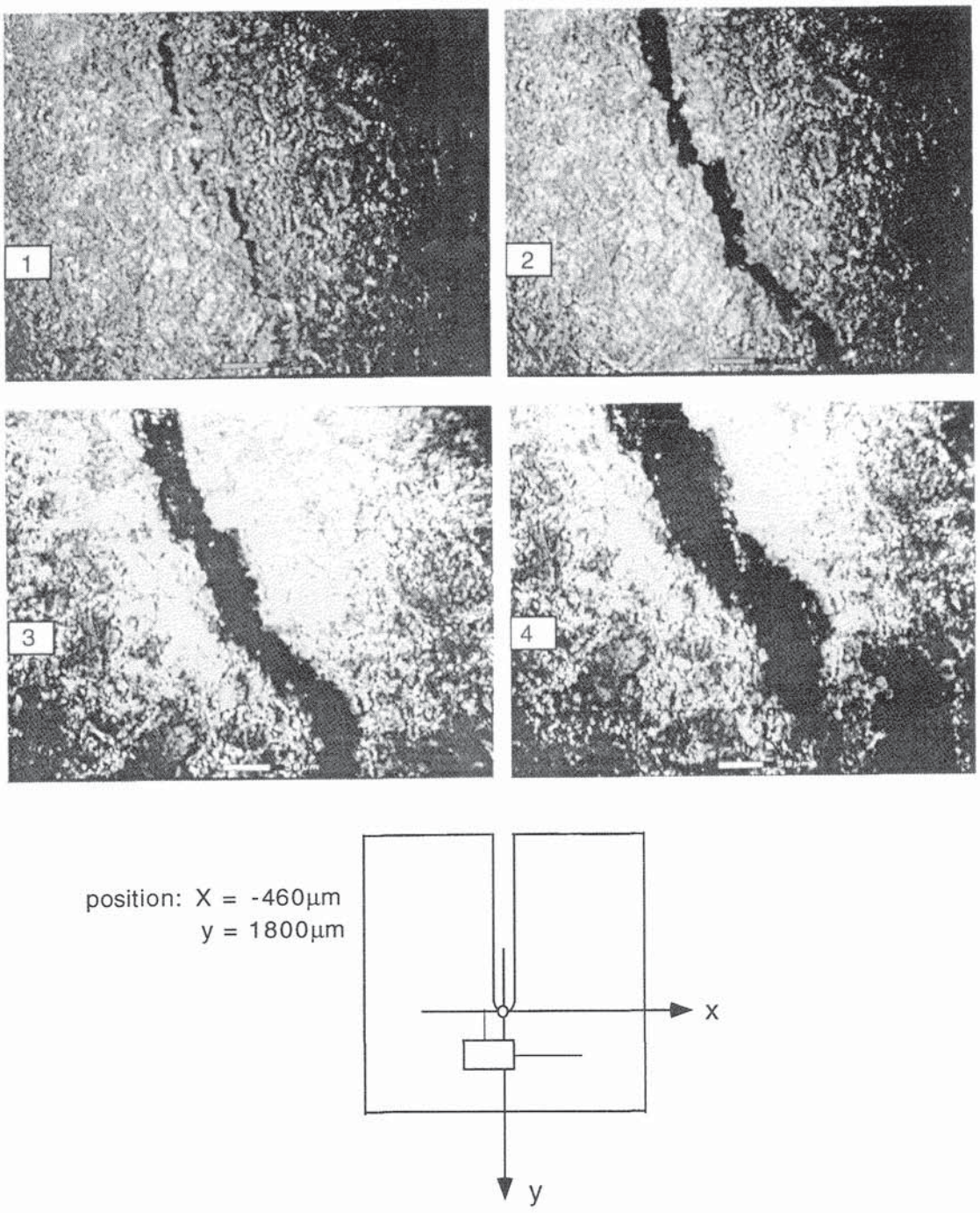

Fig. 4. Microphotos corresponding to load points 1 to 4 shown in the force-displacement diagram of Fig. 2

In Fig. 5 three different stages of crack formation in a cement mortar are shown. The corresponding points on the force-displacement diagram are marked with 1-3 in Fig. 3. In addition the crack width has been observed at a stage of higher damage (points 4 and 5). The place of observation and the micrographs are shown in Fig. 6.

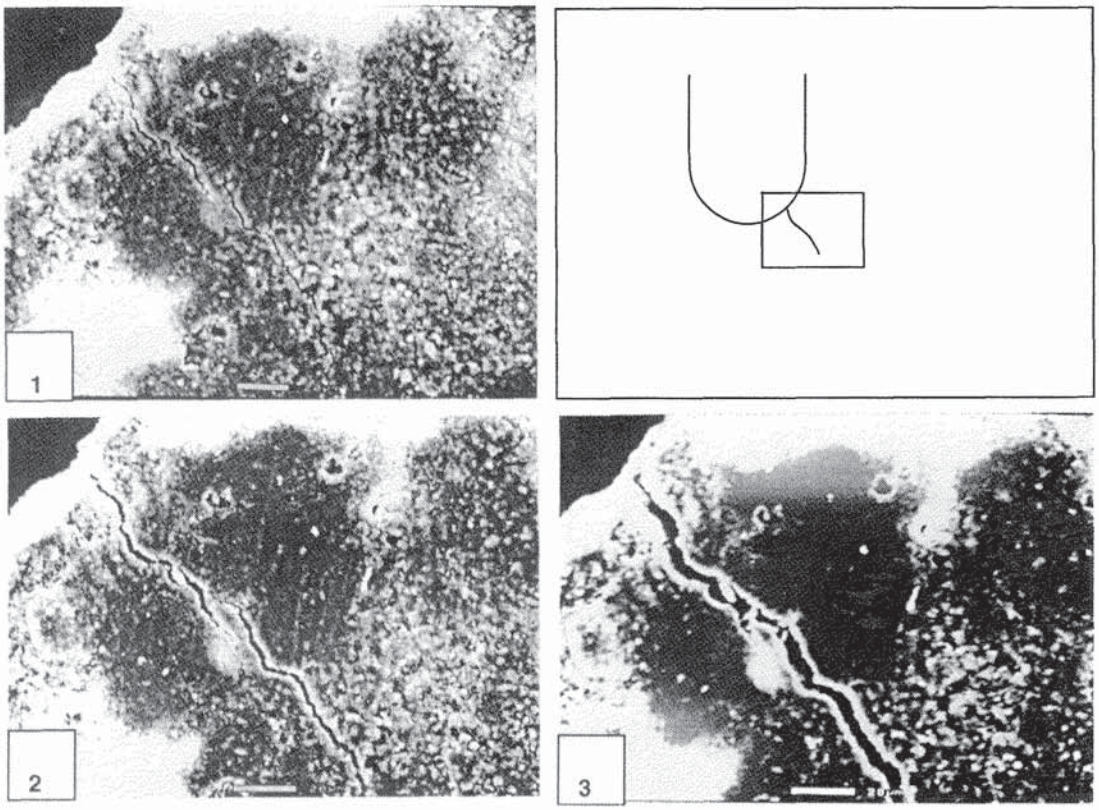

Fig. 5. Microphotos corresponding to load points 1 to 3 shown in the force-displacement diagram of Fig. 3

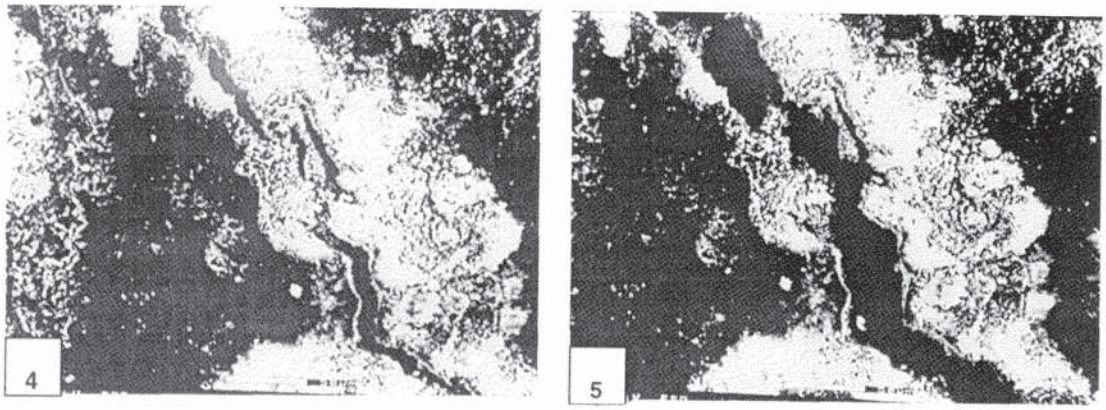

Microphotos corresponding to load points 4 and 5 shown in the force-displacement diagram of Fig. 3

3.3 Determination of crack length

In order to be able to determine the length of both the real and the fictitious crack, microphotos have been taken along an existing crack path. A typical example is shown in Fig. 7. The crack tip can be clearly seen. The transition from real to fictitious crack is located where no bridges can been seen any more.

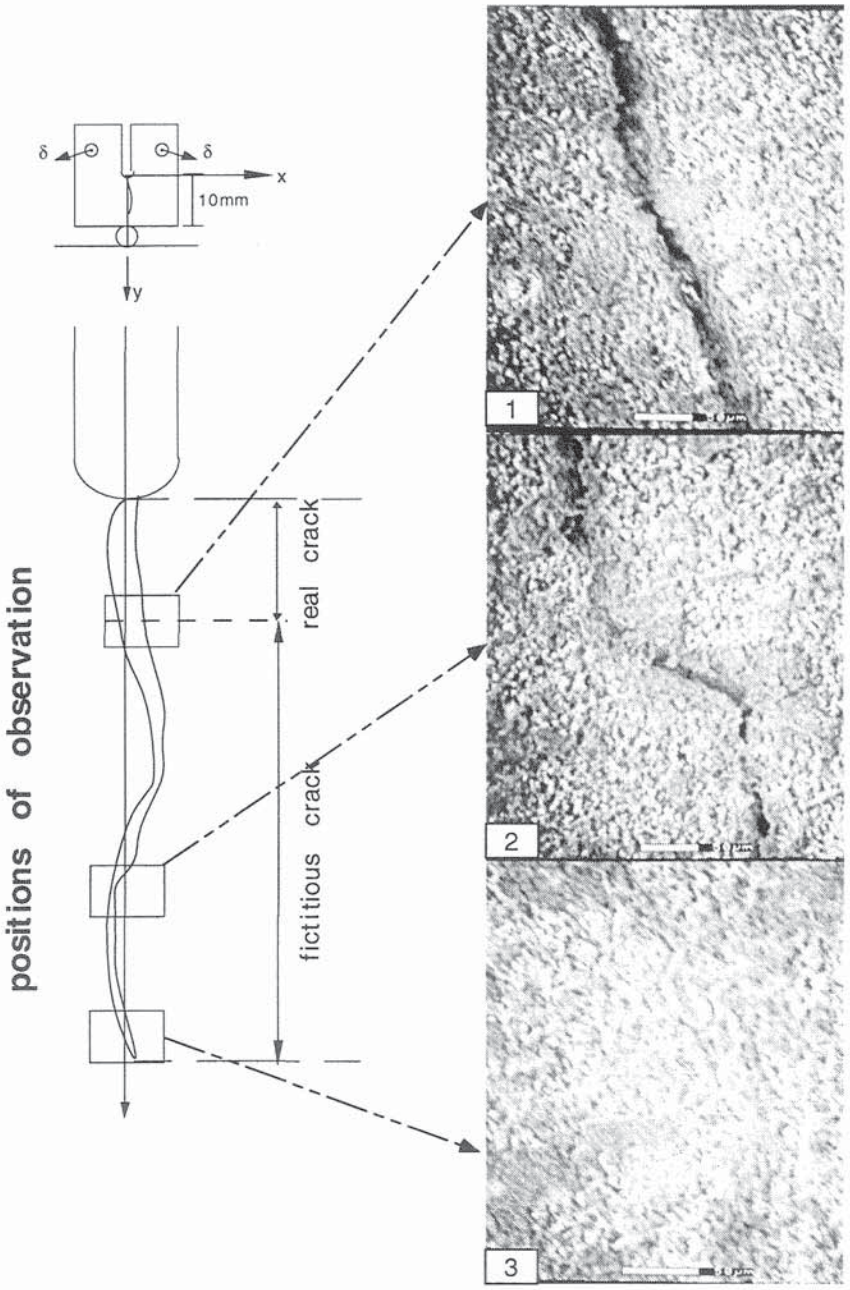

Fig. 7. Crack path with the transition from real to fictitious carck (1), an intermediate state (2) and the crack tip (3)

4 Numerical analysis and simulation

For the simulation of the formation of fictitious and real cracks we applied a cohesive crack model. The strain-softening behaviour is modelled by a bilinear curve defined by four material parameters (f_t, σ_1, w_1 and w_2). The area under the diagram is the fracture energy (G_f) given by the following equation:

$$G_f=0.5\ (f_t\ w_1+\sigma_1\ w_2) \qquad (1)$$

In principle the strain-softening diagram can be directly obtained by uniaxial tension tests, but these tests are often difficult to be performed. For that reason, the softening diagram is derived from load-displacement diagrams obtained on WOD-specimens combined with an adequate inverse analysis (Roelfstra and Wittmann (1986)). Table 1 gives the relevant mechanical properties obtained for polymer and cement mortar.

Table 1. Fracture energy and strain-softening parameters

Material	E N/mm^2	G_f N/m	f_t MPa	σ_1 MPa	w_1 mm	w_2 mm
polymer mortar	5000	237	16.8	1.83	0.025	0.03
cement mortar	20000	34	4	1.4	0.01	0.02

In order to take the heterogenous character of the composite material into account we introduced a statistical distribution of the Young's modulus E and the tensile strength f_t.

The numerical analysis of crack formation of a WOD specimen was performed by means of the customary non-linear FE-package MARC (MARC 1994). Linking a special user subroutine 'TENSOF' the numerical treatment of the cracking process is possible. The mesh generation is carried out automatically taking the realistic boundary conditions into account.

In Fig. 8 and Fig.9 the strain-softening curves of polymer and cement mortar are shown. This result can be used for the comparison with experimental results.

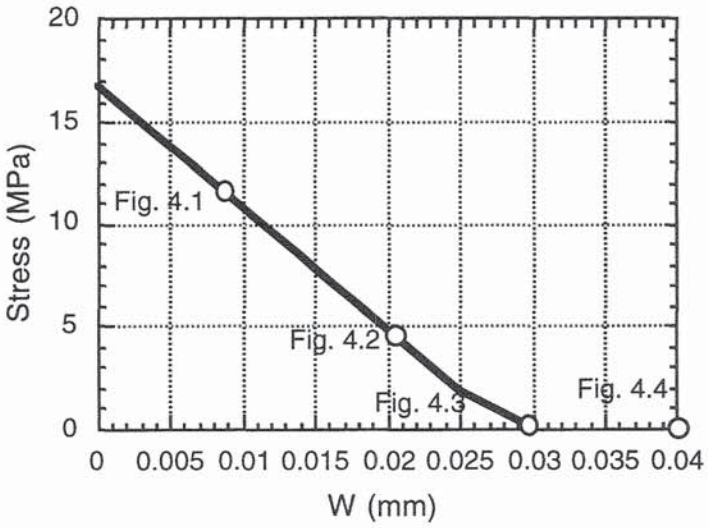

Fig. 8. Strain-softening of polymer mortar

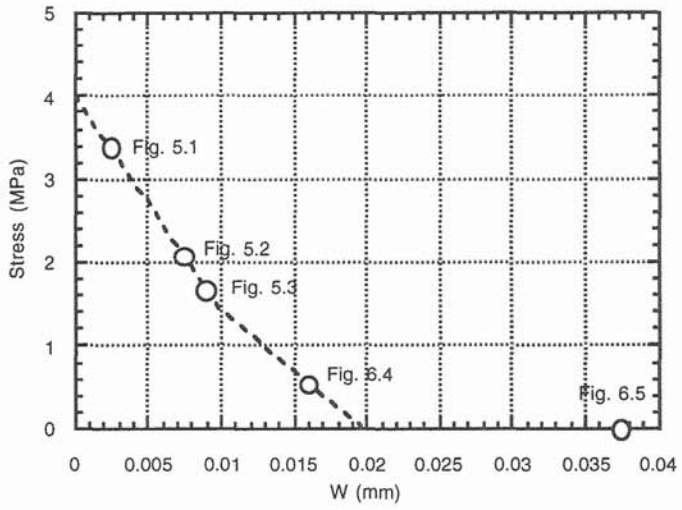

Fig. 9. Strain-softening of cement mortar

5 Comparison of experimental and numerical results and discussion

In Fig. 8 and Fig. 9 of the previous section the numerically determined strain-softening relations for polymer and cement mortar are shown. Along the descending branch the figures indicate the degree of damage which corresponds to the micrographs presented earlier. The points 4.1 and 4.2 for example correspond to the micrographs 1 and 2 shown in Fig. 4. In this way the degree of damage can be visualized.

The crack opening at a given point along the crack path has been calculated numerically by using the experimentally determined parameters. In Fig. 5 a typical example is shown. The crack opening

(fictitious and real) as numerically predicted is compared with observations in the ESEM. A fair agreement is found, as it can be seen in Fig. 10. In Fig. 11, it is not the width but the length of the fictitious and the total (fictitious and real) crack which are shown. Again a reasonable agreement can be observed. It must be stated, however, that this comparison is not yet based on a statistical evaluation of many cracks. Therefore this contribution has to be considered as an attempt to develop a new method for the validation of numerical predictions.

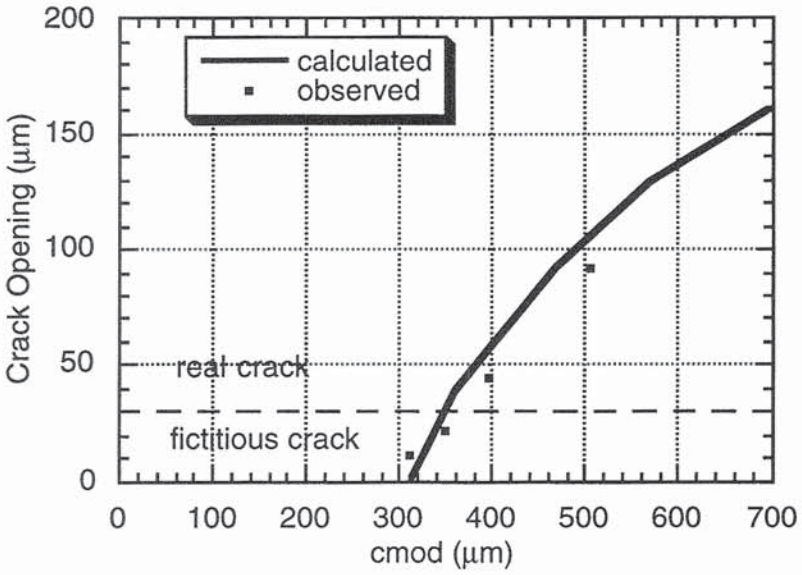

Fig. 10 Numerical and observed values of crack opening

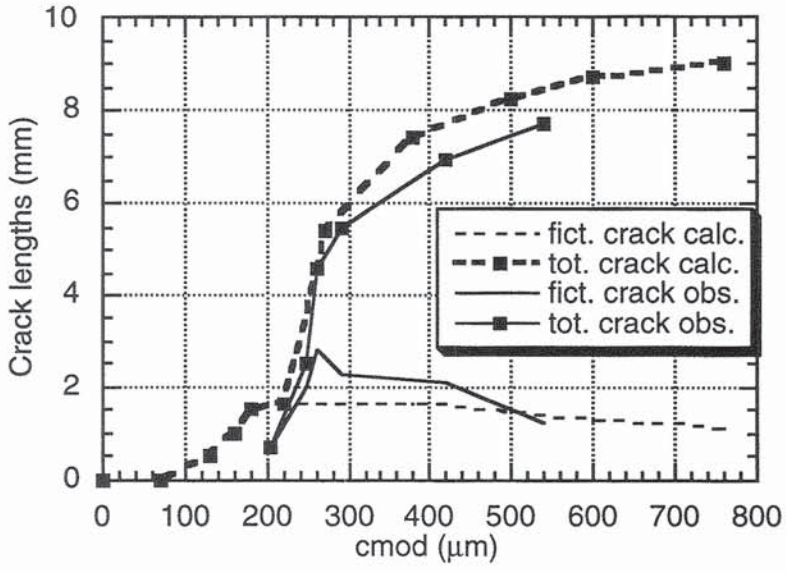

Fig. 11 Calculated and observed fictitious and total crack lengths

6. Conclusions

Basic assumptions of numerical models need to be experimentally verified. The extension, the width of the fictitious crack can be visualized by means of an electron microscopical observation. Results of a corresponding numerical simulation are in good agreement. This means that a numerical model based on the concept of the fictitious crack has a sound physical basis. The experimental results validate the main assumptions of the fictititous crack model.

The observation of the evolution of crack formation allows us to distinguish between different energy consuming mechanisms in the fictitious crack. Strain energy in remaining solid bridges, friction and interlocking all contribute to the energy consumption.

References

Danilatos, G.D, and Robinson V.N.E. (1979) Principles of scanning electron microscopy at high specimen chamber pressures, **Scanning**, 2:72-82

Diamond, S., Mindess, S, and Lovell, J. (1983) Use of a Robinson backscatter detector and "wet cell" for examination of wet cement paste and mortar specimens under load. **Cem. & Concr. Res.**, 13, 107-113

Hack, E., Steiger, T., and Sadouki, H. (1995) Application of electronic speckle pattern interferometry (ESPI) to oserve the fracture process zone, contribution to this volume.

Hillerborg, A., Modéer, M. and Petersson, P.E. (1976) Analysis of crack formation and crack growth in concrete by means of fracture mechanics and finite elements. **Cem. & Concr. Res.**, 6, 773-782.

Hu, X. (1990) Fracture process zone and strain-softening in cementitious materials, in **Building Materials Reports**, 1, AEDIFICATIO Publishers, Freiburg, Germany

Hu, X., and Wittmann, F.H. (1993) Characterisation of the fictitious crack with compliance measurements, in **Numerical Models in Fracture Mechanics of Concrete**, (ed. F.H. Wittmann), A.A. Balkema, Rotterdam, Brookfield.

Knab, L.I., Jennings, H., Walker, H.N., Clifton, J.R., and Grimes, J.W. (1986) Techniques to observe the fracture zone in mortar and concrete, in: **Fracture Toughness and Fracture Energy of Concrete** (ed. F.H. Wittmann), Elsevier,Amsterdam.

MARC Research Libary, Vol. C : Program Input. Marc Analysis Research Coorparation, Palo Alto (U.S.A.), 1994.

Mindess, S. and Diamond, S. (1980) A preliminary SEM study of crack propagation in mortar. **Cem. & Concr. Res.**, 10, 509-519

Ollivier, J.P. A non destructive procedure to observe the microcracks of concrete by scanning electron microscopy. **Cem. & Concr. Res.**,15, 1055-1060

Roelfstra, P.E. and Wittmann, F.H. (1986) Numerical Method to link strain softening with failure of concrete, in **Fracture Toughness and Fracture Energy of Concrete** (ed. F.H. Wittmann), Elsevier, Amsterdam.

Article n°2

Fracture Mechanics of Concrete Structures,
Proceedings FRAMCOS-2, edited by Folker H. Wittmann,
AEDIFICATIO Publishers, D-79104 Freiburg (1995)

SIZE EFFECT AND STABILITY OF FRACTURE

B. Trunk, H. Sadouki, and F.H. Wittmann,
Laboratory for Building Materials,
Swiss Federal Institute of Technology Zurich, Switzerland

Abstract

The effect of the specimen length on the tensile strength and on the stability of the fracture process in direct tension is investigated. Tests have been carried out on cylindrical specimens with a constant cross section but with different length. It was found that the tensile strength decreases with increasing specimen length. The influence of the strain softening behaviour on the stability of fracture is discussed.

1 Introduction

Tensile strength, specific fracture energy, and strain softening have proved to be material parameters which allow us to describe crack formation and propagation in concrete in a realistic way. Soon it was found, however, that these parameters depend on both specimen size and geometry. Weibull (1939) proposed a statistical theory that applies the weakest link concept to the strength of solids. Freudenthal (1968) linked this theory

with the Griffith crack instability criterion (Griffith (1921)). A stochastic theory for concrete fracture under different types of loading, in which, not only the stochastic characteristics of the process, but also the statistical stress distribution due to the material defects are taken into consideration was proposed by Mihashi and Masanori (1977) and Mihashi and Wittmann (1980). Another concept is the size-effect law proposed by Bazant (1983) that is applicable for geometrically similar structures of different size. It describes the transition from the strength theory, according to which failure occurs at a constant stress level, to the LEFM. The failure criterion is expressed in terms of the energy consumed per unit crack length. The multifractal scaling law as proposed by Carpenteri et al. (1993) and Carpenteri and Ferro (1994) is based on the assumption of multifractality for the damaged microstructure of the material. However, all these models do not consider the limit of stability.

For practical applications a clear distinction must be made between stable and unstable failure. Direct tension tests with the same cross section but different specimen length were carried out to determine the limit of stable fracture.

2 Background

In order to characterize the ductility of a material Petersson (1981) introduced a characteristic length l_{ch} and a critical length l_{crit} as material parameters:

$$l_{ch} = \frac{E \cdot G_f}{f_t^2} \quad \text{and} \quad l_{crit} = 2 \cdot l_{ch} = \frac{2 \cdot E \cdot G_f}{f_t^2} \tag{1}$$

When the maximum load in direct tension is reached and the elastic strain energy stored in the specimen exceeds the capability of energy consumption of the fracture process zone, the material will fail in a brittle way. This means that in a specimen with a constant cross section and a length of $2 \cdot l_{ch}$ brittle failure will occur. The stability limit given by eq. 1 is based on the assumption that the loading system is infinite stiff.

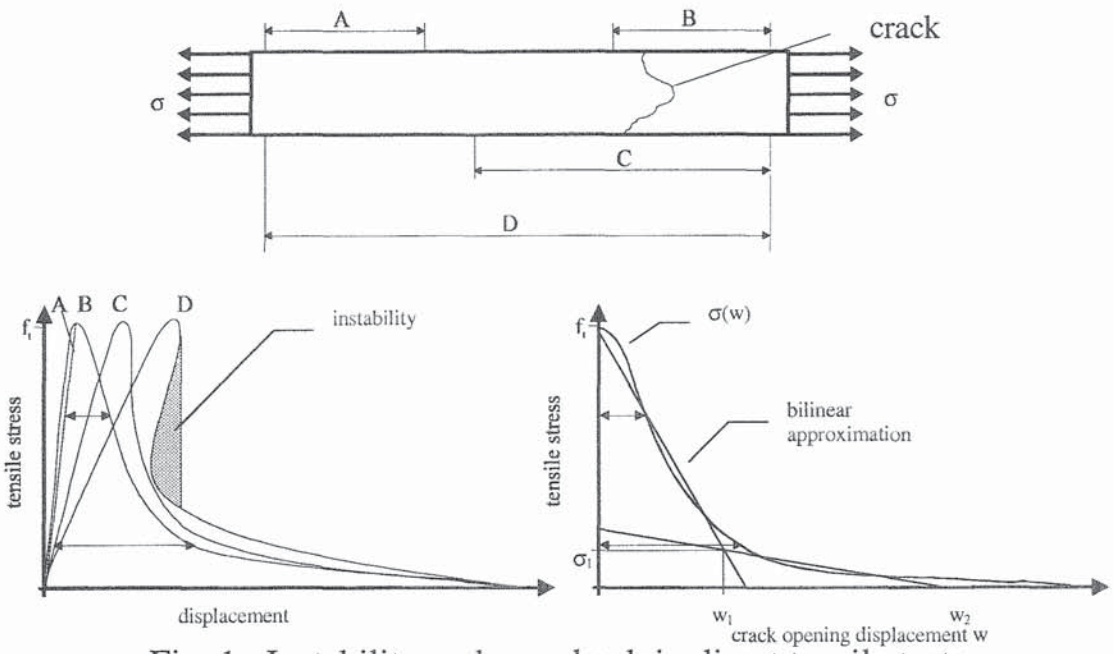

Fig. 1. Instability and snap back in direct tensile tests

We can assume that instability will occur when the slope of the softening diagram is equal or greater than the stiffness of the total loading system. Fig. 1 illustrates a direct tension test. The displacement is recorded by the four displacement transducers A, B, C and D. In the critical state when the slope of the decreasing part of the stress displacement diagram tends towards minus infinity the material will fail in a brittle way (displacement transducers C). The corresponding specimen length is called the critical length l_{crit}^*. For a known softening diagram $\sigma(w)$ (see Fig 1) as obtained from a stable test and an infinite stiff loading system the critical length l_{crit}^* can be calculated by eq. 2:

$$l_{crit}^* = \frac{E}{\left.\frac{\partial \sigma(w)}{\partial w}\right|_{\min}} \tag{2}$$

Where E is the modulus of elasticity of the specimen and w the crack opening displacement. If we assume a bilinear softening diagram (see Fig. 1) eq. 2 can be rewritten as:

$$l_{crit}^* = \frac{E \cdot w_1}{f_t - \sigma_1} \tag{3}$$

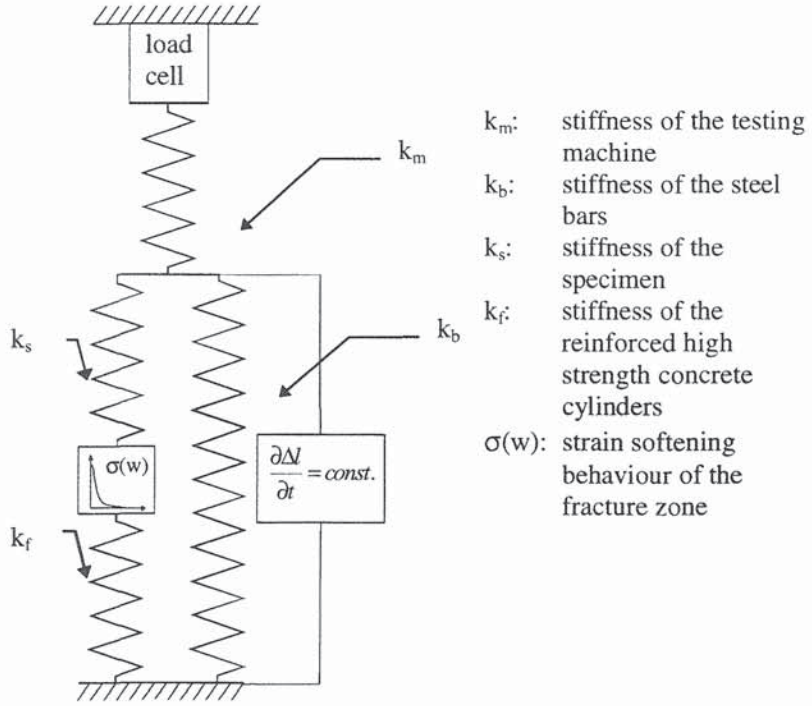

Fig. 2. Schematic illustration of the direct tension test with parallel stretched steel bars

For direct tension tests Petersson (1981) proposed among others not only the use of a stiff testing machine but also the use of steel bars attached parallel to the specimen to increase the stiffness of the total loading system. In Fig. 2 the schematic illustration of the direct tension test set-up used in this project is shown. The specimen load $F_s(\Delta l)$ can be determined from the measured load $F_m(\Delta l)$, the displacement Δl, and the stiffness of the steel bars k_b by the following equation:

$$F_s(\Delta l) = F_m(\Delta l) - k_b \cdot \Delta l \tag{4}$$

The crack opening w after peak load can be calculated by the following equation:

$$w = \Delta l - \frac{k_s + k_r}{k_s \cdot k_r} \cdot F_s(\Delta l) \tag{5}$$

Where $\frac{k_s + k_r}{k_s \cdot k_r} \cdot F_s(\Delta l)$ represents the displacement of the undamaged parts of the specimen and the reinforced high strength concrete cylinders.

To determine the critical length l_{crit}^{m} using the finite stiff loading system shown in Fig. 2 the critical length l_{crit}^{*} (see eq. 2) must be corrected by the following terms according to Petersson (1981):

$$l_{crit}^{m} = l_{crit}^{*} - \frac{E_s \cdot A}{k_b + k_m} - \frac{E_s}{E_f} \cdot l_f \tag{6}$$

Where E_s is the modulus of elasticity and A the cross section of the specimen, E_f the modulus of elasticity of the high strength concrete, and l_f the length of the reinforced high strength concrete cylinders. To determine the critical length l_{crit}^{*} from the test data eq. 6 leads to the following correction factor l_{corr} that represents an additional virtual specimen length:

$$l_{corr} = \frac{E_s \cdot A}{k_b + k_m} + \frac{E_s}{E_f} \cdot l_f \tag{7}$$

Fig. 3 shows the correction factor as a function of the stiffness of the total loading system for a specimen diameter of 100 mm and a Young's modulus of 40000 N/mm^2. The length of the reinforced high strength concrete cylinders is neglected.

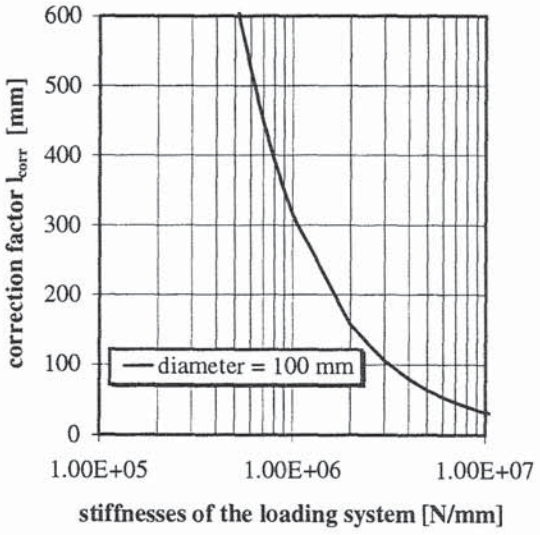

Fig. 3. Correction factor as a function of the stiffness of the loading system for a specimen diameter of 100 mm according to eq. 7

3 Experiments and results

3.1 Test set-up

The aim was to load cylindrical specimens with different length in a uniaxial direct tensile test. To achieve a homogeneous uniaxial stress distribution all over the specimen it was necessary to avoid stress concentrations at the loading interface. The attachments to the loading machine have to be restrained against rotation. Otherwise the post peak path of the load deflection curve bifurcates (Bazant et al. (1993)). However, due to the relative brittleness of concrete a very stiff testing machine has to be used for determining the strain softening behaviour (Petersson (1981)).

The test specimens were glued to reinforced high strength concrete supporting cylinders with approximately the same contraction of the endface to avoid shear stresses. Both, the specimen and the high strength concrete cylinders, have the same diameter. An epoxy resin based bicomponent adhesive was chosen. The reinforced high strength concrete cylinders were glued into flanged fittings as shown in Fig. 4. Here the same adhesive was chosen. The flanged fittings were screwed on steel supporting plates for rotational stiff attachment to the testing machine.

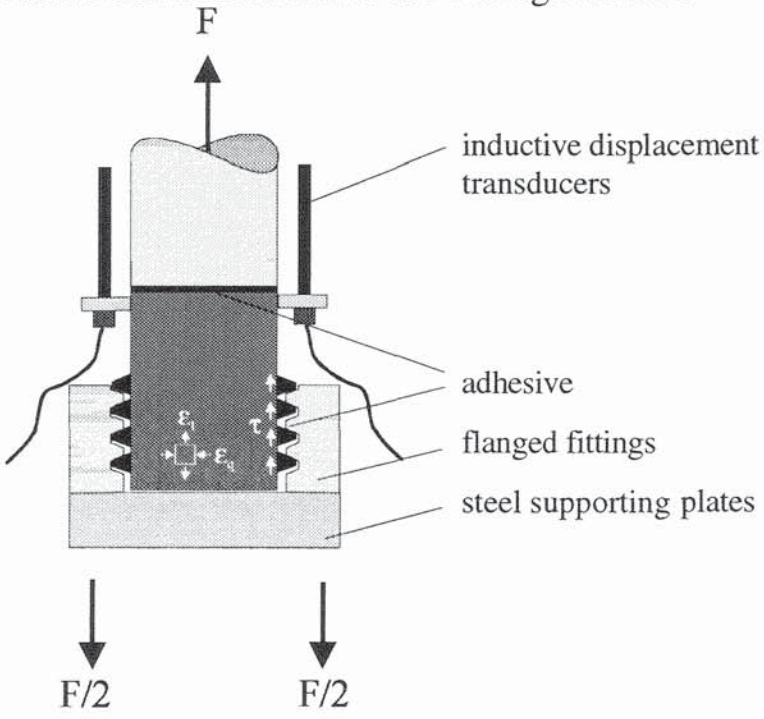

Fig. 4. Specimen bearing for direct tensile tests

Fig. 5 shows the set-up for the direct tensile tests. Steel bars were attached parallel to the specimen in order to increase the stiffness of the

machine. The tests were run under displacement controlled conditions $\partial \Delta l / \partial t = const.$ using a servo-hydraulic testing machine.

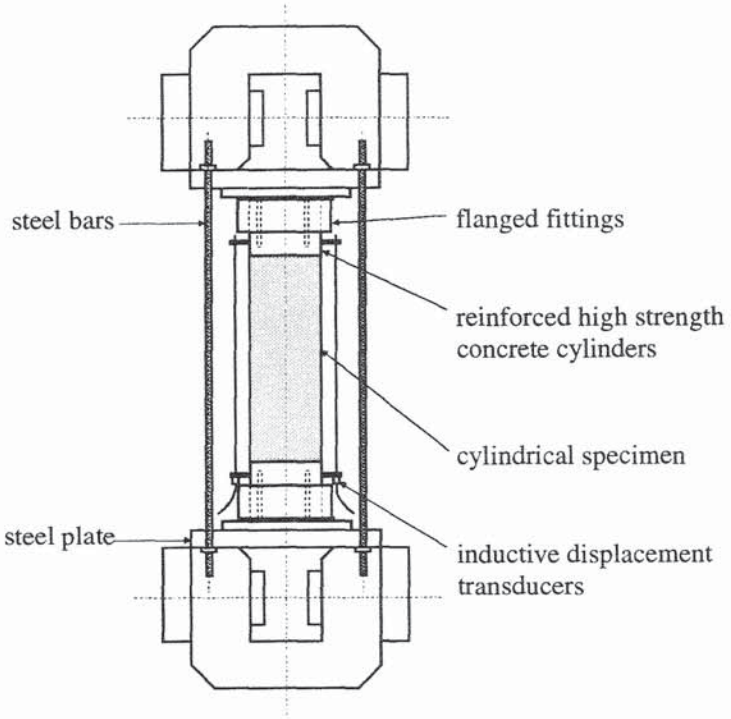

Fig. 5. Set-up for direct tension tests with a servo-hydraulic testing machine

3.2 Preparation of specimens

The concrete used for casting the specimens was made with a maximum grain size of 32 mm, a cement content of 300 kg/m^3 and a water/cement ratio of 0.5. The resulting compressive strength after 28 days was 49.7 N/mm^2, the modulus of elasticity was 38800 N/mm^2 and the density 2430 kg/m^2. The specimens were stored three and a half years at 70 % relative humidity and 20 °C. The diameter of the specimens was kept constant at 100 mm and the length varied between 50 and 400 mm.

3.3 Results

Direct tension tests were carried out in order to determine the material fracture mechanics parameters and the critical length of stability of fracture. The mean stress-displacement curves for stable tests and all curves for the instable tests are shown in Fig. 6. The results of the tests are summarized in Table 1.

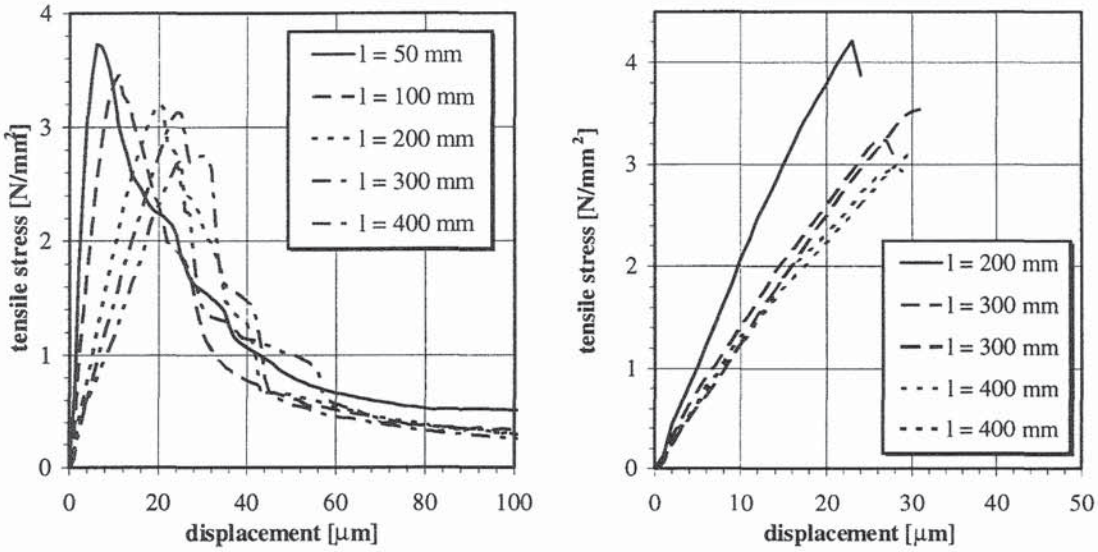

Fig. 6. Stable and unstable stress-displacement curves as observed in direct tension tests

Table 1. Test results

specimen length [mm]	50	100	200	300	400
tensile strength f_t [N/mm^2]	3.82	3.58	3.55	3.44	2.95
fracture energy [N/m]	220	170	160	140	170
number of stable tests	2	3	3	2	1
number of unstable tests	0	0	1	2	2

4 Evaluation of results and discussion

Fig. 7 shows the experimental softening curves and the bilinear approximation. In Table 2 the bilinear fracture mechanics parameters as determined from all stable tests are given. The parameters of the approximation were obtained by a non-linear least square fit. In Table 2 the characteristic and the critical length l_{ch} and l_{crit} calculated by eq. 1 and the critical length l_{crit}^* calculated by eq. 3 are given in addition.

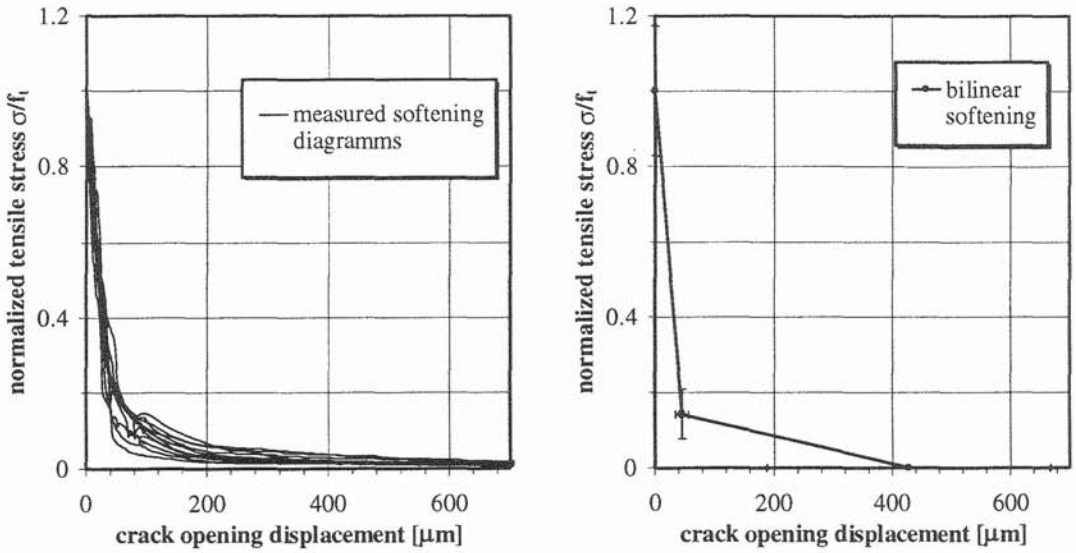

Fig. 7. Experimental softening curves and bilinear approximation

Table 2. Fracture mechanics parameters

Bilinear softening				characteristic and critical lengths		
f_t [N/mm^2]	σ_1 [N/mm^2]	w_1 [mm]	w_2 [mm]	l_{ch} [mm]	l_{crit} [mm]	l_{crit}^* [mm]
3.12	0.44	0.046	0.428	568	1136	597

The values of the measured tensile strength f_t are plotted in Fig. 8 against the specimen length. In accordance with the Weibull theory, tensile strength decreases with increasing specimen length. Under simplifying assumptions the following expression can be obtained from Weibull theory:

$$\left(\frac{f_t}{f_{t,0}}\right) = \left(\frac{l_0}{l}\right)^{\frac{1}{m}} \tag{8}$$

The parameters in eq. 8 have been determined by a least square fit to be:

$m = 11.8$

$l_0 = 50$ mm

$f_{t,0} = 3.82$ N/mm^2

The probability for brittle fracture as a function of the corrected specimen length calculated by eq. 7 is shown in Fig. 9.

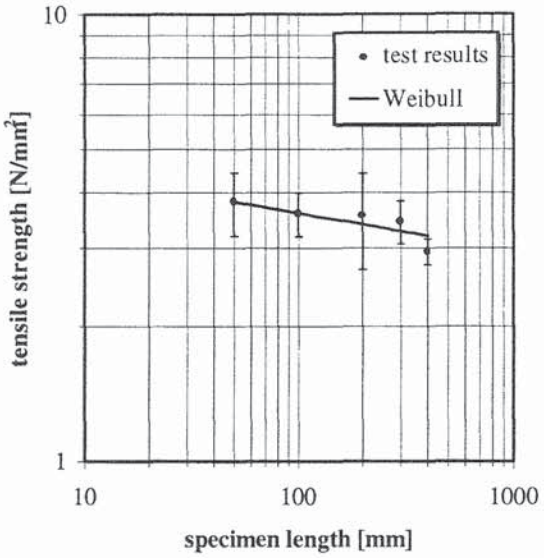

Fig. 8. Tensile strength as function of length

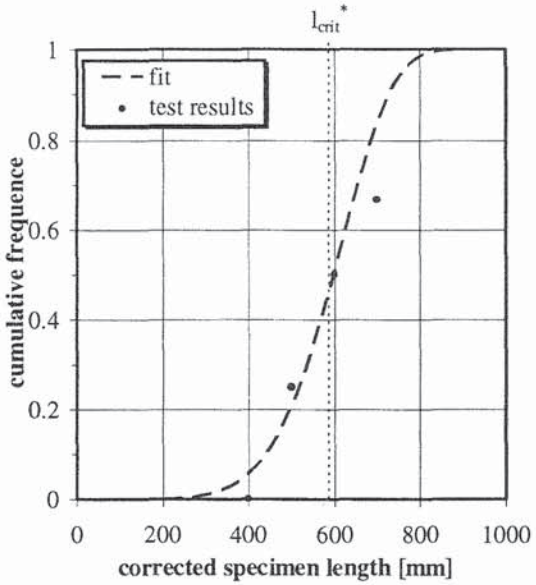

Fig. 9. Cumulative distributioßn for instability

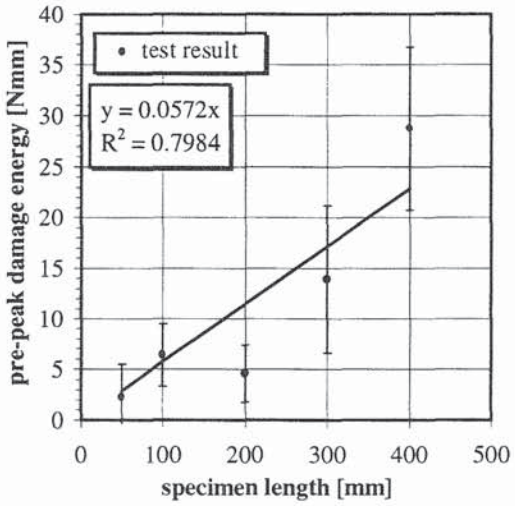

Fig. 10. Pre-peak damage energy as function of the specimen length

The pre-peak damage energy G_p introduced by Sadouki (1995) also increases with increasing specimen volume (i.e. length). To eliminate the influence of the differing tensile strength the pre-peak damage energy is calculated for each specimen length by using a stress corresponding to the lowest mean tensile strength (l = 400 mm). The results are shown in Fig. 10. The dependence on the specimen length can be described by the following linear function:

$$G_p = k \cdot l \tag{9}$$

with k = 0.0572 N, G_p is the pre-peak damage energy, and l the specimen length. It can be assumed, that within the experimental scatter the pre-peak damage energy is homogeneously distributed all over the specimens volume.

5 Conclusions

It has been shown that the critical length l_{crit} not only depends on the fracture energy G_f the tensile strength f_t and the modulus of elasticity E, but also on the shape of the softening diagram. That means, that the slope at the inflection point of the strain softening diagram is responsible for the stability of crack propagation. The slope of the first branch of the bilinear diagram can be used as a first approximation. The specimen length not only influences the stability but also the tensile strength and the pre-peak damage energy.

References

Bazant, Z.P. (1984) Size effect in blunt fracture: concrete, rock, metal. **Journal of Engineering Mechanics**, 110 (4), 518 - 535.

Bazant, Z.P. and Cedolini, L. (1993) Why direct tension test specimens break flexing to the side. **Journal of Structural Engineering**, 119 (4), 1101 - 1113.

Carpinteri, A., Chiaia, B., and Ferro, G. (1993) Multifractal scaling law for the nominal strength variation of concrete structures, in **Size effect in concrete structures**, Sendai, Japan, 173 - 186.

Carpinteri, A. and Ferro, G. (1994) Size effect on tensile fracture properties: a unified explanation based on disordered fractality of concrete microstructures. **Materials and Structures**, 27, 563 - 571.

Freudenthal, A.M. (1968) Statistical approach to brittle fracture, in **Fracture** (ed. H. Libowitz), 2, Academic Press, New York, 591 - 619.

Griffith, A.A. (1921) The phenomena of rupture and flow in solids. **Phil. Trans. R. Soc.**, 221, London, 163 - 198.

Mihashi, H. and Masanori, I. (1977) A stochastic theory for concrete fracture. **Cement and Concrete Research**, 7, 411 - 422.

Mihashi, H. and Wittmann, F.H. (1980) Stochastic approach to study the influence of rate of loading on strength of concrete. **Heron**, 25 (3).

Petersson, P.E. (1981) Crack growth and development of fracture zones in plain concrete and similar materials. Report TVBM-1006, Lund Institute of Technology, Lund, Sweden.

Sadouki, H. and Wittmann, F.H. (1995) Numerical concrete applied to investigate size effect and stability of crack propagation, in this volume.

Weibull, W. (1939) A statistical theory of strength of materials, Swedish Royal Institute for Engineering, 151, Stockholm, 591 - 619.

Article n°3

4. Internationales Kolloquium
Werkstoffwissenschaften und Bauinstandsetzen
Technische Akademie Esslingen, 17.-19. Dez. 1996

Numerisches Modell zur Beschreibung der Eigenspannungen und der Rissbildung in Beschichtungssystemen

G. Martinola, H. Sadouki und F.H. Wittmann
Institut für Baustoffe, ETH Zürich

Zusammenfassung
Wenn eine zementgebundene Beschichtung auf einen Betonuntergrund aufgetragen wird, bildet sich ein komplexer Eigenspannungszustand aufgrund hygrischer und thermischer Gradienten. Im vorliegenden Beitrag werden die theoretischen und numerischen Grundlagen eines Modells vorgestellt, das in der Lage, ist die Mechanik solcher Beschichtungssysteme zu berechnen. Die zeitabhängige Feuchtigkeitsverteilung wird mit Hilfe der nichtlinearen Diffusionstheorie beschrieben. Bei der folgenden Spannungs- und Verformungsanalyse wird das endogene Schwinden und das Trocknungschwinden, das Kriechen und die Rissbildung mit der nichtlinearen Bruchmechanik berücksichtigt. Mit diesem Modell können die relevanten Kenngrössen für die Bemessung solcher Beschichtungsysteme bestimmt werden.

A numerical model for the description of the eigenstresses and the crack formation in coating systems

Abstract
The application of a cement - based overlay on a concrete substrate leads to the formation of a complex state of eigenstresses due to hygral and thermal gradients. In this contribution the theoretical and numerical elements of a model are presented with the aim to calculate the mechanical behaviour of such coating systems. The non-linear diffusion theory is applied to describe the time dependent humidity distribution. Crack formation and delamination are predicted by means of non-linear fracture mechanics. The formation and growth of cracks is considered with a combination of discrete and smeared crack models. This model allows us to determine quantities which are relevant for the design of such coating systems.

1 Einleitung

Das Aufbringen von Mörtel oder Neubeton auf Beton ist bei einer Instandsetzung von beschädigten Bauwerken ein besonders heikles und aktuelles Problem. Üblicherweise werden solche Probleme empirisch und nicht systematisch ingenieurmässig angegangen. Im Rahmen dieser Arbeit wird das Verhalten vom System Beschichtung-Betonuntergrund unter hygrischer Beanspruchungen untersucht. Da diese Problemstellung sehr komplex ist, wird ein nichtlineares Finite Elementen Modell verwendet. Die Messungen von hygrischen und mechanischen Eigenschaften an verschiedenen Reparaturmörteln dienen als Basis für eine realistische Spannungsanalyse.

Die Grundlage für die physikalische und numerische Beschreibung eines solchen Systems wurde schon in [1] ausführlich beschrieben. Im Vergleich zum Modell, das in [1] beschrieben wurde, werden in diesem Beitrag neue konstitutive Werkstoffgesetzte implementiert. Die Grenzfläche Mörtel - Untergrundbeton wird nicht mehr mit zweidimensionalen Elementen sondern mit Grenzflächenelementen modelliert (diskretes Rissmodell). Es hat sich gezeigt, dass das hier benutzte FE-Programm DIANA [2] geeignet ist, solche komplexe Probleme realistisch zu lösen [3,4]. Die Rissentstehung und Ausbreitung im Mörtel und im Untergrundbeton wird mit dem Modell der verschmierten Risse simuliert [5,6]. Für die Berechnung der Feuchtigkeitsverteilung wird auch die endogene Trocknung berücksichtigt. Der Diffusionskoeffizient ist abhängig vom Mörtelalter. Die Abhängigkeit des hygrischen Ausdehnungskoeffizienten von dem Feuchtigkeitspotential wird mit einer Gaussfunktion beschrieben. Das viskoelastische Verhalten des Systems wird mit einer Serie von Kelvinketten simuliert, die unter anderem das Grund- und Austrocknungskriechen berücksichtigen.

2 Realistische Beschreibung des Werkstoffverhaltens

2.1 Werkstoffgesetzte

2.1.1 Hygrisches Verhalten

Zementgebundene Werkstoffe sollten idealerweise nach dem Ausschalen mit einer relativen Luftfeuchtigkeit von etwa 100% umgeben werden. Meistens sind sie aber Luft mit einer deutlich niedrigeren relativen Feuchtigkeit ausgesetzt. So beginnt häufig unmittelbar nach dem Ausschalen ein langanhaltender Austrocknungsprozess.

Das Austrocknen und die damit verbundene zeitabhängige Feuchtigkeitsverteilung im Bauteil lassen sich mit Hilfe einer Diffusionsgleichung gut beschreiben [7]. Hierbei muss beachtet werden, dass der Feuchigkeitstransportkoeffizient stark vom Feuchtigkeitsgehalt abhängig ist. Dies hat zur Folge, dass die Diffusionsgleichung durch einen feuchtigkeitsabhängigen Diffusionskoeffizient nichtlinear wird.

$$\dot{h} = div\left[D(h) \cdot \vec{grad}(h) \right] + q(t) \qquad (1)$$

Die in Gl. (1) benutzten Symbole bedeuten :

h :	Feuchtigkeitspotential
$D(h)$:	Feuchtigkeitsdiffusionskoeffizient, abhängig von h
$q(t)$:	Feuchtigkeitssenke, die eine innere chemische endogene Austrocknung des jungen Werkstoffes beschreibt

Für die Gleichung (1) gelten die folgenden Rand - und Anfangsbedingungen :

$$q_s = H_f \cdot (h_s - h_a) \tag{2}$$

mit

h_s : Feuchtigkeitspotential an der Oberfläche bei Kontakt mit der Umgebungsluft

h_a : Feuchtigkeitspotential der umgebenden Atmosphäre

H_f : Feuchtigkeitübergangskoeffizient zwischen Werkstoff und Umgebung

Dieser Koeffizient H_f ist stark abhängig von verschiedenen Faktoren, wie z.B. Temperatur, relative Luftfeuchtigkeit, und Strömungsgeschwindigkeit der Umgebungsluft

$$h(t = 0, x_i, y_i, z_i) = h_i \tag{3}$$

h_i : Feuchtigkeitspotential im Punkt (x_i, y_i, z_i) zu Beginn des Austrocknungsprozesses

Durch eine Änderung Δh des Feuchtigkeitspotential in einem hypothetischen finiten Volumen des trocknenden Werkstoffes wird eine hygrische Dehnung hervorgerufen. Dieser Mechanismus kann durch folgenden Ausdruck formuliert werden :

$$\Delta\varepsilon_{h.Sch.} = \alpha_{h.Sch.}(h) \cdot \Delta h \tag{4}$$

$\Delta\varepsilon_{h.Sch.}$ ist die infinitesimale hygrische Schwindverformung, Δh ist die Änderung des Feuchtigkeitspotentials und $\alpha_{h.Sch.}(h)$ ist der hygrische Ausdehnungskoeffizient. Der hygrische Ausdehnungskoeffizient ist stark vom Feuchtigkeitsgehalt abhängig. Wird das externe oder interne hygrische Schwinden des Werkstoffes behindert, so entstehen Spannungen.

2.1.2 Mechanisches Verhalten

Das mechanische Verhalten eines zementgebundenen Werkstoffes kann in realistischer Weise durch ein Elasto - Entfestigungsmodell wie das kohäsive Rissmodell von Hillerborg et al. beschrieben werden [8]. Das Versagen der Grenzfläche wurde mit dem diskreten Rissmodell modelliert. Für den Mörtel und den Untergrundbeton wurde das "multi-directions fixed smeared crack model" eingesetzt [2,5].

Im implementierten konstitutiven Modell wird das gesamte Verformungsfeld ε in elastische und riss- , kriech- und feuchtigkeitabhängige Komponenten zerlegt:

$$\varepsilon = \varepsilon^{El.} + \varepsilon^{Ris.} + \varepsilon^{Krie.} + \varepsilon^{h.Sch.} \tag{5}$$

Die Komponenten $\varepsilon^{h.Sch.}$ und $\varepsilon^{Krie.}$ sind zeitabhängig, die erste Komponente wird von der Feuchteänderung beeinflusst (Gl. 4), die zweite ist von der Spannungsgeschichte abhängig.

Das Spannungs - Dehnung Diagramm in Zugrichtung des Kontinuums besteht aus einem linear elastischen Teil, charakterisiert durch Elastizitätsmodul und Zugfestigkeit. Das „post-peak" Verhalten ist vom Entfestigungsdiagramm und der Bruchenergie abhängig (Abb. 1a).

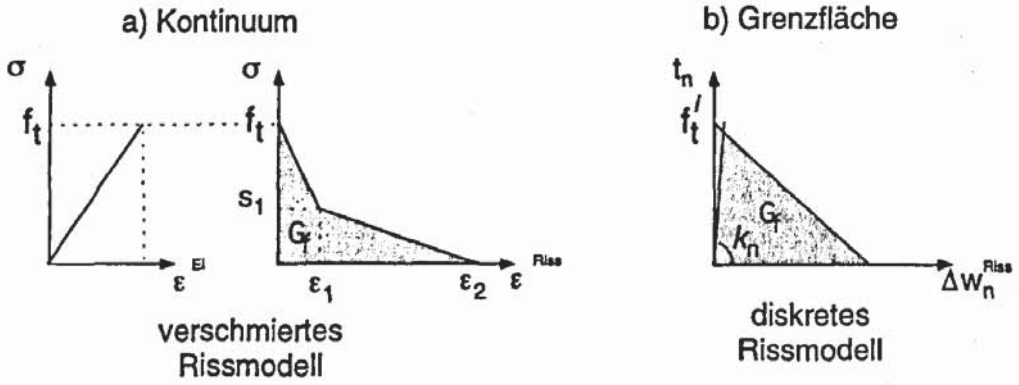

Abb. 1 : Mechanisches Verhalten eines „verschmierten" und eines diskreten Risses
Fig. 1 : Mechanical behaviour of a smeared and a discrete crack

Die Öffnung der Grenzfläche wird aktiviert, wenn f_t' erreicht wird. Nach der Rissöffnung wird das Entfestigungsverhalten als linear betrachtet (Abb. 1b).

Das Kriechverhalten von zementgebundenen Werkstoffen kann als viskoelastisch beschrieben werden. Für die Berechnung der Dehnung muss die Spannungsgeschichte berücksichtigt werden. Die folgende Integralgleichung beschreibt diesen Zusammenhang (Superpositionsprinzip) :

$$\varepsilon(\tau) = \int_{-\infty}^{t} J(t,\tau)\bar{C}\,\dot{\sigma}(\tau)d\tau \qquad (6)$$

wobei

t:	Zeit
τ:	Belastungsdauer
$J(t,\tau)$:	Kriechfunktion
$\bar{C}$:	Nachgiebigkeitsmatrix
$\dot{\sigma}(\tau)$:	globale Spannungsrate

In DIANA wird die Kriechfunktion durch eine Dirichlet - Reihe entwickelt:

$$J(t,\tau) = \sum_{\alpha=0}^{\infty} \frac{1}{E_\alpha}\left[1 - e^{-\frac{t-\tau}{\lambda_\alpha}}\right] \quad , \quad \text{mit } \lambda_\alpha = \frac{\eta_\alpha}{E_\alpha} \qquad (7)$$

wobei

E_α :	Steifigkeit des α-ten Kelvin Elements
λ_α:	Retardationszeit des α-ten Kelvin Elements
η_α:	Viskosität des α-ten Kelvin Elements

Diese Reihe kann physikalisch durch eine Serie von rheologischen Kelvin Elementen interpretiert werden. In Bild 2 ist eine Kelvinkette gezeigt.

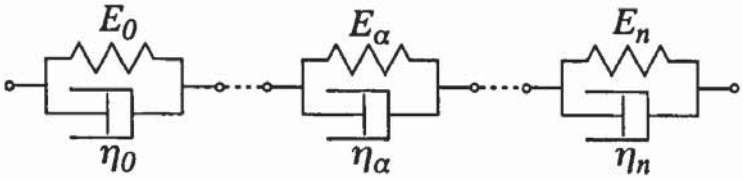

Abb. 2 : Ideale Kelvinkette
Fig. 2 : Ideal Kelvin chain

Die Parameter der Gleichung (7) werden aus den experimentellen Kriechkurven durch eine inverse Analyse automatisch in DIANA generiert. Auf diese Weise, können die Feuchtigkeitseinflüsse auf das viskoelastische Verhalten, wie zum Beispiel das Grund- und Austrocknungskriechen berücksichtigt werden.

2.2 Werkstoffeigenschaften für die numerische Analyse

2.2.1 Hygrische Eigenschaften

Es hat sich gezeigt, dass der feuchtigkeitsabhängige Diffusionskoeffizient durch eine inverse Analyse numerisch aus den Austrocknungsdaten bestimmt werden kann [9]. Es werden zur Beschreibung der Abhängigkeit des Diffusionskoeffizienten von der Feuchtigkeit unterschiedliche Funktionen verwendet. Nach unserer Erfahrung, hat sich die Exponentialfunktion für die Beschreibung der Abhängigkeit des Diffusionskoeffizienten bei mehreren porösen Werkstoffen (wie z.B. Beton oder Mörtel) als geeignet erwiesen:

$$D(h) = a \cdot \exp(b \cdot h) \tag{8}$$

hierin bedeuten

a, b : Parameter
h : Feuchtigkeitspotential

Die Diffusionskoeffizienten der Werkstoffe, die in den folgenden numerischen Simulationen untersucht werden, sind in Abbildung 3 wiedergeben.

Der Feuchtegehalt im jungen Mörtel wird durch die einsetzende Hydratation reduziert. Besonders bei tiefen w/z-Werten, führt dies zu einer deutlichen inneren Trocknung. Dies wurde mit Hilfe von kapazitiven Sonden an versiegelten Probekörper gemessen. Abbildung 4 zeigt die Ausgleichfeuchte im Mörtel als Funktion des Alters. Im betrachteten Mörtel reduzierte die endogene Trocknung die innere Feuchte auf 80%. In einer früheren Arbeit wurde das endogene Trocknen bereits auf solche Art berücksichtigt [10].

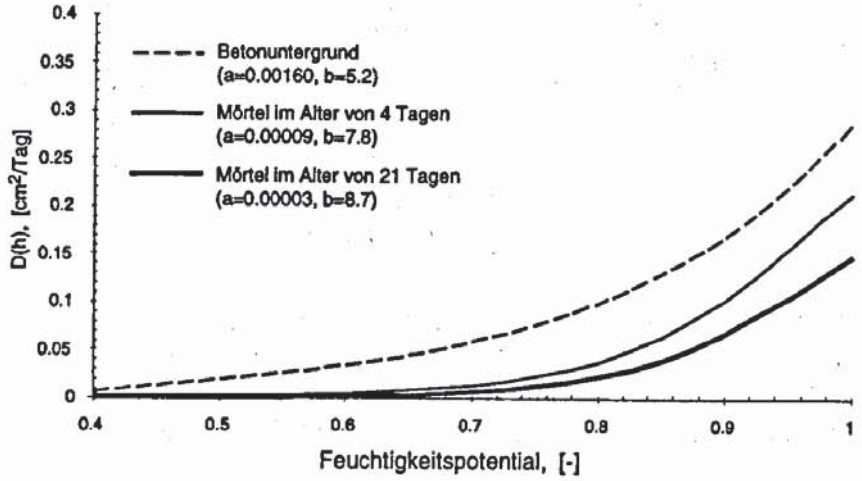

Abb. 3 : Diffusionskoeffizient für Beschichtung und Untergrundbeton
Fig. 3 : Moisture diffusion coefficients of the overlay and the substrate

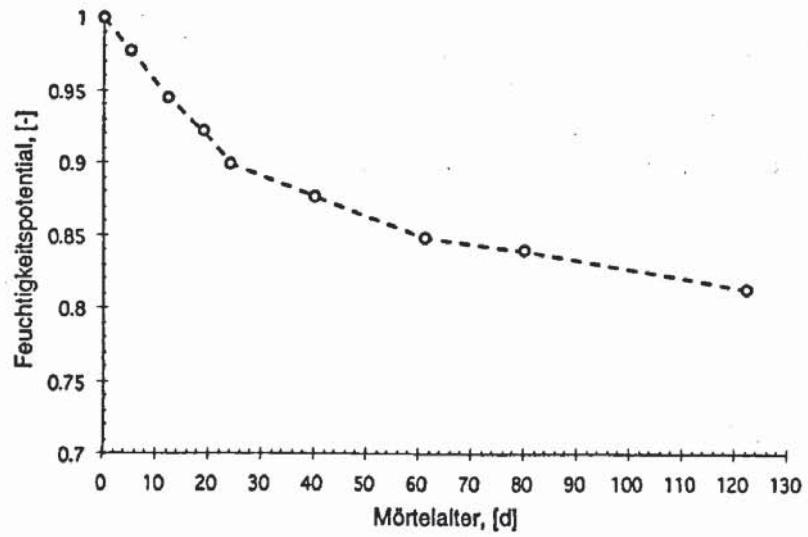

Abb. 4 : Feuchtigkeitsabnahme h_e durch endogene Trocknung
Fig. 4 : Decrease of humidity due to self dessication

Die daraus resultierende Feuchtigkeitssenke $q(t)$ der Gleichung (1) erhält man durch Ableiten der dargestellten Kurve :

$$q(t) = \frac{dh_e}{dt} = \frac{1.08}{(40+t)^2} \qquad (9)$$

Bei einem alten weitgehend hydratisierten zementgebundenen Werkstoff wird dieser Term $q(t)$ vernachlässigt.

Die gesamten Schwindverformung setzt sich aus dem externen Austrocknungsschwinden und dem endogenen Schwinden zusammen. Der Verlauf des Endschwindmasses ist in Abbildung 5a als Funktion des Feuchtigkeitspotentials gezeigt.

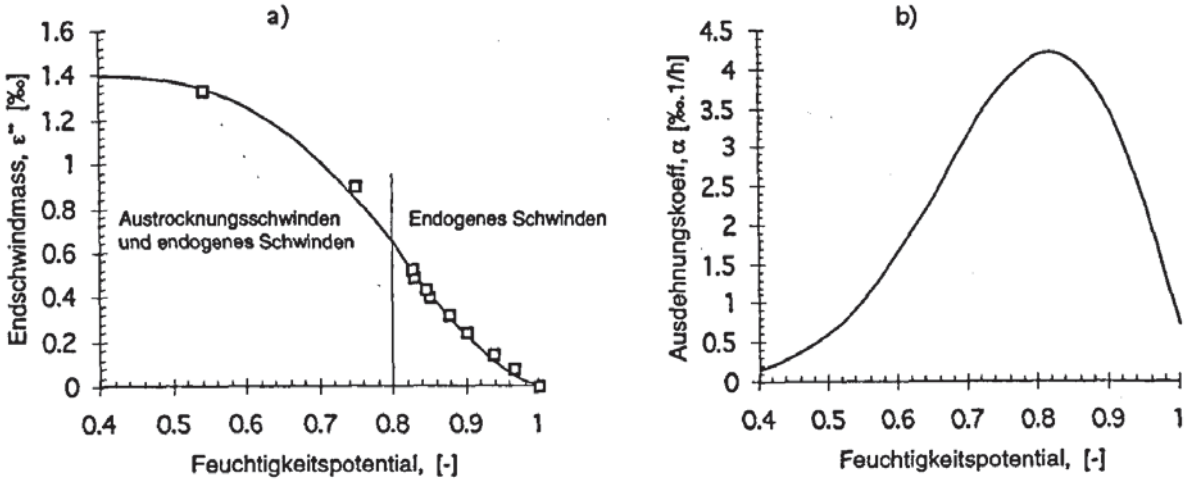

Abb. 5 : a) Endschwindmass und b) hygrischer Ausdehnungskoeffizient
Fig. 5 : a) Final shrinkage and b) hygral shrinkage coefficient

In diesem Fall konnte man die experimentellen Punkte mit einer Gaussfunktion fitten. Der hygrische Ausdehnungskoeffizient $\alpha_{Sch.}(h)$ (Abb. 5b) resultiert aus folgender Gleichung :

$$\alpha_{Sch.}(h) = \frac{d\varepsilon^{t\to\infty}(h)}{dh} \qquad (10)$$

2.2.2 Mechanische Eigenschaften

Die Bruchenergie und das Spannungsdehnungsdiagramm wurden mit dem Keilspaltversuch bestimmt [11,12].

Die Ergebnisse für einen herkömmlichen und einen kohlefaserverstärkten Mörtel und den Betonuntergrund sind der Tabelle 1 zu entnehmen.

Tabelle 1 : Mechanische Eigenschaften für die numerische Berechnung
Table 1 : Mechanical Properties for the numerical Analysis

	G_f [N/m]	E [GPa]	f_t [MPa]	s1 [MPa]	w1 [mm]	w2 [mm]
Mörtel A	55.	20.0	4.44	0.53	0.019	0.062
Mörtel B	288.	20.0	4.44	0.53	0.090	0.350
U.-Beton	95.	30.0	3.54	0.58	0.021	0.200

Um den Rissprozess zu aktivieren, wurde die Zugfestigkeit mit statistisch verteilten Werten eingeführt [13].

Die Adhesionfestigkeit und die Bruchenergie der Grenzfläche betragen 1.0 MPa beziehungsweise 25 N/m in Fall 1 und 3.0 MPa beziehungsweise 95 N/m in Fall 2.

Die gemessene Kriechfunktionen sind in der untenstehender Abbildung dargestellt.

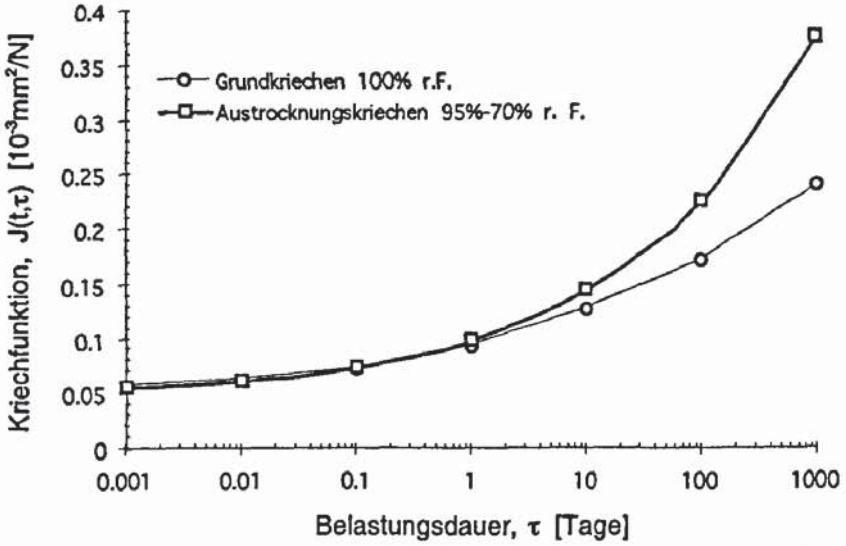

Abb. 6 : Verlauf des Grund- und Austrocknungskriechens
Fig. 6 : Basic and drying creep functions

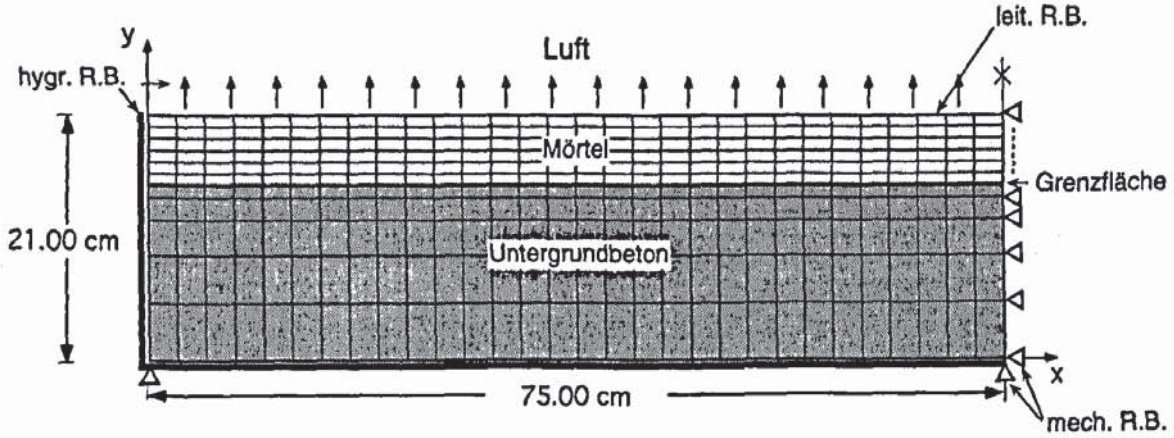

Abb. 7 : 2-dimensionales Netz für das betrachtete Bauteil
Fig. 7 : 2D finite element mesh of the investigated composite system

3 Beispiel für die Verwendung der Werkstoffkenngrössen im numerischen Modell

3.1 Modell

Das implementierte 2-dimensionale Netz ist in Bild 7 dargestellt. Die Beschichtungsdicke beträgt 60 mm, der Untergrund ist 150 mm dick. Auf der rechten Seite hat man eine Symmetrieachse und somit ist die gesamte Bauteil 1.50 m.

3.2 Feuchtigkeitsverteilung

Für die Berechnung der Feuchtigkeitsverteilung wurden zwei Anfangsbedingungen gewählt. Im ersten Fall ist der Untergrundbeton im Gleichgewicht mit 70% relativer Feuchtigkeit. Während der Oberflächenvorbereitung wurde Wasser durch Kapillarität aufgesaugt. Die zeitabhängigen Feuchteprofile sind in Abbildung 8 dargestellt. Die relative Umgebungsfeuchte beträgt dabei 60% und der Feuchteübergangskoeffizient 0.5 mm/d.

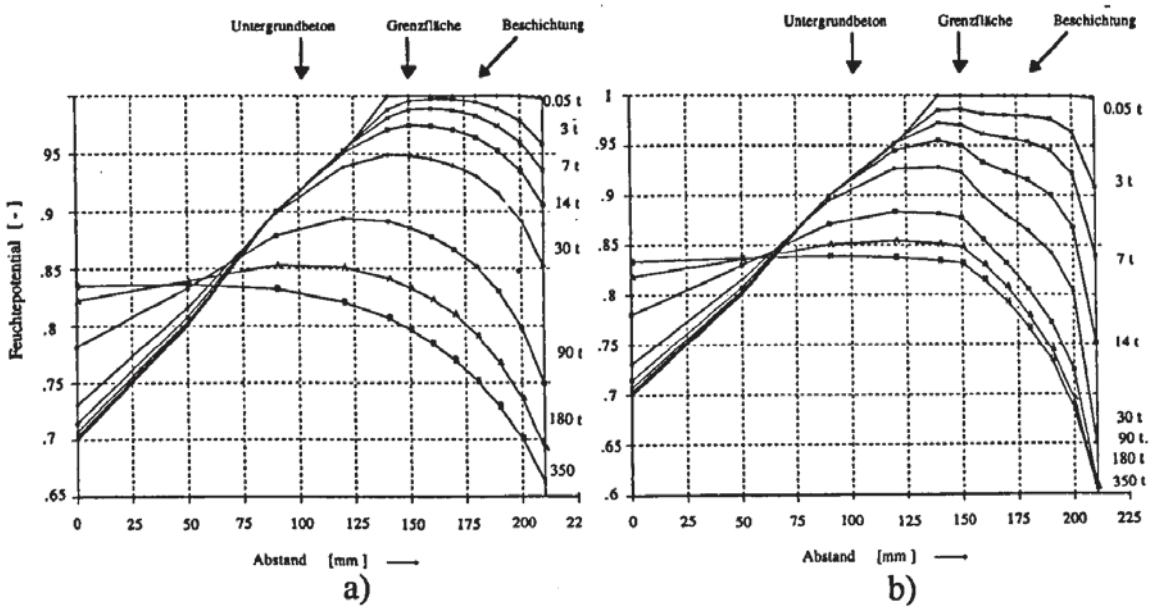

Abb. 8 : Feuchtigkeitsverteilung nach unterschiedlichen Trocknungszeiten a) ohne endogenes Trocknen b) mit endogenem Trocknen (Austrocknung nach rechts)

Fig. 8 : Moisture distribution at different drying times a) without endogeneous drying b) with endogeneous drying

In Abbildung 9 sind die Ergebnisse der Feuchteanalyse gezeigt wobei der Untergrundbeton als feucht gesättigt angenommen wurde.

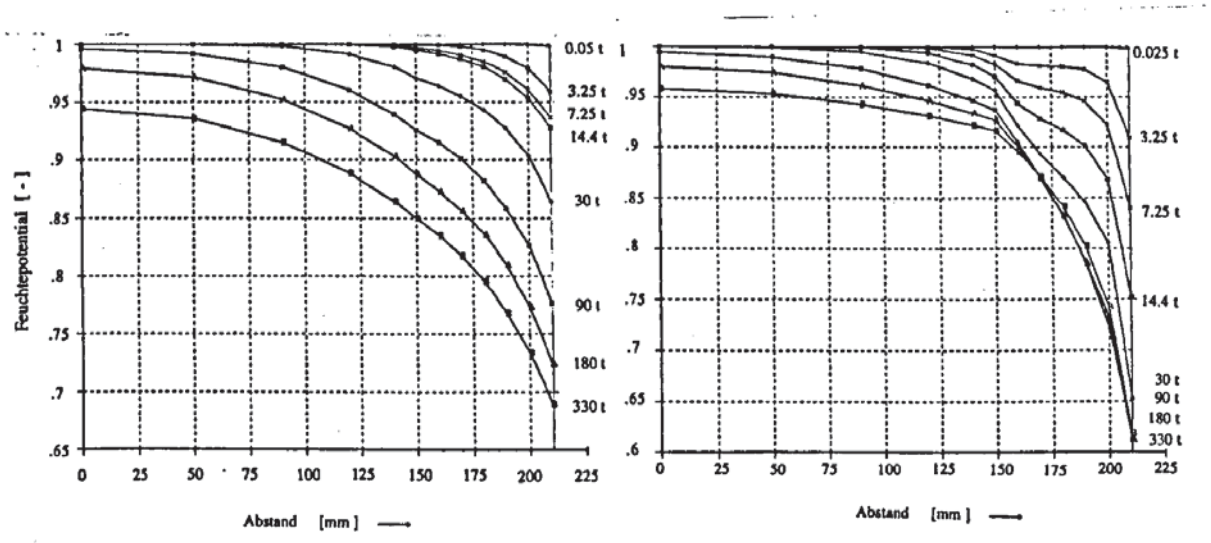

Abb. 9 : Feuchtigkeitsverteilung nach unterschiedlichen Trocknungszeiten, U.-Beton zu Beginn gesättigt a) ohne endogene Trocknung b) mit endogener Trocknung

Fig. 9 : Moisture distribution of a saturated drying system at different times a) without endogeneous drying b) with endogeneous drying

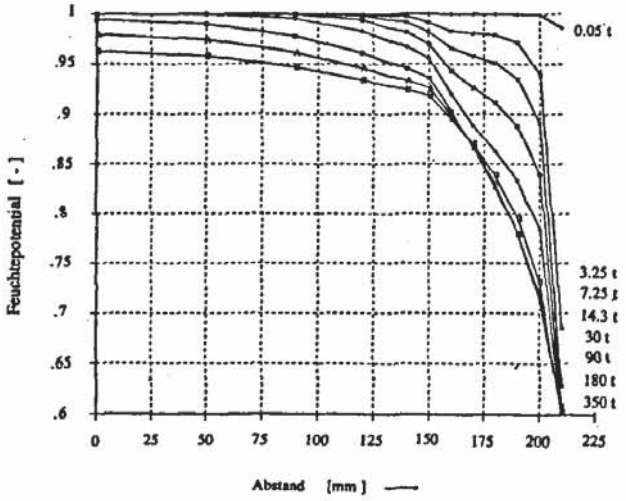

Abb. 10 : Feuchtigkeitsverteilung für die erste Anfangsbedingung nach unterschiedlichen Trocknungszeiten unter Berücksichtigung des Windeinflusses

Fig. 10. Hygral distribution for the first initial condition at different drying times subject to the action of wind

Im letzten Beispiel wurde der Einfluss vom Wind untersucht. Zu diesem Zweck wurde ein sehr grosser Feuchteübergangskoeffizient von 3.5 mm/d eingesetzt. Das Ergebnis ist in Abb. 10 dargestellt.

3.3 Verformungen und Rissbildung

3.3.1 Niedrige Haftzugfestigkeit

Im folgenden soll der Einfluß der wichtigsten Parameter anhand einer Parameterstudie untersucht werden. Die in Tabelle 1 charakterisierten Mörtel werden im Verbund mit den ebenfalls in Tabelle 1 charakterisiertem Beton untersucht. Für die folgende Berechnungen werden die hygrischen Bedingungen der Abb. 8b zu Grunde gelegt. Zunächst wird angenommen, daß die Haftzugfestigkeit 1 MPa beträgt. Die Rißbildung bzw. die Delamination bis zu einer Trocknungsdauer von 150 Tagen sind in der Abb. 11 dargestellt. Zunächst entstehen nahe der Oberfläche viele kleine Risse. Nach 61 Tagen haben sich im Mörtel A zwei Risse entwickelt. Man sieht daher, daß an der Stelle der Risse die Beschichtung abgelöst wird. Ebenso ist am Rand des Elementes zu diesem Zeitpunkt bereits Ablösung festzustellen. Nach 150 Tagen Trocknungsdauer erreicht ein dritter Riß im Mörtel A den Altbeton. Das Ablösen ist bereits im Ansatz zu erkennen. Mörtel B hat im Vergleich zu Mörtel A eine deutlich höhere Bruchenergie (siehe Tab. 1). Dies verhindert bis zu einer Trocknungsdauer von etwa 60 Tagen das Ausbilden durchgehender Risse. Nach 150 Tagen hat sich jedoch die Beschichtung am Rand gelöst und schüsselt auf. Zu diesem Zeitpunkt ist auch ein durchgehender Riss zu beobachten.

Das Ablösen am Rand ist in Abb. 12 noch einmal detailierter und als Funktion der Trocknungsdauer aufgetragen. Im oberen Teil (Mörtel A) ist dargestellt wie sich ein fiktiver Riss bildet, d.h. die Grenzfläche ist in diesem Fall noch in der Lage Kraft zu übertragen. Im unteren Teil dagegen ist gezeigt, daß sich beim Mörtel B nach etwa 110 Tagen ein realer Riss ausbildet. Danach schüsselt die Beschichtung rasch auf.

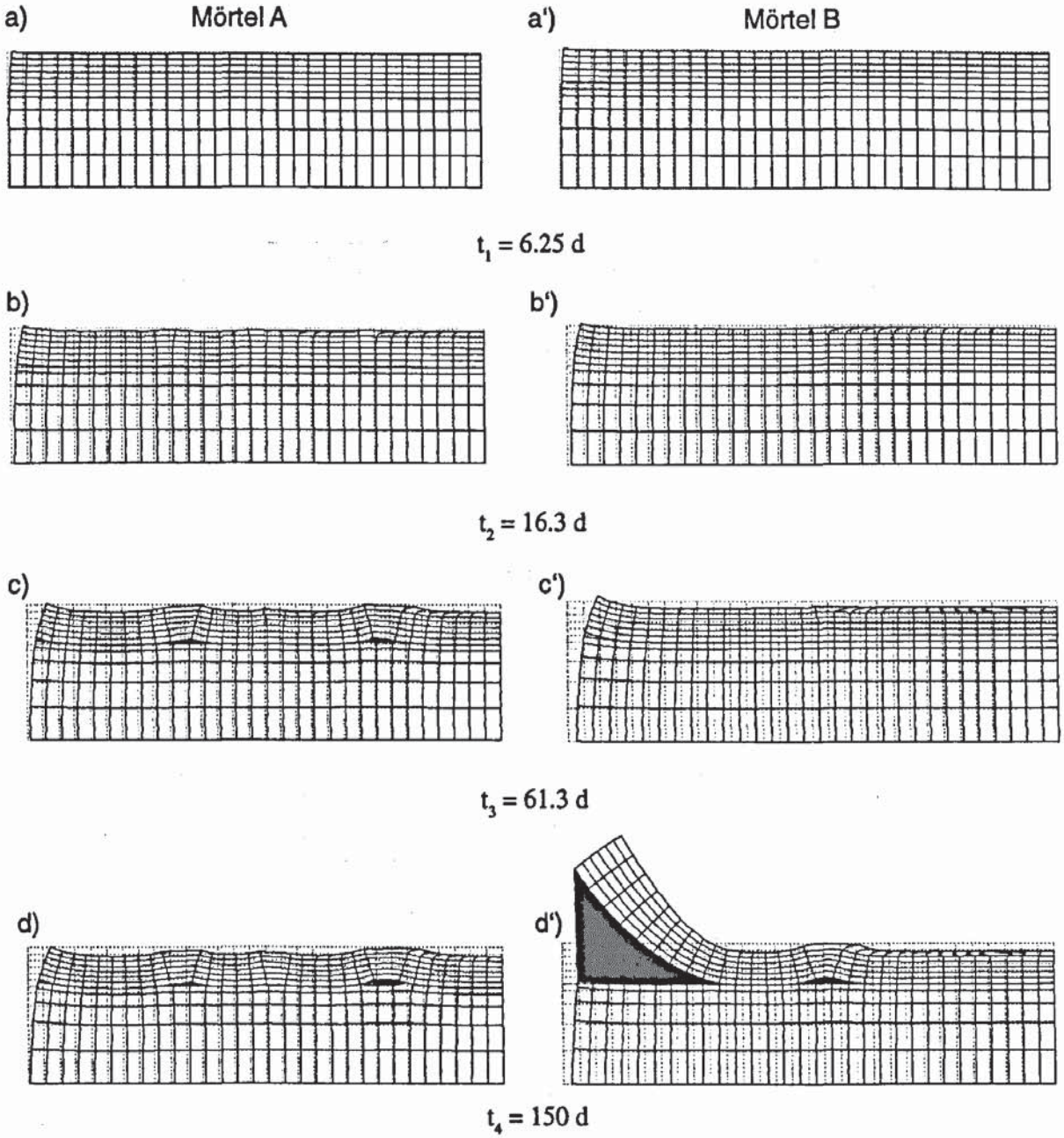

Abb. 11 : Zeitlicher Verlauf der Verformungen in x- und y- Richtung für Mörtel A und B

Fig. 11 : Evolution of the total deformation in x and y direction of mortar A and B

a)

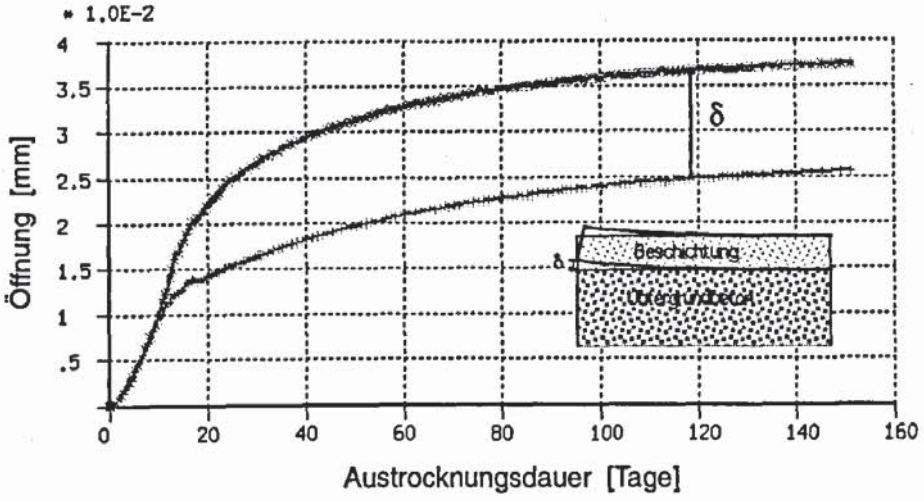

b)

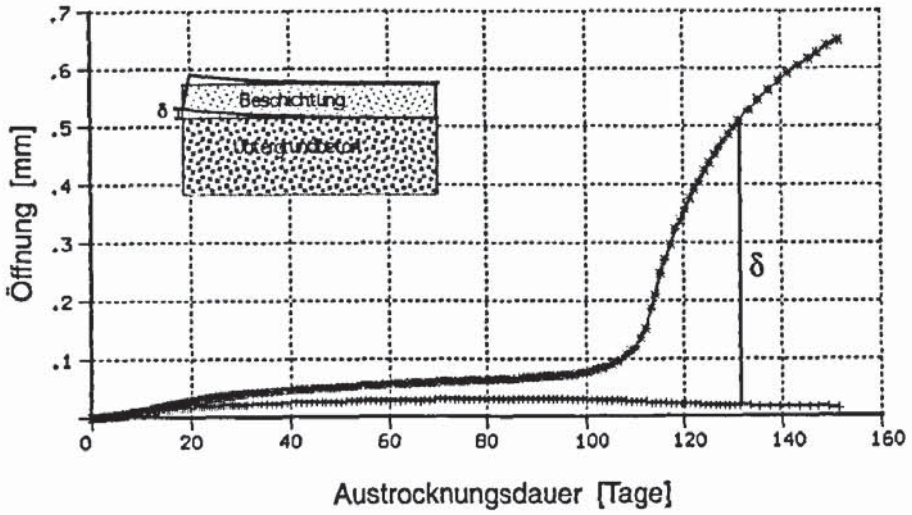

Abb. 12 : Zeitabhängige Öffnung der Grenfläche a) bei Verwendung von Mörtel A und b) bei Verwendung von Mörtel B

Fig. 12 : Evolution of the delamination at the interface of a) mortar A and b) mortar B

3.3.2 Hohe Haftzugfestigkeit

Im nächsten Beispiel wird angenommen, daß die Grenzfläche eine Haftzugfestigkeit von 3MPa aufweist. Zunächst bilden sich nahe der Oberfläche wieder viele kleine fiktive Risse. Nach etwa 60 Tagen Trocknungsdauer laufen drei Risse bis zum Beton durch den Mörtel A. Auch nach 150 Tagen löst sich die Beschichtung weder im Bereich der durchgehenden Risse noch am Rand vom Beton ab. In der Beschichtung B tritt erst viel später ein durchgehender Riß auf. Auch in diesem Fall kommt es nicht zur Ablösung.

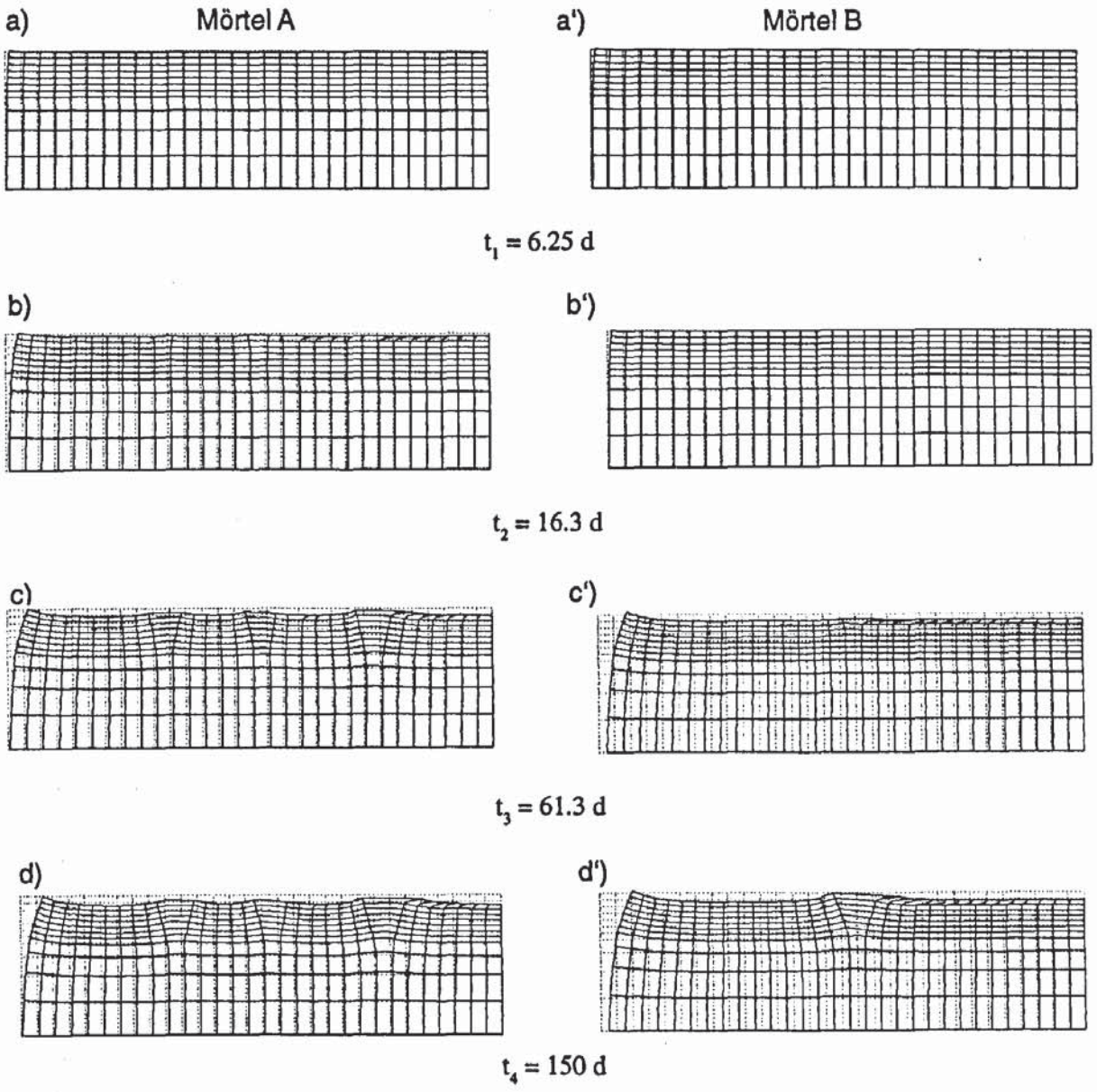

Abb. 13 : Zeitlicher Verlauf der Verformungen in x- und y- Richtung für Mörtel A und B mit einer Haftzugfestigkeit von 3 N/mm²

Fig. 13 : Evolution of the total deformation in x and y direction of mortar A and B with an adhesive strength of 3 N/mm²

3.3.3 Niedriger hygrischer Ausdehnungskoeffizient

Im dritten Beispiel wurde wieder angenommen, daß die Haftzugfestigkeit bei 3 MPa liegt. Bei den beiden vorgenannten Beispiel wurde der experimentell bestimmte Verlauf des hygrischen Ausdehnungskoeffizienten als Funktion des Feuchtigkeitspotentials eingesetzt (siehe Abb. 5). Jetzt wird angenommen, daß ein konstanter hygrischer Ausdehnungskoeffizient von $0.001h^{-1}$ nachgewiesen wurde. Unter diesen Voraussetzungen verformt sich das zusammengesetzte Bauteil nach 150 Tagen Trocknungsdauer wie in Abb. 14 dargestellt. An keiner Stelle wird die Zugfestigkeit der Werkstoffe erreicht. Es kommt auch nicht zur Ablösung.

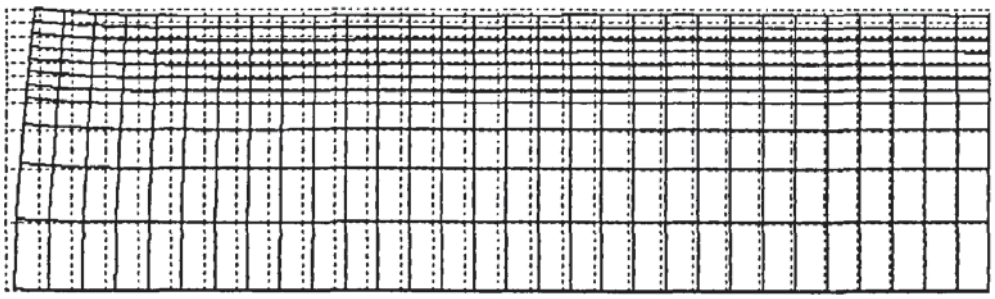

t = 150 d

Abb. 14 : Totale Verformungen für den Mörtel B mit einem konstanten hygrischen Ausdehnungskoeff. von 1.0 ‰1/h

Fig. 14 : Total deformation of a mortar with a constant hygral shrinkage coefficient of 1.0 ‰1/h

4. Folgerungen

Mit Hilfe eines numerischen Modells kann die Rißbildung an einer trocknenden zementgebundenen Beschichtung und die Ablösung berechnet werden. Der Einfluß unterschiedlicher Werkstoffparameter oder Randbedingungen kann wirklichkeitsnah berücksichtigt werden. Mit diesem Ansatz können Beschichtungen für gegebene Anwendungsfälle optimiert werden.

5 Danksagung

Die Autoren bedanken sich bei Herrn Dr. M. Oppliger und Herrn Dr. Q. Yang von der F+E-Abteilung der MBT Schweiz für die konstruktive Zusammenarbeit. Der Erstautor bedankt sich darüber hinaus bei der KTI, Schweiz; für die finanzielle Förderung des Projektes. Die Arbeiten wurden durch eine enge Zusammenarbeit mit dem Istituto Cantonale Tecnico Sperimentale wesentlich gefördert. Dem Leiter des Instituts danken wir dafür.

6 Literatur

1. G. Martinola, F. H. Wittmann, *Application of fracture mechanics to optimize repair mortar systems*, Proceedings FraMCoS-2, F.H. Wittmann, editor, AEDIFICATIO Verlag, 1481, Freiburg (1995)
2. DIANA, *Users Manual - Release 6.1*, Diana Analysis BV, Delft, Niederlanden (1996)
3. H. Sadouki, J.G.M. van Mier, *Simulation of Hygral Crack Growth in Concrete Repair Systems*, will be published in Mat. & Struct.
4. H. Sadouki, *Numerical Simulation of the hygromechanical behaviour of composite materials: Continuum and Lattice Approaches,* Research Report, Technical University of Delft, Delft, Niederlanden (1996)
5. J.G. Rots, *Computational modelling of concrete fracture*, Ph.D. thesis, Delft University of Technology, Niederlanden (1988)
6. Z.P. Bazant, B.H. Oh, *Crack band theory for fracture of concrete*, Mater. Struct. (RILEM), **16**, 155 (1983)
7. Z.P. Bazant, L.J. Najjar, *Drying of concrete as a nonlinear diffusion problem.* Cem. and Concr. Res., **1** , 461-473 (1971)
8. A. Hillerborg, M.Modéer, P.-E.Petersson, *Analysis of crack formation and crack growth in concrete by means of fracture mechanics and finite elements,* Cem. & Concrete Res., **6** , 773 (1976)
9. X. Wittmann, H. Sadouki, F.H. Wittmann, *Numerical evaluation of drying test data*, Trans. 10th Intern. Conf. on Strucutural Mechanics in Reactor Technology, **Q**, 71-79 (1989)
10. A.M. Alvaredo, F.H.Wittmann, *Shrinkage and cracking of normal and high performance concrete,* High Performance Concrete : Material Properties and Design, F.H. Wittmann and P.Schwesinger , editor, AEDIFICATIO Verlag, 91 Freiburg (1995)
11. E. Brühwiler, *Bruchmechanick von Staumauerbeton unter quasi-statischer und Erdbebendynamischer Belastung,* Dissertation no 739 École Polytechnique Féderal de Lausanne, 1988.
12. P.E. Roelfstra, F.H. Wittmann, *Numerical Method to link strain softening with failure of concrete*, Fracture toughness and fracture energy of concrete, F.H. Wittmann, editor, Elsevier, Amsterdam. (1986)
13. H. Sadouki, F.H. Wittmann, *Numerical concrete model applied to investigate size effect and stability of crack propagation*, Proceedings FraMCoS-2, F.H. Wittmann, editor, AEDIFICATIO Verlag, 619, Freiburg (1995)

Article n°4

Materials and Structures/Matériaux et Constructions, Vol. **30**, November 1997, pp 518-526

SCIENTIFIC REPORTS

Simulation of hygral crack growth in concrete repair systems

H. Sadouki and J.G.M. van Mier*

Delft University of Technology, Faculty of Civil Engineering, Stevin Laboratory, P.O. Box 5048, 2600 GA Delft, The Netherlands

**) On leave from ETH-Hönggerberg, CH-8093 Zürich, Switzerland*

Paper received: July 8, 1996; Paper accepted: September 17, 1996

ABSTRACT

In this paper, results of numerical simulations of a repaired concrete structure are presented. A repair layer of mortar was cast on top of a substrate of old concrete. The repair mortar was saturated with water, and allowed to dry at the top surface. The moisture distribution was determined using the finite element code DIANA. The moisture gradients lead to shrinkage cracking. Using the smeared crack model available in DIANA, and from the effect of decreasing the thickness of the overlay of repair mortar (from 60 to 15 mm), and by decreasing the bond strength between repair mortar and substrate from 3 to 1 MPa, it is shown that the number of hygral shrinkage cracks depends largely on the thickness of the repair layer. Moreover, in analyses with high interfacial strength, the cracks were found to propagate into the substrate. However, at lower bond strength, debonding was observed. The analyses show that hygral strains may cause severe damage in a repaired concrete system. Problems may decrease when the overlay thickness increases or when the bond between substrate and overlay is improved. In addition, applying reinforcement in the repair layer, either as discrete bars or as distributed fibres, may decrease the spacing and width of the shrinkage cracks, thereby reducing the probability of delamination. The numerical programme is shown to be a viable tool for damage analyses not only under mechanical load, but also under hygral gradients (and thermal gradients).

RÉSUMÉ

Dans cette contribution on présente les résultats de simulations numériques pour une structure en béton formée d'un vieux béton et d'une couche de mortier de réparation. Le mortier de réparation a été saturé d'eau ; on en a laissé sécher la surface supérieure. La distribution hydrique a été déterminée au moyen du code DIANA à éléments finis. Les gradients hydriques résultent en une fissuration de retrait. Au moyen du modèle de la bande microfissurée de DIANA pour étudier les effets d'une diminution de l'épaisseur de la couche de mortier de réparation (de 60 à 15 mm), et d'une diminution de l'adhérence entre le mortier de réparation et le substrat de 3 à 1 MPa, il a été montré que le nombre de fissurations induites par le retrait de séchage dépend largement de l'épaisseur de la couche de matériaux de réparation. De plus, lors des analyses où il existait une forte résistance interfaciale, on a trouvé que les fissurations se propageaient dans le substrat. À de plus faibles adhérences, une décohésion a été observée. Les analyses montrent que les contraintes hydriques peuvent entraîner de graves endommagements dans un système en béton réparé. On peut les diminuer en augmentant l'épaisseur de la couche de réparation ou en améliorant l'adhérence entre le substrat et le matériau de réparation. L'application de renforcement dans la couche de réparation, soit par des treillis d'armatures soit par des fibres, peut diminuer l'espacement et la largeur des fissurations de retrait, réduisant ainsi la probabilité de décohésion. On a montré que le programme numérique est un outil viable pour l'analyse des endommagements non seulement sous charge mécanique, mais également sous gradients hydriques et thermiques.

1. INTRODUCTION

The repair of concrete structures has become increasingly more important over the past few years. Durability problems, for example due to ingress of moisture and chlorides, or carbonation may lead to corrosion and subsequently damage the outer parts of the concrete structure. Much research is carried out to find repair methods that are capable of improving, or at least restoring, the earlier situation. One of the methods is to make an overlay of new concrete on top of the old concrete. The durability of such systems is then studied in long-term exposure tests. The

Editorial note:
Dr. Jan G. M. van Mier is a RILEM Senior Member. He is Secretary of TC 148-SSC on Test methods for the Strain Softening responses of Concrete and a member of TC 159-ETC on Engineering of the interfacial Transtion zone in Cementitious composites. In 1987, Dr. van Mier was awarded the Robert L'Hermite Medal for outstanding research work. Dr. van Mier is also a member of the RILEM Management Advisory Committee.

repair layer may fracture under any mechanical, physical or chemical loading. Physical loadings include hygral and thermal effects, for example caused by drying-out of the concrete or by exposure to sunlight, respectively. Hygral and thermal gradients that develop in the structure may eventually lead to crack growth and delamination. Tools for modelling the behaviour of repair overlays have gradually become available in numerical codes. In this paper, the DIANA finite element code [1] was used to simulate moisture transport and the effect on crack growth in a simple binary system composed of two different porous materials as shown in Fig. 1. The top layer is assumed to be cast on top of the older substrate. Only the top surface is exposed to a dry atmosphere, therefore leading to unidirectional moisture flow from the concrete to the atmosphere. After the analysis of the moisture flow in the substrate and overlay, a stress-analysis is carried out using the smeared crack model [2] in DIANA, which is based on the Bažant and Oh crack band model [3]. In this paper, first the theoretical background of moisture flow in porous media is treated, including a description of the numerical aspects and the material parameters needed. Subsequently, the smeared crack model is outlined, again elucidating the numerical implementation and the parameters needed in the model. Both moisture flow and stress analysis are considered un-coupled, which is a simplification from the real behaviour. Nevertheless, the results described in Section 4 are quite realistic. The sensitivity of the macroscopic analyses to a number of model parameters, such as the thickness of the new concrete overlay and the bond strength of the new to old concrete is discussed as well.

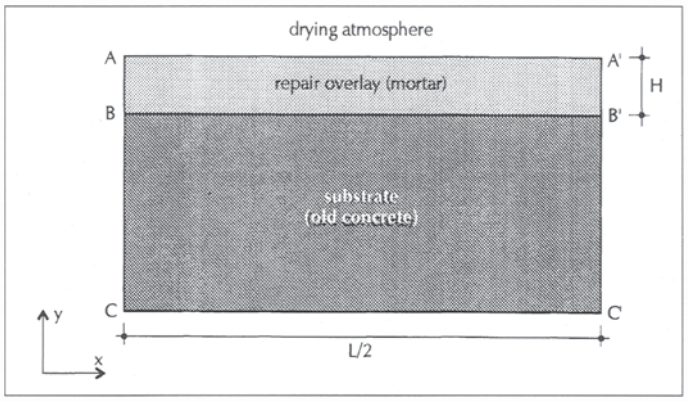

Fig. 1 – Schematic representation of the concrete repair system being considered.

At present, this work is being continued and moisture flow and fracture are being analyzed using a meso-level numerical lattice model [4]. The lattice model has proven to give realistic simulations of crack patterns in concrete and other brittle disordered materials. The extension to allow for moisture flow, and the incorporation of eigen-stresses caused by hygral gradients, is considered important to come to a better understanding of fracture of cement-based composites. A comparison between the macro- and mesoscopic simulations will be the topic of a future publication.

2. MOISTURE FLOW IN POROUS MEDIA

2.1 Background

Moisture variations in a cement-based composite may result from internal drying induced by the hydration reaction of cement and water at an early age (self-desiccation), or from climatological conditions during the life-span of the structure. Alternating wet and dry periods may lead to hygral gradients in the structure. Understanding the time-dependent development of hygral gradients is of utmost importance for analyzing crack growth. In the present paper, as mentioned, the analyses are limited to the macro-level. Moreover, only moisture changes induced by the interaction between the porous system and its surrounding atmosphere are considered.

At the macroscopic level, the moisture flow in a porous material (such as a cement-based composite) can be described phenomenologically by a diffusion equation [5, 6]. It has been recognized that the moisture transport coefficient (moisture diffusivity) of the above-mentioned materials is strongly dependent on the actual potential (*i.e.* the humidity or moisture concentration). The moisture diffusivity increases strongly as the moisture content increases. Different mathematical formulations describing the dependence of the diffusion coefficient upon the moisture potential can be found in the literature, *e.g.* [5-9]. An exponential diffusivity function will be assumed in this contribution [9]. If the pore humidity, rather than the moisture content concentration, is used as the potential, the transient moisture flow problem can be described by the following non-linear partial differential equation:

$$\partial h/\partial t = div\,(D(h)\,\nabla h) \text{ in vol } \Omega \qquad (1)$$

where h is the pore humidity ($0 < h < 1$), $D(h)$ the moisture-dependent diffusivity and t the time. In addition, the solution to equation (1) has to satisfy the boundary conditions of the problem (see Fig. 1). It has been assumed that the exchange of humidity between the exposed surfaces and the surrounding atmosphere is dependent on convection. The convective boundary conditions (free surface Γ in contact with the atmosphere) can be expressed as:

$$q_n = \beta\,(h_\Gamma - h_0) \text{ on } \Gamma \qquad (2)$$

where q_n is the moisture flux normal to the exposed surface Γ, β is the hygral convection coefficient, h_Γ is the humidity on the surface Γ and h_0 is the humidity of the atmosphere. In general, the coefficient β depends on many factors, such as the actual humidity, the temperature and the speed of the wind at the convective surface. In the present analyses, a constant mean value of β will be used. When symmetry is assumed, or when the surfaces are completely sealed, the corresponding fluxes (equation (2)) are zero.

To solve the diffusion equation (1), the initial conditions describing the spatial potential field in the system at the start of the flow process are required. This can be described by means of the following set of equations:

$$h(P_i, t = 0) = h_i \qquad (3)$$

in which P_i is localisation of a point in the volume and h_i is its potential value at the start of the analysis.

2.2 Numerical modelling

The advanced non-linear finite element programme DIANA [1] has been used to simulate the moisture flow in the drying porous system of Fig. 1. In DIANA, a special module is available for solving equation (1). The finite element discretization of the bi-material system is shown in Fig. 2. Four-noded flow elements are used to calculate the moisture distribution in the porous system. The top surface (A-A' in Fig. 1) is the convective surface. All other surfaces (*i.e.* CC', AC and A'C' in Fig. 1) are assumed to be sealed. Special two-noded convective finite elements have been used to simulate the humidity exchange between the porous system and the surrounding atmosphere. Symmetry has been assumed along line AC, and the half-length of the system is $L/2$ = 500 mm. The height of the substrate is 200 mm (distance BC in Fig. 1), whereas the thickness H of the repair layer varies from 15 to 60 mm.

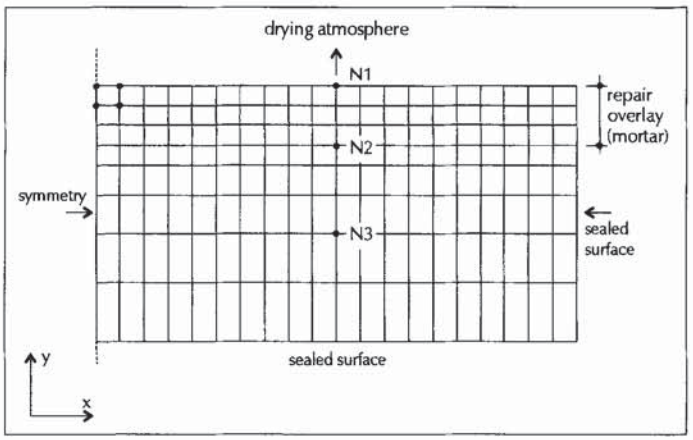

Fig. 2 – Finite element discretisation of the bi-material system of Fig. 1.

2.3 Material parameters

Besides the dependence on the moisture potential, the moisture diffusion coefficient $D(h)$ is strongly dependent on the composition of the porous material. In the present study, the substrate is assumed to be an old concrete with a w/c ratio of 0.5. In order to obtain the moisture diffusivity, saturated concrete specimens were exposed to different environments. During the drying tests, the moisture losses (weight) were measured as a function of time. An inverse numerical technique, combining the moisture diffusion equation (1) with the theory of the least-squares method, was developed to determine the moisture diffusivity of the material from the experimental data [9]. For the aforementioned concrete for the substrate, the following moisture diffusivity was found:

$$D_c(h) \simeq 0.22\, e^{5.4\,h} \tag{4}$$

where the subscript c stands for concrete and the dimension of D_c is [mm^2/day]. For the repair mortar, the following was assumed:

$$D_m(h) \simeq 5D_c(h) \tag{5}$$

For the convection coefficient of the exposed surface, β = 0.3 mm/day was assumed.

3. FRACTURE UNDER HYGRAL GRADIENTS

3.1 General remarks

In the present paper, hygral gradients were considered as the only driving force behind crack growth. Any other loading, such as mechanical stresses or thermally-induced strains, were excluded. During the drying of the porous system, hygral gradients develop over the height of the (repaired) structure, thus causing differential deformations. If a hypothetical fibre of any cross-section of the material is free to shrink under an infinitesimal drop Δh in humidity, the resulting unrestrained shrinkage strain can be computed as follows:

$$\Delta\varepsilon_{sh} = \alpha_{sh}\,\Delta h \tag{6}$$

where $\Delta\varepsilon_{sh}$ is the unrestrained hygral shrinkage and α is the so-called shrinkage coefficient. α depends on the composition of the material and on the humidity. In the range of humidities from 0.6 - 1.0, α can be roughly considered to be constant [10].

The internal restraint-to-volume changes across a section will generate eigen-stresses. In order to emphasize the importance of these induced eigen-stresses, a fibre of material subjected to a moisture variation Δh is considered. If the fibre is restrained to shrink, the resulting tensile stress σ can be calculated using,

$$\sigma = E\alpha_{sh}\,\Delta h \tag{7}$$

where E is the Young's modulus of the material. For mortar with E = 25 GPa, α_{sh} = 0.003 mm/mm.h, it follows that σ = 7.5 MPa when Δh = 0.1. Thus, the stress largely exceeds the tensile strength of the material. In cementitious materials subjected to drying, the tensile strength f_t is generally exceeded. Shrinkage can be restrained due to contact with any other material, *e.g.* [11]. For instance, in a concrete repair system, the shrinkage of the newly poured mortar (or concrete) can be restrained by the old concrete on which it was cast. If the bond between the repair material and the substrate is not sufficient, and the hygral gradient is large enough, delamination or surface cracking may occur in the repair mortar. In general, the hygral gradients are large enough to cause cracking, and adequate fracture mechanics tools must then be applied. For a continuum-based analysis, the application of a macroscopic elastic-softening model seems adequate. For example, a specimen subjected to uniaxial tension does not fail suddenly when the tensile strength is reached, but rather a gradually decreasing stress is measured with increasing axial deformation. This so-called softening behaviour is caused by crack nucleation and growth processes at the meso-level, *e.g.*

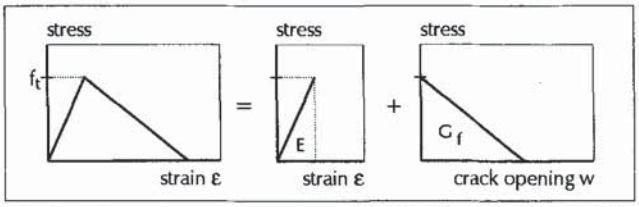

Fig. 3 – Schematic representation of the Fictitious Crack Model.

[12]. The gradually fracturing cross-section of the tensile specimen gradually loses its load-bearing capacity. Macroscopic models incorporating macroscopic softening are mostly based on the Fictitious Crack Model (FCM) developed by Hillerborg and co-workers [13, 14]. It is an appropriate macroscopic description of the fracture process. The stress-deformation diagram under tension is split into a pre-peak stress-strain diagram, which is characterised by the Young's modulus E of the material and the tensile strength f_t, and a post-peak stress-crack opening diagram (or softening diagram). The post-peak relation is fully characterised by the shape of the softening curve. The area under this curve is the fracture energy G_f [N/m]. The model is shown schematically in Fig. 3. The Crack Band Model developed by Bažant and Oh [3] is quite similar, except that it assumes that crack growth occurs in a band, rather than in a line. The Crack Band Model forms the basis for the smeared crack model in DIANA. There are still quite a few problems in defining and determining the parameters for the FCM, but as an approximation of crack growth phenomena at the macro-level it seems quite suitable.

3.2 Numerical tools

As mentioned before, the combined flow-stress analysis is performed with DIANA. The calculated time-dependent humidity distribution from the transient flow analysis (Section 2) is stored in a file for every time step Δt. For the stress and fracture analysis, the incremental hygral load Δh is converted to a strain field *via* the hygral shrinkage coefficient α_{sh}. The two analyses are uncoupled, *i.e.* it is assumed that the moisture diffusivity is not affected by crack growth. This hypothesis seems justified by recent experiments demonstrating that the rate of drying increases very slightly only when hygral cracks develop [15].

The multiple fixed smeared crack model developed by Rots [2] has been used to simulate crack growth in the repair layer and the substrate. As mentioned, the smeared crack model is a band model in the spirit of the Bažant and Oh model. The strain is decomposed into an elastic part and a crack strain. The crack strain is obtained by dividing the crack opening by the crack band width, which is generally the size of the finite element or of the distance between two Gauss points in a finite element. Crack initiation is governed by a (2D) tension cut-off criterion and a threshold angle between two consecutive cracks. A detailed description of the model can be found in [2].

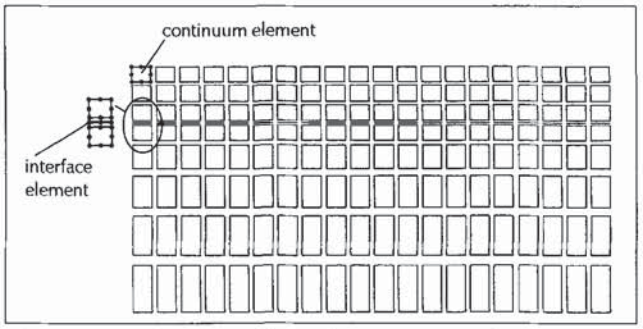

Fig. 4 – Finite element mesh for the repair system for the stress and fracture analysis.

The interface between the repair layer and the substrate is modelled using the interface elements available in DIANA. After the initiation of a (discrete) interface crack, again a softening relation is assumed between stress and crack opening. Under crack growth, the tangential stiffness is reduced by means of a shear retention factor [2]. The finite element mesh used for the stress and fracture analysis is shown in Fig. 4. The continuum elements are eight-noded isoparametric elements, and are fully compatible with the elements used in the transient flow analysis. The interface elements have six nodes.

A softening relation proposed by Reinhardt and Moelands (*i.e.* see [16]) was used for the fracture analyses and is given by:

$$\sigma_{nn}^{cr} = f_t \left[1 - \left(\frac{\varepsilon_{nn}^{cr}}{\varepsilon_{nn,ult}^{cr}} \right)^c \right] \tag{8}$$

where σ_{nn}^{cr} and ε_{nn}^{cr} are the stress and strain in the direction normal to the crack, and $\varepsilon_{nn,ult}^{cr}$ is the ultimate crack strain. c is a constant equal to 0.31. The ultimate crack strain is related to the size of the finite element l, as well as to the model parameters G_f and f_t according to:

$$\varepsilon_{nn,ult}^{cr} = 4.226 \frac{G_f}{l f_t} \tag{9}$$

3.3 Material parameters

As mentioned, the FCM requires the Young's modulus E, the tensile strength f_t and the fracture energy G_f as input parameters. Furthermore, for the shrinkage analysis, α_{sh} must be specified. All parameters must be given, both for the substrate and for repair layer materials. In Table 1 these values are summarized.

Two different values for the hygral shrinkage coefficient were considered, namely 2.25 and 1.25‰ mm/mm.h. In the overlay, statistically-distributed mechanical properties were introduced, otherwise the entire overlay would fracture instantaneous because the state of stress is rather homogeneous. The Young's modulus and the tensile strength were assumed to be randomly distributed over the columns of elements (this implies that all elements in each column get the same strength, but there are differences between columns). A scatter of 10% of the mean values of E and f_t was

Table 1 – Input parameters for the mechanical analysis			
	Substrate	Repair layer	Bond layer
Young's modulus E [GPa]	31	26	-*)
Tensile strength f_t [MPa]	5	4	1-3
Fracture energy G_f [N/m]	100	160	25

**) The bond layer elements are interface elements for which a spring stiffness must be specified. This is always a relatively high value,* i.e. *> 10^5 N/mm.*

assumed. The random variables E and f_t are adequately correlated by forcing them to follow the same statistical distribution. Introducing a statistical distribution is in good agreement with the heterogeneous nature of the concrete. The bond strength between substrate and repair layer was varied, as shown in Table 1. No statistical strength distribution was used for the bond strength. The fracture energy for the bond layer was similarly small.

Fig. 5 – Computed moisture distributions in the bi-material structure. The situations after 3 months (a), 6 months (b) and 1 year (c) are shown. The thickness of the repair layer is 60 mm.

4. NUMERICAL RESULTS

4.1 Moisture distribution in the bi-material system

At the start of the analysis, it is assumed that the overlay is fully water-saturated, *i.e.* $h = 1$. A gradual increasing initial humidity from the bottom to the interface between substrate and repair mortar is assumed; a higher humidity of $h = 0.95$ was given to the upper row of elements (*i.e.* closest to the interface), reflecting the moisture suction from the repair mortar when it is cast, and the possible humidification of the old concrete substrate before the repair mortar is applied. The lower parts of the substrate have the same humidity as assumed for the atmosphere, namely $h = 0.6$. The moisture distribution at $t = 0$ can be seen from Fig. 6. The top of the repair layer is exposed to the atmosphere with a constant humidity $h = 0.6$. In Fig. 5, the simulated hygral contours at three different drying times (3, 6 and 12 months) are plotted. The thickness of the repair mortar is in this case 60 mm. Fig. 6 shows the moisture profiles across a vertical section at different drying intervals. It can be seen that the initially moisture saturated repair layer gradually loses moisture from its exposed surface through convection. The moisture loss also occurs at deeper parts of the structure, as can be seen from these two figures. In particular, the last profile at 480 days in Fig. 6 shows that most of the moisture gradients have disappeared. This is even more pronounced when the moisture-histories of three nodes in the repair layer and the substrate are considered. The locations of the nodes N1-N3 are shown in Fig. 2. N1 and N2 are in the repair mortar and at the

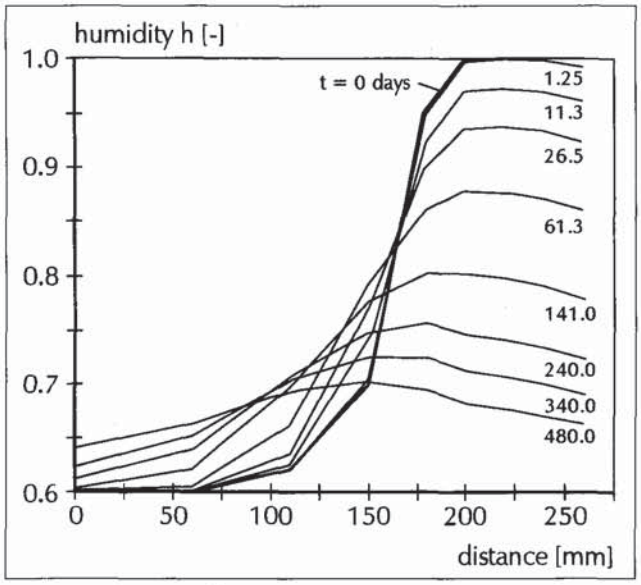

Fig. 6 – Moisture profiles in a cross-section of the repaired system at different drying times: $t = 0$ (initial state), 1.25, 11.3, 26.5, 61.25, 141, 240, 340 and 480 days. The thickness of the repair overlay is 60 mm.

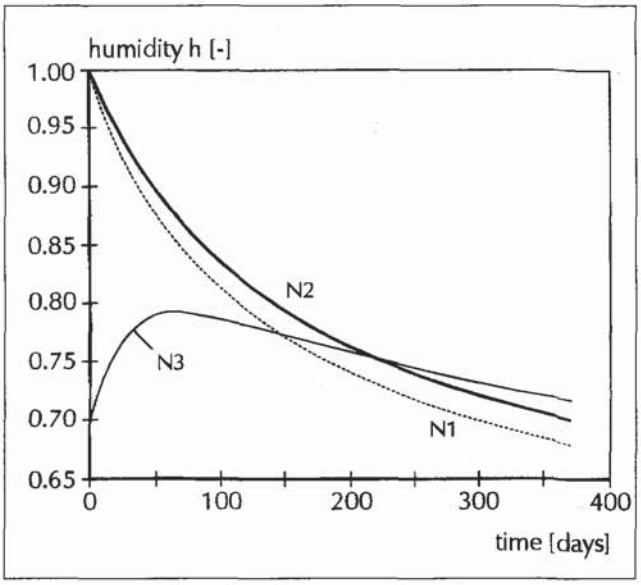

Fig. 7 – Computed moisture histories at the nodes N1, N2 and N3 (see Fig. 2 for the location of the nodes). The thickness of the repair overlay is 60 mm.

interface respectively, whereas N3 is in the substrate. In the beginning, largely varying humidities are found, whereas at the end of the simulation equilibrium is almost achieved.

For comparison, the simulated moisture histories at the nodes N1-N3 are shown in Fig. 8 for the case where the repair layer has a thickness of 30 mm only. In this case, because of the reduced thickness of the repair mortar, equilibrium is reached much faster. In the next section, it will be shown that the structure with a reduced overlay thickness is much more prone to cracking.

4.2 Crack formation and propagation

4.2.1 High-bond interface

In the case of a repaired structure with an overlay of 60 mm thickness, the first cracks appear at the top surface of the repair material at t = 14.3 days. Note that these cracks can still transfer load; they must be regarded as a fracture process zone where microcracking and crack face bridging occurs. During the next time steps, the process zone gradually increases in width, until a second zone develops at t = 27 days. As the drying process proceeds, cracking is governed by two phenomena, namely: (1) a number of distributed cracks will close, whereas other distributed cracks appear at certain integration points in the repair layer, and (2) simultaneously, the width of the two vertical cracks increases. In Fig. 9a the crack deformations are plotted at t = 273 days, clearly showing the two vertical cracks penetrating the substrate. No other "spectacular" events can occur after that due to the gradual drying of the structure. The system evolves to a state of hygral equilibrium. The final deformed state of the structure is shown in Fig. 9b (t = 273 days). It should be mentioned here that for a bond strength greater than 2 MPa, no delamination occurred. The substrate and the repair layer worked as a single concrete element. Note that no crack developed at the right side of the structure. This edge of the structure can deform freely.

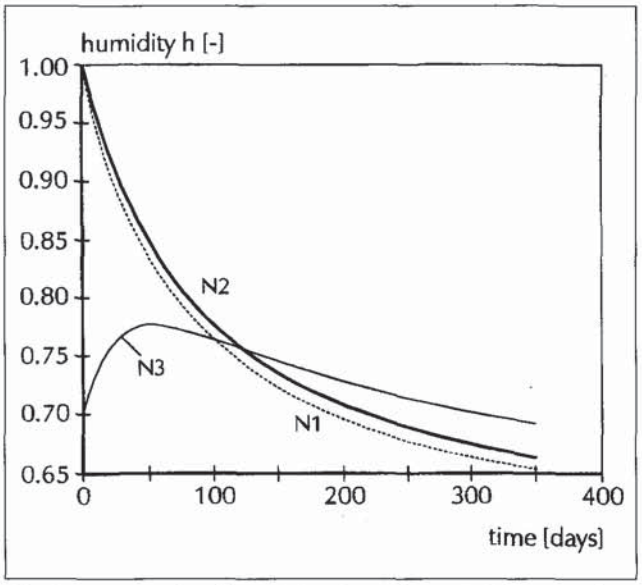

Fig. 8 – Computed moisture histories at the nodes N1, N2 and N3 (Fig. 2), when the repair layer thickness is 30 mm.

In the second analysis, the thickness of the repair layer was reduced to 30 mm. All the other parameters were kept the same. The crack process can now be summarized as follows. The occurrence of the first crack is similar to the first analysis with H = 60 mm. However, cracking occurs at an earlier stage (t = 8.75 days). The reason is that, because of its lower thickness, drying-out proceeds at a faster rate. This can be clearly observed from comparing Figs. 7 and 8 where the results of the flow analyses were summarized. In the case of the thin overlay, two process-zones develop next, at t = 11.3 and 13.8 days,

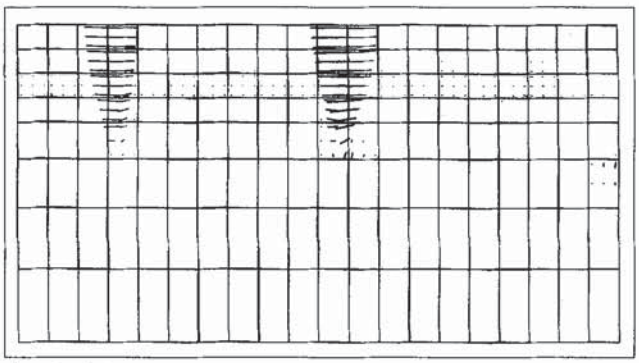

▲ Fig 9(a)

▼ Fig. 9 (b)

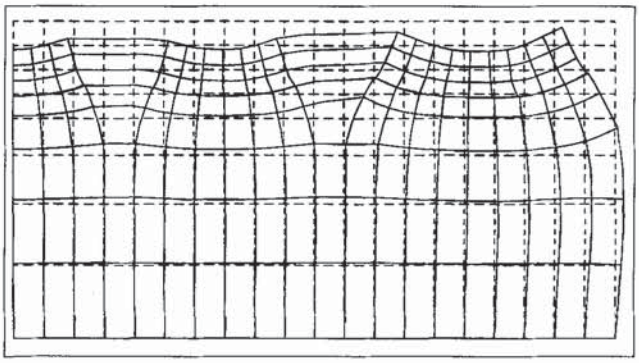

Fig. 9 – Crack deformation distribution at t = 273 days (a), and total deformed shape of the structure after 273 days of drying (b) for the repaired structure with H = 60 mm. The deformations in Fig. (b) have been exaggerated for better visualisation of the fracture process.

respectively. Again, during the analysis, a number of distributed microcracks close and others appear. However, the main fracture process is characterized by the widening of the three crack zones. Fig. 10 shows the state of cracking after a drying time of 200 days. In Fig. 10a, the deformed shape of the structure is shown, in Fig. 10b, the crack deformations ε_{nn}^{cr}.

Upon further decreasing the thickness of the overlay, *i.e.* to H = 15 mm, the first damage is observed after t = 4.75 days. In this case, the fracture process is becoming more complex. Between t = 4.75 days and 11.3 days, several crack bands develop, all of them, however, with a very small crack opening. Ultimately, only a small number of cracks survive and dominate the behaviour of the structure. At further drying, eventually only four open crack zones survive, while all the other cracks close (t = 291 days). Again, due to the relatively high bond strength for the interface between repair mortar and concrete substrate (*i.e.* 2 MPa), the cracks propagate into the substrate concrete. The number of macro-cracks is determined by the geometry of the structure and the boundary conditions. In the present analyses, the thickness of the repair mortar is the main controlling parameter. Similar crack growth histories are found in concrete slabs subjected to thermal gradients (*e.g.* [17]), but also in bond-slip tests between steel and concrete, where similar phenomena are observed (*e.g.* [18]). In the above analyses, debonding effects were insignificant because of the rather high bond strength of 2 MPa. Next, the effect of varying the bond strength is simulated.

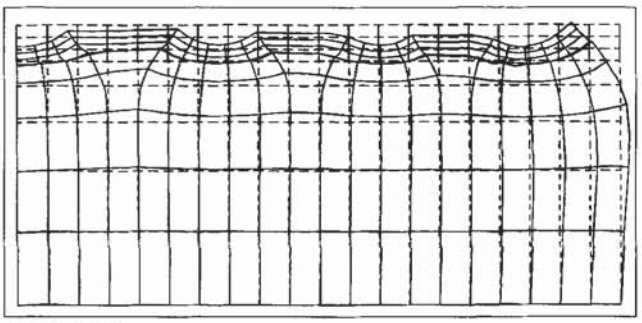

▲ Fig 10(a)

▼ Fig. 10 (b)

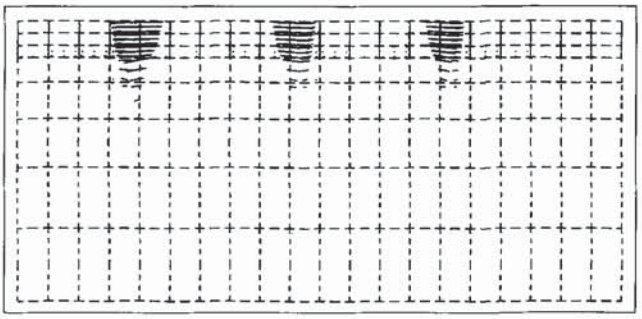

Fig. 10 – The state of damage in the structure with a 30 mm thick overlay at t = 200 days. The total deformed mesh is shown in Fig. (a), the crack deformations in Fig. (b). Note that the cracks also grow into the substrate concrete.

4.2.2 Low-bond interface

The analysis with H = 60 mm was repeated. The bond strength of the interface between substrate and repair mortar was reduced to 1 MPa, and a coefficient of hygral shrinkage α_{sh} = 1.25 ‰ mm/mm.h was assumed. All other parameters were kept the same. The initial distinct crack band developed at t = 11.25 days. Note that the crack appeared earlier as in the previous analysis (t = 14.3 days), which can be explained from the differences between the shrinkage coefficients. Debonding was initially observed at t = 15.25 days. A symmetric, horizontal crack grew along the interface starting from the location where the shrinkage crack hit the substrate (Fig. 11). A second shrinkage crack developed later, and here again delamination between the repair layer and the substrate was ultimately

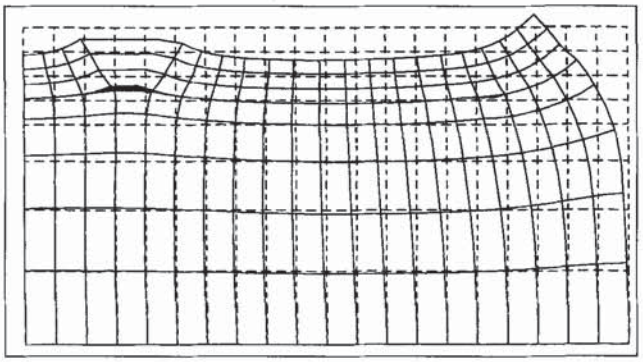

Fig. 11 – Deformed mesh of the structure with a repair mortar overlay of H = 60 mm, after the appearance of the first debonding crack at a drying time t = 15.25 days. The bond strength of the interface was reduced to 1 MPa.

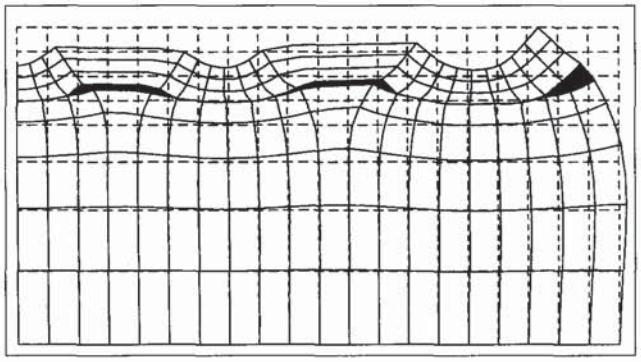

Fig. 12 – Deformed mesh for the structure with a low interfacial strength of 1 MPa, after t = 41 days. Delamination near the shrinkage cracks and at the far right end of the structure is clearly visible.

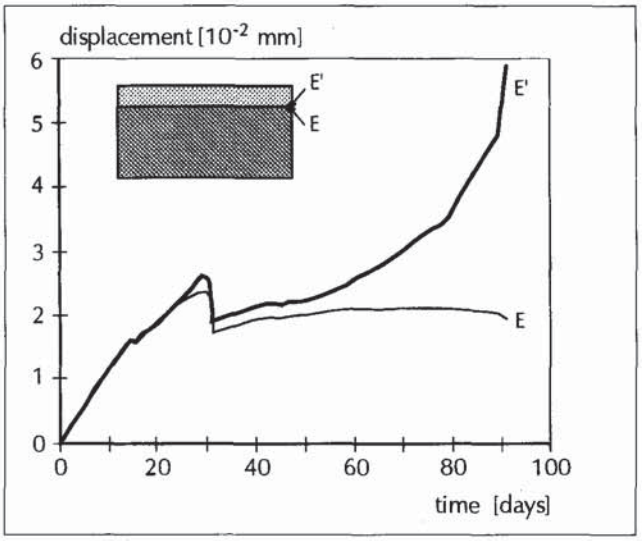

Fig. 13 – Vertical displacements of the two nodes of the interface element at the far right end of the structure (delamination crack) as a function of drying time.

observed. In Fig. 12, the deformed mesh is shown at t = 41 days. Note that delamination also occurred at the far right end of the structure. Upon further drying, the cracking remains limited to the two main shrinkage cracks, and the debonding between the substrate and repair mortar. Some numerical instabilities were observed during the analyses, in particular when the interface cracks developed. Moreover, stress-locking (as found earlier by Rots [2]) was found to occur in the smeared cracks. Such problems might be circumvented in lattice-type analyses, at the cost however of longer computational times.

Finally, Fig. 13 shows the displacement in the y-direction at the interface at the right-end side of the structure (*i.e.* the vertical displacements between nodes E and E′ of the last interface element). It can be seen that decohesion occurs after approximately 24 days of drying. The figure reveals a large drop in displacement at $t \approx 31$ hours, which corresponds to the development of the second shrinkage crack. At t = 90 days, the opening of the debonding crack EE′ was approximately 35 μm. It might be concluded that an interface strength of 1 MPa is still too high. For example, Zimbelmann [19] performed numerous bond tests in which a cement mortar was cast against different types of rock. In his tests, the bond strength was usually below 1 MPa. In this case, delamination would be expected at even earlier stages, thereby resulting in a more severe damage after extensive periods of drying out.

5. CONCLUSIONS

In this paper, simulations of damage induced by drying shrinkage in cementitious repair systems are presented. A repaired concrete structure consisting of a concrete substrate and a repair mortar overlay is considered. Based on the simulations, the following conclusions can be drawn:

(1) The flow module of the finite element code DIANA and the smeared crack model are viable tools for the analysis of coupled flow/strength problems in concrete structures at the macro-level.

(2) Due to drying of the bi-material structure, hygral strains develop which cause crack growth in the structure.

(3) Damage consists of a limited number of narrow crack bands perpendicular to the surface exposed to drying. The number of these shrinkage cracks is directly related to the geometry (thickness) of the mortar overlay.

(4) Shrinkage cracking is delayed when the thickness of the overlay increases.

(5) When the bond strength is sufficiently high, the damage is limited to the development of these vertical shrinkage cracks, which may also propagate into the substrate.

(6) When the bond strength decreases, delamination of the mortar overlay may occur. The delamination cracks initiate from the vertical shrinkage cracks.

(7) Using the numerical tools, the effect of different repair geometries can easily be simulated. An improved insight in the durability of repaired concrete structures can thus be obtained.

ACKNOWLEDGEMENT

The present work was made possible through a grant of the Netherlands School for Advanced Studies in Construction, the Ministry of Works and ETH Zürich. The authors are indebted to this support. Moreover the assistance of our colleagues of the Computational Mechanics Group at TNO Building Research is gratefully acknowledged.

REFERENCES

[1] DIANA, Users manual - Release 6.1, Diana Analysis BV, Delft, The Netherlands (1995).

[2] Rots, J.G., 'Computational modelling of concrete fracture', Ph.D. thesis, Delft University of Technology, The Netherlands (1988).

[3] Bažant, Z.P. and Oh, B.-H., 'Crack band theory for fracture of concrete', *Mater. Struct.* **16** (155) (1983).

[4] Schlangen, E. and Van Mier, J.G.M., 'Experimental and numerical analysis of micro-mechanisms of fracture of cement-based

composites', *Cem. & Conc. Composites* **14** (105) (1992).
[5] Pihalajavaara, S.E., 'On the main features and methods of investigation of drying and related phenomena in concrete', PhD thesis, University of Helsinki, Finland (1965).
[6] Bažant, Z.P. and Najjar, L.J., 'Drying of concrete as non-linear diffusion problem', *Cem. & Conc. Res.* **1** (461) (1971).
[7] Daian, J.F., 'Processus de condensation et de transfert d'eau dans un matériau méso et macroporeux. Étude expérimentale du mortier de ciment', Thèse de Doctorat Sciences Physiques, Université de Grenoble, France (1986).
[8] Sakata, K., 'A study on moisture diffusion in drying shrinkage of concrete', *Cem. & Conc. Res.* **13** (216) (1983).
[9] Wittmann, X., Sadouki, H. and Wittmann, F.H., 'Numerical evaluation of drying test data', Transaction 10th Int'l. Conf. on Struct. Mech. in Reactor Techn., Vol. Q (71) (1989).
[10] Martinola, G. and Wittmann, F.H., 'Application of fracture mechanics to optimize repair mortar systems', in 'Proceedings FraMCoS-2', Wittmann, F.H., Ed., (AEDIFICATIO Publishers, Freiburg, 1995) 1481.
[11] Alvaredo, A.M., 'Drying shrinkage and crack formation', PhD thesis, Institute of Building Materials, Swiss Federal Institute of Technology, Zürich, Switzerland (1994).
[12] Van Mier, J.G.M., 'Fracture Processes of Concrete - Assessment of Material Parameters for Fracture Models' (CRC Press, Boca Raton, 1997).
[13] Hillerborg, A., Modéer, M. and Petersson, P.-E., 'Analysis of crack formation and crack growth in concrete by means of fracture mechanics and finite elements', *Cem. & Conc. Res.* **6** (1996) 773.
[14] Petersson, P.-E., 'Crack growth and development of fracture zones in plain concrete and similar materials', Report TVBM-1006, Lund Institute of Technology, Sweden, 1981.
[15] Wittmann, F.H., 'Influence of drying induced damage on the hygral diffusion coefficient', in Proceedings FraMCoS-2, Wittmann, F.H., Ed. (AEDIFICATIO Publishers, Freiburg, (1995) 1481.
[16] Reinhardt, H.W., 'Fracture mechanics of an elastic softening material like concrete', *HERON* **29** (2) (1984).
[17] Elbadry, M. and Ghali, A., 'Thermal stresses and cracking of concrete bridges', *ACI Journal* **83** (6) (1986) 1001-1106.
[18] Van Mier, J.G.M. and Vervuurt, A., 'Lattice model for analyzing steel-concrete interface behaviour', in 'Mechanics of Geomaterials Interfaces', Selvadurai, A.P.S. and Boulon, M.J., Eds. (Elsevier Science Publishers, Amsterdam, 1995) 201-225.
[19] Zimbelmann, R., 'A contribution to the problem of cement-aggregate bond', *Cem. & Conc. Res.* **15** (5) (1985) 801.

Article n°5

Internationale Zeitschrift für
Bauinstandsetzen
4. Jahrgang, 1 - 15, (1998)

Combined Experimental and Numerical Study to assess Shrinkage Cracking of Cement-Based Materials

G. Martinola and H. Sadouki
Laboratory for Building Materials
ETH Zürich

Abstract

In this contribution, a combined experimental and numerical study to assess the cracking resistance of cement-based materials subjected to desiccation is outlined. Experimentally, the tendency to hygral cracking is determined by means of mortar ring specimens exposed to drying atmosphere. A numerical model based on the nonlinear theory of diffusion and nonlinear fracture mechanics is developed. The relevant hygral and mechanical parameters and laws needed for the model have been determined by means of adequate experiments analyzed by inverse analyses. The hygro-mechanical behaviour of two different types of mortar is studied. Numerical results have been compared to experimental findings. Furthermore, a parametric study has been carried out with the aim to characterize the relevant material parameters influencing shrinkage cracking. It can be concluded that a combination of experimental and numerical methods can play a decisive role in optimizing mortars or concretes with respect to predefined and required material properties. In this way, the durability of concrete structures can be significantly enhanced.

Key words: Shrinkage, diffusion, drying, endogeneous shrinkage, humidity profiles, cracking, numerical model, material parameters, material laws

Kombinierte experimentelle und numerische Studie zur schwindinduzierten Rissbildung zementgebundener Werkstoffe

Zusammenfassung

In diesem Beitrag wird eine experimentelle und numerische Studie zum Risswiderstand von zementgebundenen Baustoffen unter Austrockungsbedingungen vorgestellt. Die Tendenz der hygrischen Rissbildung ist experimetnell mit Hilfe eines unter trocknenden Bedingungen gelagerten Mörtelringes ermittelt worden. Ein Modell, dessen Grundlage die nichtlineare Diffusionstheorie und die nichtlineare Bruchmechanik sind, wurde entwickelt. Die wichtigsten hygrischen und mechanischen Parameter und Werkstoffgesetze, die für das Modell benötigt werden, sind mit Hilfe angepasster Messmethoden in Verbindung mit der inversen Analyse bestimmt worden. Das hygro-mechanische Verhalten von zwei unterschiedlichen Mörteltypen wurde untersucht. Die numerischen Ergebnisse wurden anschliessend mit den experimentell ermittelten verglichen. Zusätzlich wurde eine Parameterstudie mit dem Ziel durchgeführt, die für die Rissbildung empfindlichsten Werkstoffparameter zu finden. Es wurde gezeigt, dass kombinierte experimentelle und numerische Methoden eine entscheidende Rolle bei der Optimierung von Mörtel oder Beton spielen können und so einen Beitrag zu verbesserter Dauerhaftigkeit von Tragwerken leisten.

Stichwörter: Schwinden, Diffusion, Austrocknung, endogene Trocknung, Feuchtigkeitsverteilung, Rissbildung, numerisches Modell, Werkstoffparameter, Werkstoffgesetze

G. Martinola, graduated in 1993 in Materials Engineering at ETH Zürich. Member of the staff at Istituto Tecnico Sperimentale in 1993-94. Since September 1994, Research Assistant at Laboratory for Building Materials, ETH Zürich.

Dr. H. Sadouki, graduated in Physics at EPF Lausanne. Ph.D Thesis in Materials Sciences at EPF Lausanne in 1987. Since 1988 Research Assistant at Institute for Building Materials. His main interset and experience are in field of numerical simulation of fracture mechanics and fluid transport in cement-based materials.

1 Introduction

The durability of concrete structures is strongly related to the penetration of water into the concrete structure. Water often contains substances which once transported into the porous system of concrete can damage the concrete structure by various external or internal mechanisms. To increase the durability of concrete structures means essentially to abate the penetration of water into the structure. This means also a reduction of the number of cracks and in case of cracks a minimal crack opening. Because of their specific applications in service, some concrete structures like cellars or water containers need to be completly free of cracks. In the domain of building restauration deteriorated or contaminated concrete layers have often to be removed from existing structural elements and subsequently replaced by new concrete or mortar. In most cases an empirical approach is chosen instead of an engineering analysis and rigorous design, so that failures of some systems, e.g. cracks in the overlay and delamination of the overlay, occur requiring the repair of repair systems.

Fresh concrete is mixed with typically 120 to 170 litres of water per cubic meter. Part of this water is consumed during hydration; the remaining part is still enough to supply the young porous concrete with a moisture content which is in hygral equilibrium with 95-100 % relative humidity. Concrete structures are usually exposed to much lower humidities. As a consequence a long-lasting drying process starts immediately after demoulding. A concrete layer contracts during the drying process. In this layer a hygral gradient originates a stress field if the concrete layer is restrained in a statically undeterminated system. Tensile eigenstresses can overcome the tensile strength even for moderate environmental drying conditions. In this case crack formation occurs. So cracking in concrete structures due to shrinkage is a complex matter involving the shrinkage rate, the restraint level, creep properties, Young's modulus of elasticity and fracture mechanics parameters of concrete. All of these material properties develop with time. The aim of concrete designers is to generate a concrete mix with reduced shrinkage in order to guarantee a low probability of crack formation [1].

In this contribution a restrained shrinkage ring test [2,4,5,6] which allows to quantifiy shrinkage behaviour is presented. A sensitivity analysis of the material properties is carried out in order to identify the influence of these properties on shrinkage cracking. The analysis and the evaluation of the test results give us the possibility to optimize shrinkage of cement-based materials.

2 Theoretical basis of the hygro-mechanical behaviour of cement-based materials

2.1 Physical description of drying

Moisture variations in cement-based materials may result from internal drying induced by the hydration reaction of cement and water at early age (self-desiccation) , and from drying caused by climatological conditions of the environment during the life-span of the structure. The knowledge of moisture distributions in space and time in a structure is of utmost importance for analyzing crack formation and further crack growth.

The size and the shape of pores present in a porous material exert a direct influence on the transport mechanism of water. Despite the knowledge of the basic individual phenomena involved, like capillary transport, diffusion, surface diffusion, etc., it is not yet possible to assess quantitatively the influence of each of them on the global moisture transfer in a porous material such as concrete or mortar. At the macroscopic level (i.e. in a representative finite volume of the porous and heterogeneous structure), the aforementioned difficulty can be circumvented by defining a concentration-dependent transfer coefficient, which integrates all contributions of the different mechanims in the global mass transfer . In this phenomenological description, the transient moisture flow can be described according to the second Fick's law [7,8]. If h represents the relative humidity held in the pores, then Fick's law is described by the following partial differential equation :

$$\frac{\partial h}{\partial t} = div\left[D(h) \cdot \vec{grad}(h) \right] \tag{1}$$

in which D(h) is the moisture transfer coefficient depending on the pore humidity h and on the composition of the cement-based material.

Equation(1) describes in a realistic way the transient moisture flow in normal matured concretes with relatively high water-cement ratio in which self-desiccation can be neglected (w/c $\geq$ 0.5). However, for young cement-based materials with low w/c ratio, the available water is less than required to maintain equilibrium with a relative humidity of around 100%, self-desiccation than plays an important role. In order to take into account the contribution of the endogeneous drying in the description of the drying process, a moisture-sink term $q(t_0,t)$ as function of the hydration time t_o is added to the right-hand side of Equation 1. The extended equation governing the global drying process is then written as follows:

$$\frac{\partial h}{\partial t} = div\left[D(h) \cdot \vec{grad}(h) \right] + q(t_0, t) \tag{2}$$

For calculating the drying process of a porous system exposed to a given atmosphere, equation (2) must be solved coinjointly with adequate boundary conditions and initial conditions.

In general, convective boundary conditions are used to describe the exchange of humidity between the exposed surfaces of the system and the surrounding atmosphere. This condition is expressed as follows:

$$\vec{j}_n = \gamma \cdot (h_\Gamma - h_0) \cdot \vec{n} \quad \text{on } \Gamma \tag{3}$$

with $\vec{j}_n$ = moisture flux normal to the exposed surface Γ
γ = hygral convection coefficient
h_Γ = humidity on the surface Γ
h_0 = humidity of the surrounding atmosphere

In general, γ depends on many factors, such as the actual humidity, the temperature and the speed of the wind at the convective surface. In this analysis, a constant mean value of γ will be used, this is justified in our case because the specimens are assumed to be exposed to a constant atmosphere.

The initial condition describing the spatial humidity field in the porous structure at the beginning of the exposure to a drying atmosphere is given by means of the following set of equations:

$$h(t = 0, x_i, y_i, z_i) = h_i \tag{4}$$

with (x_i, y_i, z_i) = localisation of a point in the volume
h_i = corresponding humidity potential value at the beginning of the analysis

This value takes into account the moisture loss induced by the autogeneous desiccation before the structure is exposed to the atmosphere.

2.2 Description of the hygro-mechanical behaviour

In this contribution, hygral variations induced by endogeneous or/and exogeneous desiccation are considered as the only driving force for crack formation and propagation. During drying of a cement-based material, hygral gradients will develop, inducing differential deformations in the specimen. If a hypothetical fibre of the material is free to shrink under an infinitesimal drop Δh in humidity, the resulting shrinkage strain can be expressed as follows:

$$\Delta\varepsilon_{h.sh.} = \alpha_{h.sh.}(h) \cdot \Delta h \tag{5}$$

with $\Delta\varepsilon_{h.sh.}$ = infinitesimal free shrinkage
$\alpha_{h.sh.}(h)$ = coefficient of shrinkage depending on the material composition and on the actual pore humidity.

If the drying material is restrained with respect to shrinkage, tensile eigen-stresses will develop. Often, these tensile stresses are large enough to cause cracking, and adequate fracture mechanics tools must then be applied. Elastic-softening models can describe crack formation and crack growth in cement-based materials in a realistic way. Models incorporating softening are mostly based on the Fictitious Crack Model (FCM) originally developed by Hillerborg and co-workers [9]. In this model, the stress-deformation diagram under tension is split in a pre-peak stress-strain diagram, which is characterized by the Young's modulus E of the material and the tensile strength f_t, and post-peak behaviour. After the maximum stress is reached bifurcation occurs. Within the fracture process zone (FPZ) strain softening takes place while outside this zone the material continues to react linear elastic. The post-peak relation is fully characterised by the shape of the softening curve. The area under this curve is the fracture energy G_f. The model is shown schematically in Figure 1.

The Crack Band Model (CBM) as developed by Bazant and Oh [10] is quite similar, except that it assumes that the crack growth occurs in a band, rather than

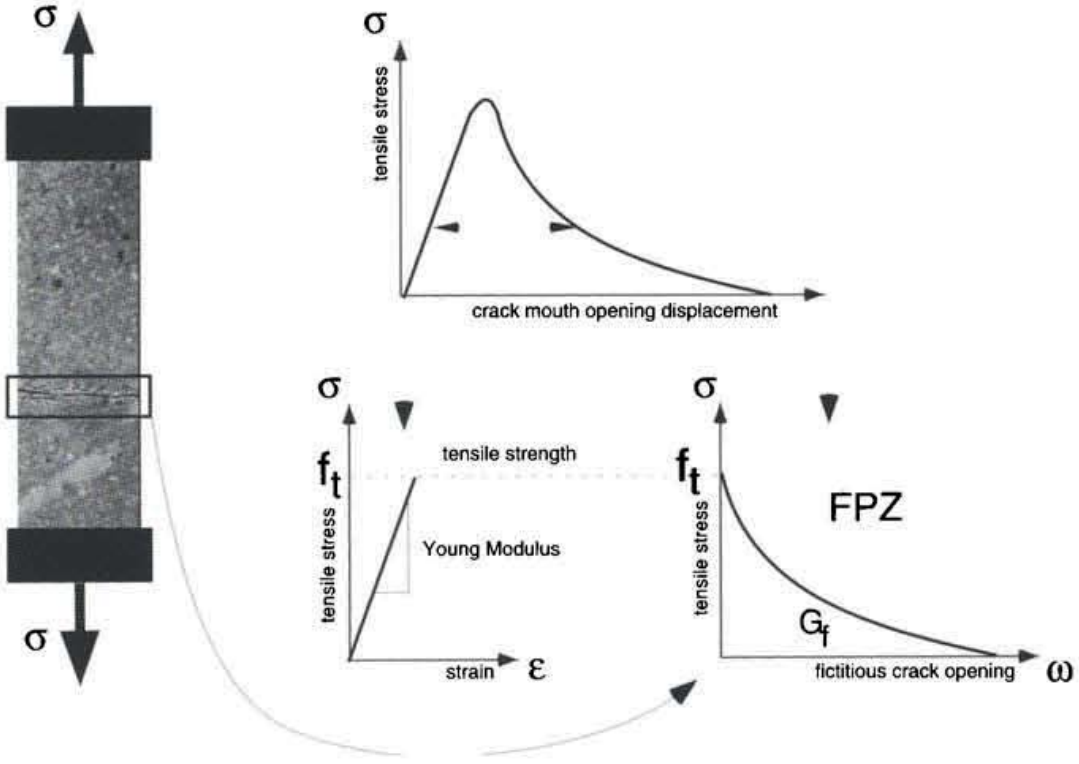

Fig. 1: Basic elements of the fictitious crack model

along a line. The CBM forms the basis for the smeared crack model in the finite element code DIANA [11,3,12] used in this work.

During the period of the hygral loading, the deformations of the material increase due to creep. Creep can be described by means of visco-elastic models (Kelvin chains). The visco-elastic relation between strain and stress is derived in our case from measured creep curves, which describe the instantaneous and transient strain after a unit force loading. The properties of Kelvin chains are then obtained by curve fitting of the measured creep function [11].

3 Description of the ring-test model

3.1 Experimental set-up

Different experimental techniques are used to assess the resistance against cracking of cement-based materials when subjected to restrained drying shrinkage. The restrained ring type test is used in our case [2,4,5,6].

The technique consists of casting a ring of mortar around a very stiff ring specimen. Figure 2 shows schematically a 2D representation of the ring specimen. After a preliminary curing period, the two sides of the mortar ring are sealed. The

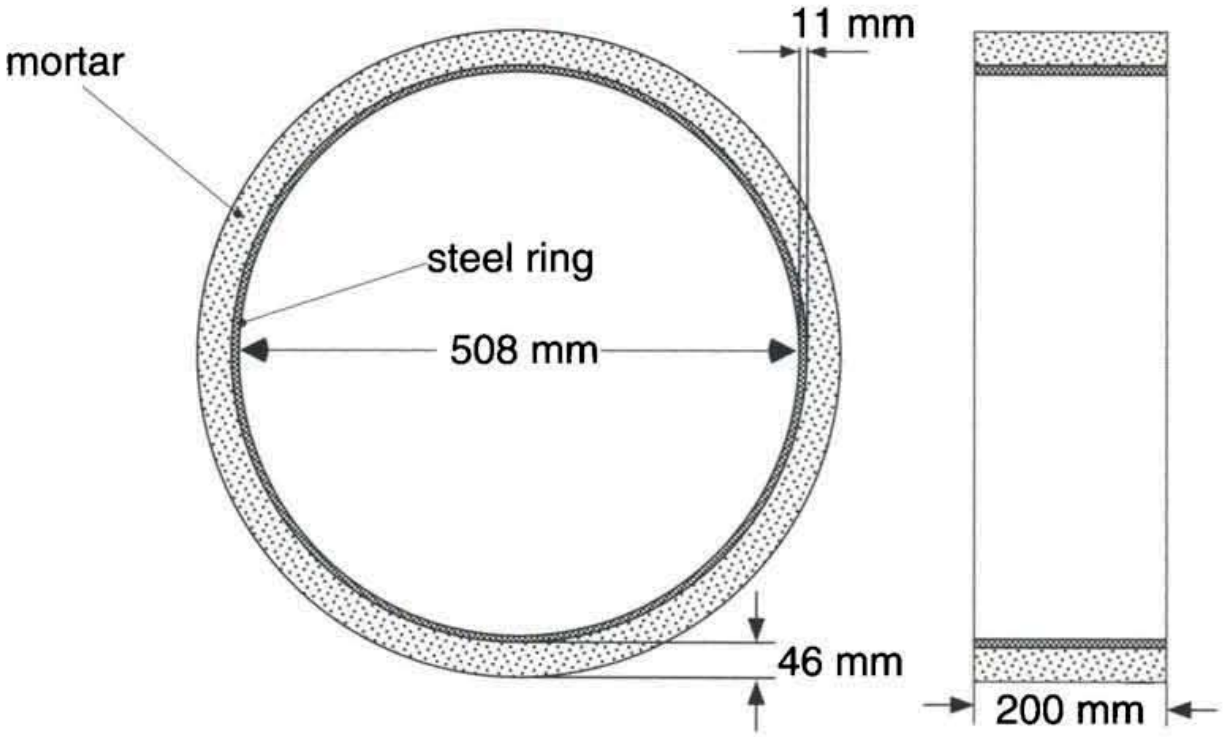

Fig. 2: 2D representation of the ring specimen

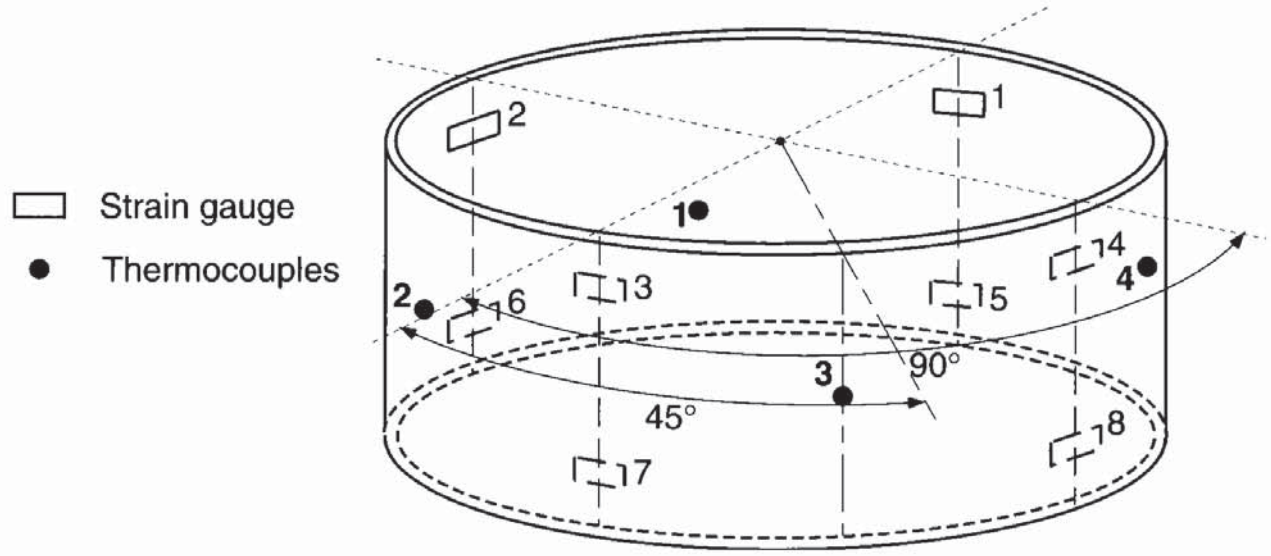

Fig. 3: Localization of the strain gauges on the inner surface of the steel ring and of the thermocouples

ring is then exposed to a given drying atmosphere (T=20°C, 45% R.H). Under these conditions, drying is allowed only through the outer circumferential surface. Due to hygral shrinkage, the mortar ring attempts to contract against the restraint of the steel ring.

The mortar rings are 46 mm in radial thickness and 200 mm in heigth. The internal and external diameters of the steel ring are 508 and 519 mm respectively. Several strain gauges are placed at different positions on the inner surface of the steel ring. Figure 3 shows the positions of the strain gauges and positions of thermocouples. Deformations on the steel are then recorded automatically as function of the drying time.

3.2 Numerical modelling

As mentioned before the non-linear finite element programme DIANA [11] has been used to simulate the combined flow-stress analysis. The analysis is performed in 2D (radial moisture diffusion only). Figure 4 shows the finite element idealization of the steel-mortar ring specimen. During the flow analysis, finite elements representing the steel are removed and no moisture flux is allowed through the inner surface of the mortar ring.

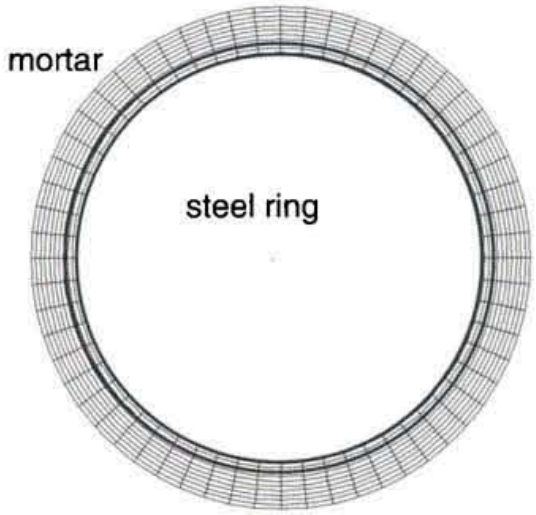

Fig. 4: FE idealization of the ring specimen

In DIANA, the global deformation field ε is split up in four components as follows:

$$\varepsilon = \varepsilon^{el.} + \varepsilon^{crack} + \varepsilon^{creep} + \varepsilon^{h.sh.} \tag{6}$$

with
- $\varepsilon^{el.}$: elastic strain
- ε^{crack} : crack strain
- ε^{creep} : creep strain
- $\varepsilon^{h.sh.}$: hygral shrinkage strain

The calculated time-dependent humidity distribution from the transient analysis is stored in a file for every time step Δt. For the stress and fracture analysis, the incremental hygral load Δh is converted to a strain field ($\varepsilon^{h.sh}$) via the hygral shrinkage coefficient α(h). The two analyses are un-coupled, meaning that it has been assumed that the moisture flow is not affected by cracking.

The multiple fixed smeared crack approach developed by Rots [13] is used to simulate the crack formation and growth in the mortar ring. As mentioned, the smeared crack model is a band in the spirit of the Bazant and Oh model [10]. The strain is decomposed in an elastic part and a crack strain. The crack strain is obtained by dividing the crack opening by the crack band width, which is the size of

the finite element. Due to the cracking of the material the shear stiffness is usually reduced, this is taken into consideration by correcting the shear modulus G by a reduction factor β. Crack initiation is governed by a linear tension cut-off criterion and a threshold angle between two consecutive cracks. A detailed description of the model can be found in Rots [13]. The shape of the stress-crack opening is assumed to be bilinear, the parameters are obtained by an inverse analysis of the load-displacement diagram measured on wedge-splitting test specimens. The main characteristics of the used crack modeling are schematically shown in Figure 5.

As it has been mentioned, creep is described by the visco-elastic theory. In

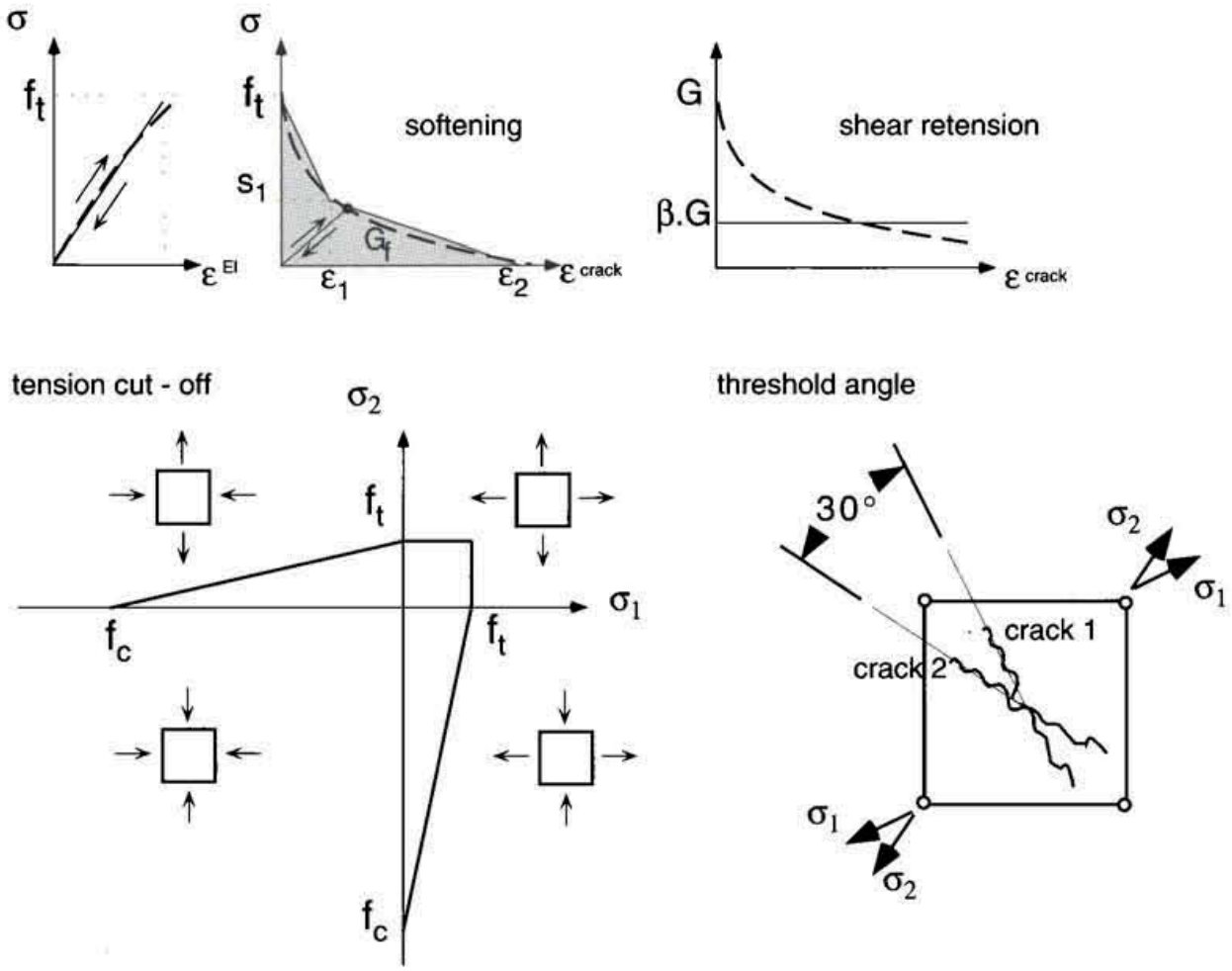

Fig. 5: Characteristic of the crack model

calculating time dependent strains, the history of the stresses must be taken into account. By assuming the principle of superposition (Boltzmann), one obtains the classical Volterra integral equation:

$$\varepsilon(\tau) = \int_{-\infty}^{t} J(t,\tau)\overline{C}\,\dot{\sigma}(\tau)\mathrm{d}\tau \tag{7}$$

where t : time
τ : loading duration
$J(t,\tau)$: creep function
$\overline{C}$: compliance matrix
$\dot{\sigma}(t)$: stress rate

The material behaviour is characterized by the creep function $J(t,\tau)$. This can be expressed as a sum of exponential functions (Dirichlet series). Physically the Dirichlet series can be interpreted as a Kelvin chain model.

$$J(t,\tau) = \sum_{\alpha=0}^{\infty} \frac{1}{E_\alpha}\left[1 - e^{-\frac{t-\tau}{\lambda_\alpha}}\right] \qquad \text{with } \lambda_\alpha = \frac{\eta_\alpha}{E_\alpha} \tag{8}$$

where E_α : equivalent stiffness
λ_α : retardation time
η_α : viscosity

The stiffnesses E_α and retardation times λ_α of the units in the chain are estimated from the measured creep curve by a nonlinear least squares method. More details on this approach can be found in [11].

In this numerical simulation statistically distributed mechanical properties of the mortar are introduced. This leads to realistical localization processes. The Young's modulus (E) and the tensile strength (f_t) are assumed to be randomly distributed over all finite elements representing mortar. A scatter of 10% and 20 % of the mean values of E and f_t respectively are assumed, in accordance with the measured standard deviations of these properties. The random variables E and f_t are adequately correlated by forcing them to follow the same statistical distribution over the finite elements.

4 Material properties for the numerical analysis

4.1 Composition of mortar

In this contribution two different mortars are investigated. The first one is a standard mortar with 0-4 mm aggregate size. The second one is a special mortar developped for repairing concrete structures. In this case the mechanical properties are optimized in order to reach low elastic modulus and high fracture energy. Carbon fibers, superplastizers (SP), air entraining agents (AEA), polymer dispersions (PD) were added. The mix-design of the two mortars is shown in table 1.

4.2 Hygral properties

Cylindrical specimens were drilled after two days of hydration and prepared for radial drying. These specimens were stored in different ambient humidities with constant temperature. The moisture loss was measured periodically as function of drying time. The experimental data was used for the determination of the diffusion coefficient by means of an inverse analysis [14]. The moisture diffusivity is described by an exponential function of humidity with two parameters a and b:

$$D(h) = a \cdot e^{(b \cdot h)} \tag{8}$$

with a, b : Parameters
h : Humidity potential

The moisture diffusion coefficients of the two mortars are given in Fig. 6.

Table 1: Composition of standard and optimized mortar

	aggregate size [mm]	w/c [-]	cement [kg/m³]	Aggregate [kg/m³]	Fibers [%]*	P.D. [%]	HP.P. [%]*	A.E.A. [%]*
Stan. mortar	0-4	0.5	500	1500	-	-	-	-
Opt. mortar	0-6	0.36	375	1620	1	15	1.2	0.2

* of the cement weight

with P.D. : polymer dispersion
HP.P. : high performance plastizer
A.E.A. : air entraining agents

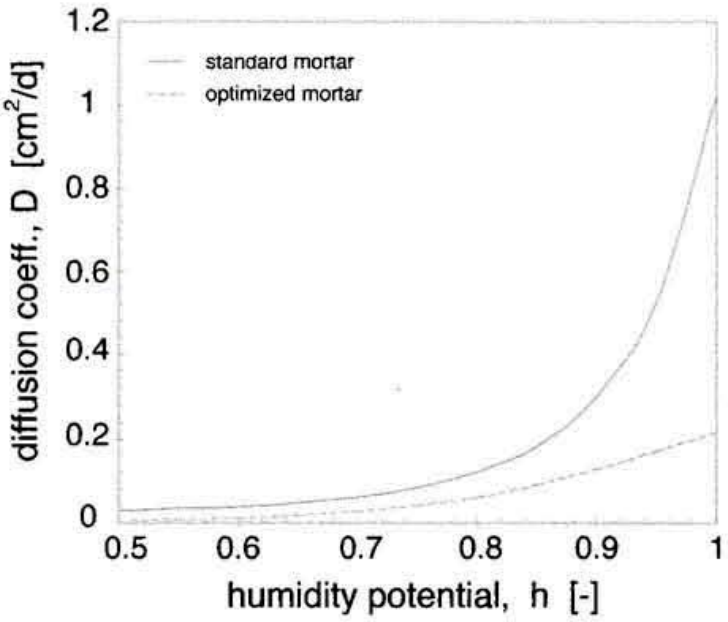

Fig. 6: Moisture diffusion coefficients of the standard and optimized mortar

Mortars with a low w/c ratio are subject to internal drying. This phenomenon was measured on sealed specimens with capacity sensors. The standard mortar does not present this characteristic of self-desiccation, because of its comparatively high water-cement ratio. Figure 7 shows the evolution of the pore humidity as function of the age for both mortars. In the optimized mortar, the endogeneous drying will finally reduce the internal humidity to approximately 75%.

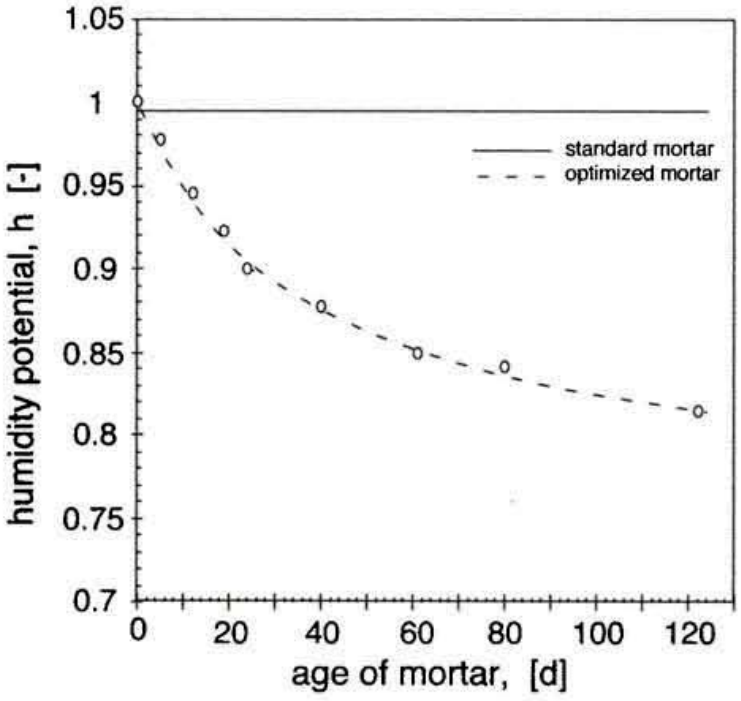

Fig. 7: Decrease of pore humidity due to self dessication

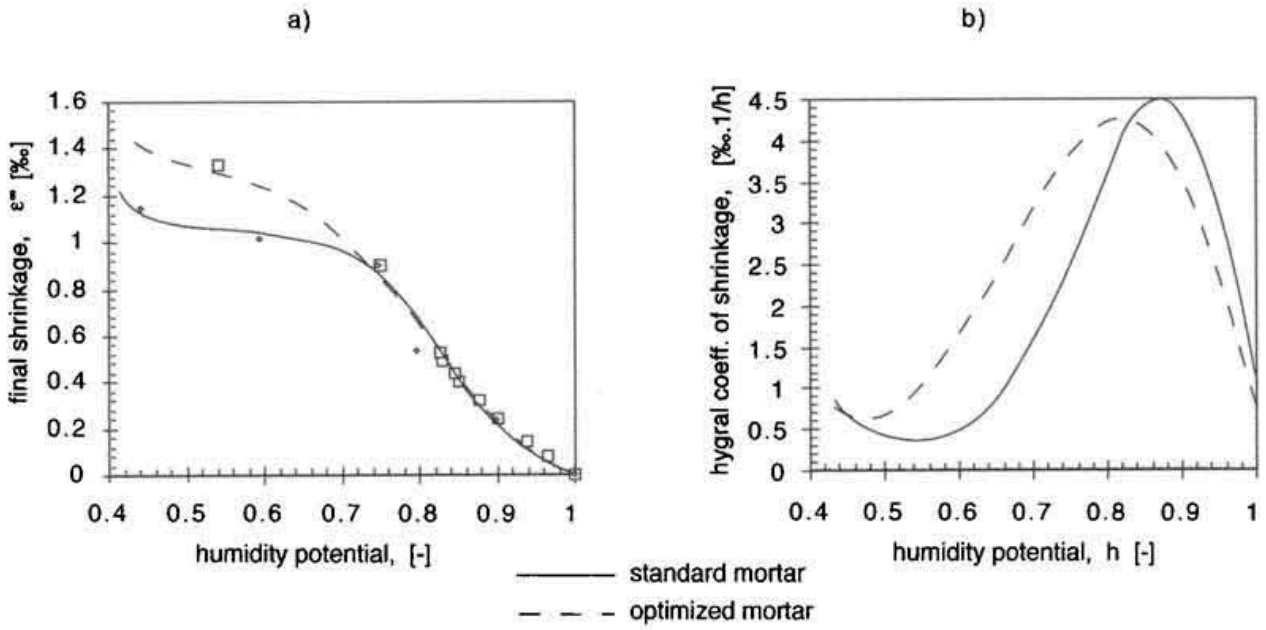

Fig. 8: a) Final shrinkage and
b) hygral shrinkage coefficient as function of humidity

The moisture sink term $q(t_0,t)$ is obtained by derivation of the time dependent humidity decrease function (see Figure 7):

$$q(t) = \frac{dh}{dt} = -\frac{0.358}{(43.8+t)^2} + \frac{0.358}{43.8+t} \tag{9}$$

The total hygral deformation is induced by external drying shrinkage and internal autogeneous shrinkage. The humidity dependent final shrinkage was measured on cylindrical specimens exposed to different relative humidities. The obtained experimental data are fitted. The results are given in Figure 8 a).

The hygral shrinkage coefficient (Figure 8 b) is calculated by the first derivation of the final shrinkage curve with respect to humidity potential h :

$$\alpha_{sh.}(h) = \frac{d\varepsilon^{t\to\infty}(h)}{dh} \tag{10}$$

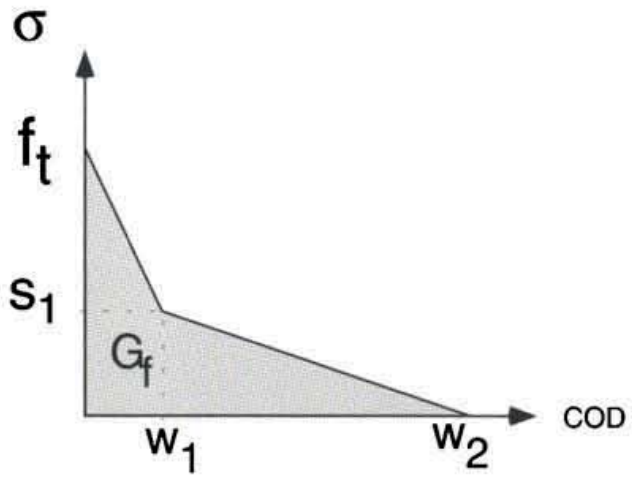

Fig. 9: Bilinear stress crack-opening diagram

4.2 Mechanical properties

The moduli of elasticity of the mortars are measured on cylindrical specimens tested under compression.

The determination of fracture parameters such as fracture energy and strain softening has been performed by means of the wedge splitting test described in [15]. An inverse analysis allows the computation of the parameters of the bilinear softening diagram [16]. These parameters f_t, σ_1, w_1, w_2 are indicated in Figure 9.

The mechanical properties of the two mortars measured at the age of 7 days are shown in Table 2.

Creep functions were measured on prismatic specimens. The mortars were 3 days old at the time of loading. Half of the number of the specimens were completely sealed, the others are exposed to a drying atmosphere of 70% relative humi-

Table 2: Mechanical properties of standard and optimized mortar

	G_f [N/m]	E [GPa]	f_t [MPa]	s1 [MPa]	w1 [mm]	w2 [mm]
Stand. mortar	52.	29.0 ± 2.9	2.1 ± 0.39	0.37	0.026	0.134
Opt. mortar	288.	20.0 ± 1.9	4.4 ± 0.42	0.53	0.090	0.350

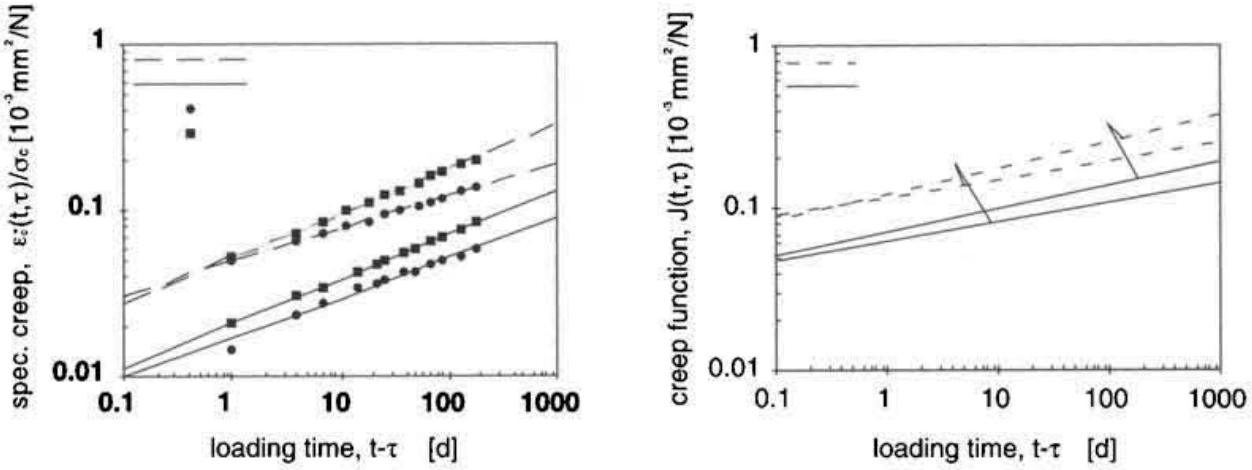

Fig. 10: Basic and drying creep functions

dity. The specimens were then loaded in compression with a stress level of 35 % of their expected compressive strength and the deformations were recorded as function of loading time. The measured basic creep and drying creep curves are given in Figure 10.

5 Numerical simulation and validation of the proposed model

5.1 Humidity distribution

Figures 11 a) and 11 b) show the simulated radial humidity profiles in the two mortar ring specimens for six drying times. In the case of the standard mortar (Figure11a), the pore humidity at the beginning of exposure to the drying was in equilibrirum with a relative humidity of 100%. In the case of fiber reinforced mortar, this value was 97.5 % only, due to the self-desiccation during the curing period (see Figure 11b). By comparing the profiles of the materials, one can clearly see that in case of the standard mortar the hygral gradient, at a given drying time, increases slowly from the inner to the outer surface. In the second case, because of the self-desiccation of the material (low w/c ratio), humidity distributions show a large plateau region, but high hygral gradients occur at the outer layers near the exposed surface.

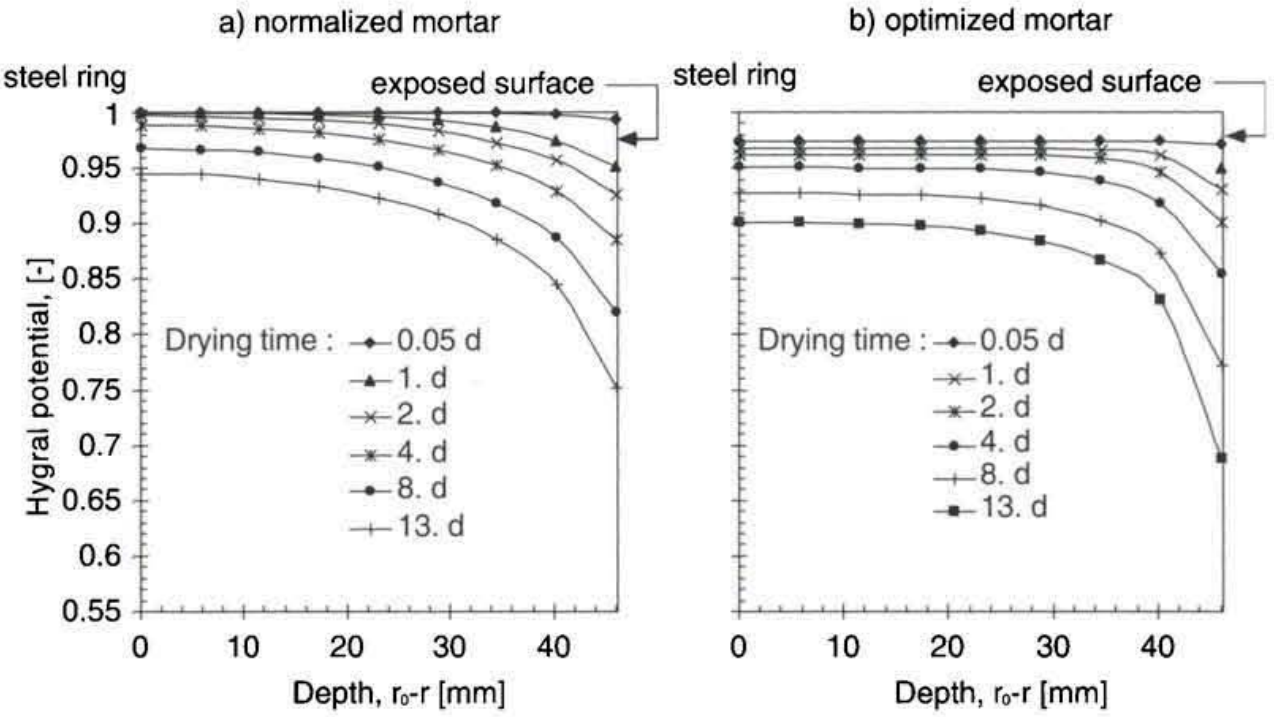

Fig. 11: a) Moisture distribution at different drying times of the standard mortar
b) Moisture distribution at different drying times of the optimized mortar (with endogeneous drying)

5.2 Crack formation and propagation

5.2.1 Standard mortar

Results of the numerical simulation are shown in Figure 12. In the standard mortar ring, the first fictitious cracks appear on the outer layer of the ring, the region with the highest hygral gradients, already at t = 0.9 day after the exposure. Note, that these cracks still can transfer load, they must be regarded as local fracture process zones where microcracking and crack bridging occur. During the next time steps the fictitious cracks gradually increase in width. As the drying process proceeds, cracking is governed by two phenomena, namely a number of cracks, closely positioned with respect to one another disappear (close), whereas other more distantly distributed cracks continue to grow at certain integration points of the elements of the outer layers of the ring. At t = 5.6 days a well defined microcracked band is formed and runs radially from the outer surface of the mortar to the inner steel ring surface. From this cracked band the first macrocrack is developed. About 2.2 days later (t = 7.8 days), a second macrocrack is formed in another region of the ring nearly opposite the first crack. After that the two macrocracks increase gradually in width and microcracking occurs in the inner layer of

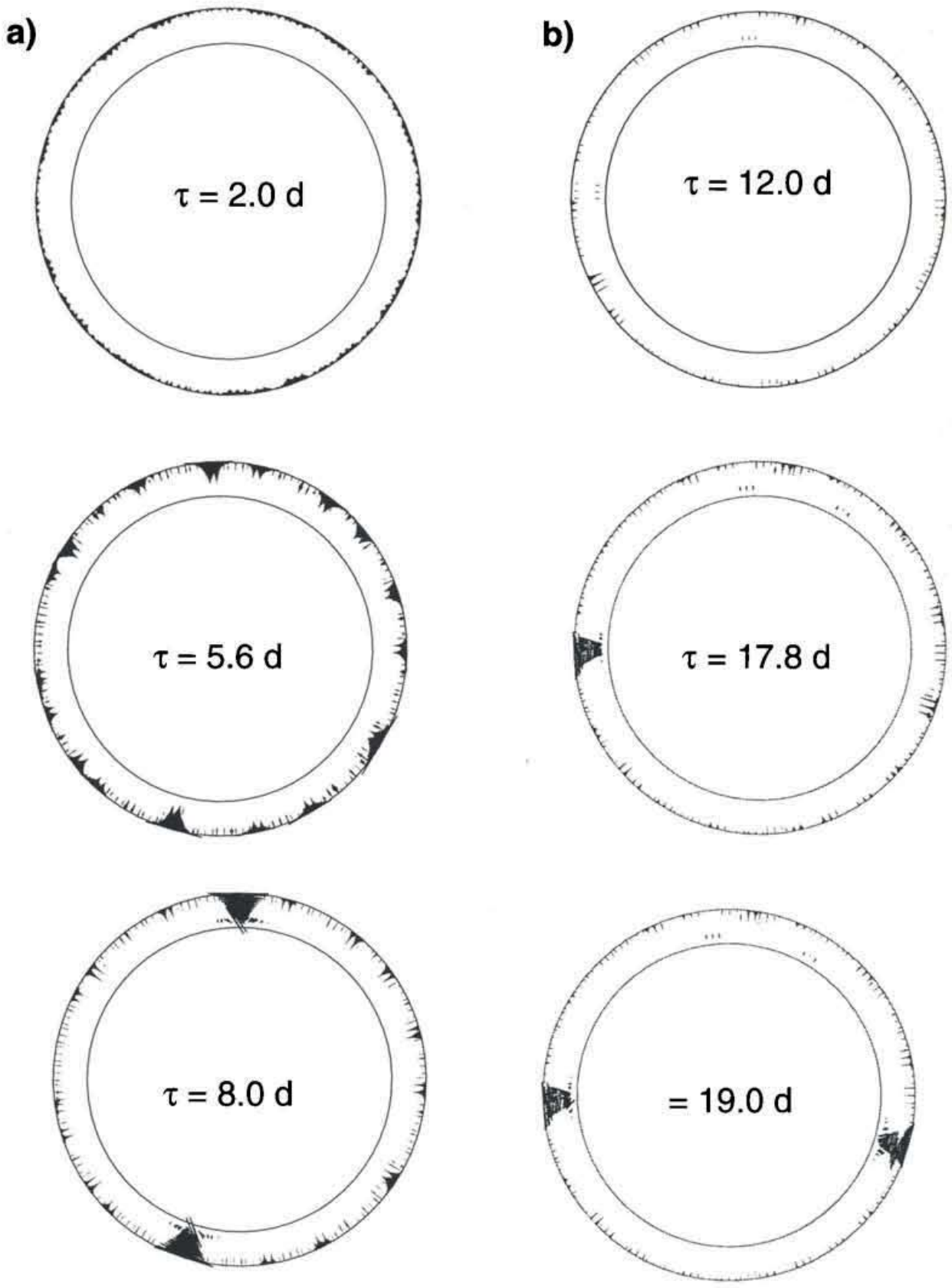

Figure 12: Evolution of cracking at different drying times of a) standard mortar b) for optimized mortar

the mortar where the macrocracks hit the steel ring. This type of crack evolution is similar to that obtained for a concrete repair system subjected to drying [12]. Figure 12a shows crack strains at Gauss points obtained by numerical simulation at three different drying times, 2, 5.6 and 8 days.

In the corresponding experiment, the first macrocrack appeared at 5.2 days and a second one at 11 days. Unfortunately, with the used experimental set-up it was not possible yet to follow the evolution of the crack opening, only an estimation of the width of the visible cracks was possible. The exact occurrence of the two real cracks was made possible by analyzing the time evolution of the strains recorded at different positions on the inner surface of the steel ring.

5.2.2 Optimized mortar

A similar numerical analysis has been performed for the fibre reinforced mortar ring. Figure12b) shows schematically the distribution of the crack strains at Gauss points at 3 different drying times, t = 12, 17.8 and 19 days. The evolution of the cracking process is analogue to the former case (standard mortar). Nevertheless, the first dispersed fictitious cracks appeared later, namely 7 days after the start of the drying of the specimen. This can be explained by two main reasons: (1) lower moisture diffusivity, and (2) higher tensile strength and lower E-Modulus as compared to the standard mortar. The first real macrocrack (band of real cracks) occurred at t=17.8 days (see Figure 12b). Two days later a second fictitious crack grow up significantelly, but only 9 days later becomes a real crack (see also Figure

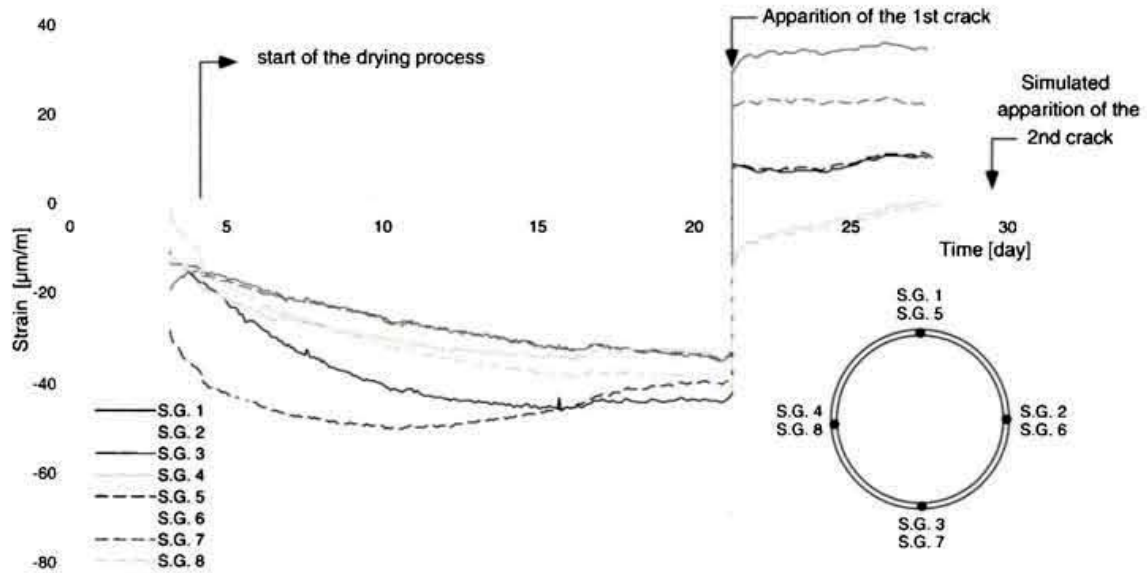

Fig. 13: Evolution of the tangential strain of the steel measured by means of strain gauges for the optimized mortar

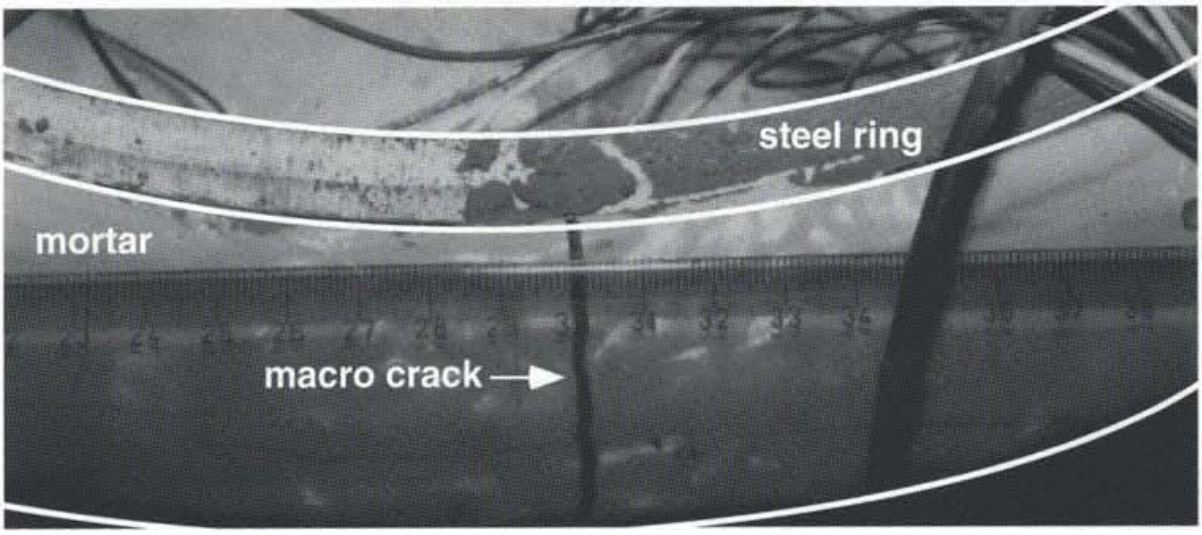

Fig. 14: Photography of the macrocrack after 20 days of drying for the optimized mortar

15). At further drying, most of the dispersed fictitious microcracks close and the two real macrocracks increase in width. In the case of the corresponding experiment, one macrocrack occurred only and suddenly after a drying time of 17.5 days with a measured width of 2 mm. The second crack was not observed as was the case in the numerical simulation because the experiment came to an end before its apparition.

Figure 13 shows the steel strains recorded as function of drying time, for the

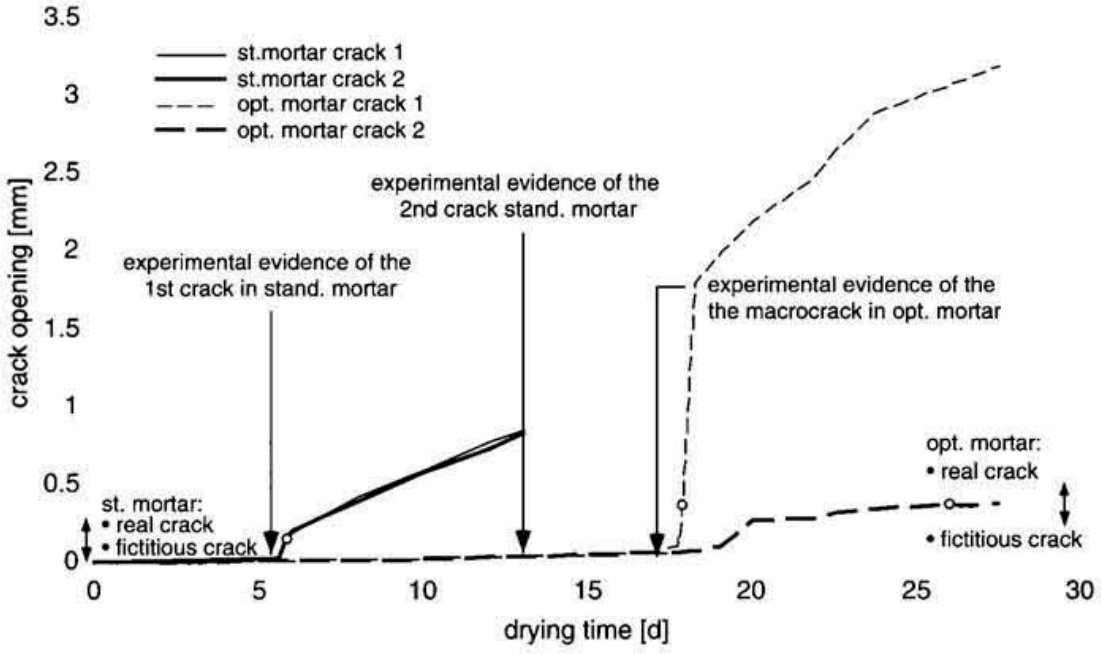

Fig. 15: Simulated crack opening as function of the drying time

test of optimized mortar. The brutal jump in the curves has to be related to the apparition of a macrocrack (unloading of the steel ring), in this case this jump appeared at 17.8 days. A photography of this macrocrack, after a drying time of about 20 days is shown in Figure 14. The opening of this macrocrack agrees quite well with numerical results (see Figure 15). Figure 15 shows the simulated crack opening as function of the drying time for the two analyzed rings.

6 Parametric study

Based on the quite good agreement between the experimental results performed on two mortars with totally different hygro-mechanical properties and the corresponding numerical results obtained by the proposed model, a numerical parametric study has been carried out.

The main aim of this study is to define the most relevant material parameters influencing shrinkage cracking and consequently to be able to decide which material parameter(s) must be optimized in order to try to reduce the risk of damage as far as possible.

Because of the large number of the material parameters involved in the cracking process and their mutual interaction, in each simulation one or two material parameters only are varied while the others are kept constant equal to the reference values. As far as possible, the material parameters, considered as variables, are changed in a reasonable way, meaning that a „real" mortar having these hypothetic propreties can be made.

The reference values of the hygro-mechanical properties are listed below:

- Young modulus $E = 25$ GPa
- Tensile Strength $f_t = 3.0$ N/mm^2
- Fracture energy $G_f = 97.5$ N/m
- Softening parameters $s_1 = 0.5$ N/mm^2
  $w_1 = 0.04$ mm
  $w_2 = 0.15$ mm
- Diffusion coeff. $D(h) = a_0 \cdot \exp(b_0 \cdot h)$ cm^2/d
  $a_0 = 0.00005$
  $b_0 = 10$
- Coeff. of shrinkage $\alpha_0(h) = -a \cdot (h-c)/b^2 \cdot \exp(-0.5 \cdot ((h-c)/b)^2)$ ‰/h
  $a = 0.953$
  $b = 0.204$
  $c = 1.042$

In the following parametric study, the varied material parameters are given in the corresponding figures. The final result of each study consists of curves showing the evolution of the crack opening of the most dominant crack in the mortar ring as function of the drying time.

In a first analysis, the influence of the moisture diffusivity on the crack evolution has been studied. Three different moisture diffusivities are considered as it can be seen in Figure 16a. In Figure 16b, the resulting crack opening as function of drying time is shown. It is evident from this figure that the moisture diffusivity plays an important role in the crack formation. These main conclusions can be drawn: the apparition of the first damage (first fictitious cracks) is delayed at low moisture diffusivity and for a given drying time, the crack opening is an increasing function of the moisture diffusivity.

In order to measure the importance of the moisture-dependent coefficient of shrinkage a(h) with respect to the risk of cracking, the peak value (a_0) of the function a=a(h) has been varied, the resulting curves are shown in Figure 17a. In Figure 17b, the corresponding results regarding the cracking evolution as function of the drying time are shown. It can clearly be seen as it can be anticipated that the coefficient of shrinkage has a very strong influence on the crack formation. For low values ($a \leq a_0/4$) of this material parameter, cracking becomes insignifiant.

In a next study, two parameters are varied at the same time, the Young´s modulus E and the coefficient of shrinkage a(h). In Figure 18a, a is equal to the reference value a_0 and three different values are assumed for the Young´s modulus. As it can be seen in this figure, in all cases the cracking is extremly severe, depending on the Young´s modulus at least one real crack (crack-opening w higher than w_2 of the bilinear diagram) is formed after a drying time between 45 and 60

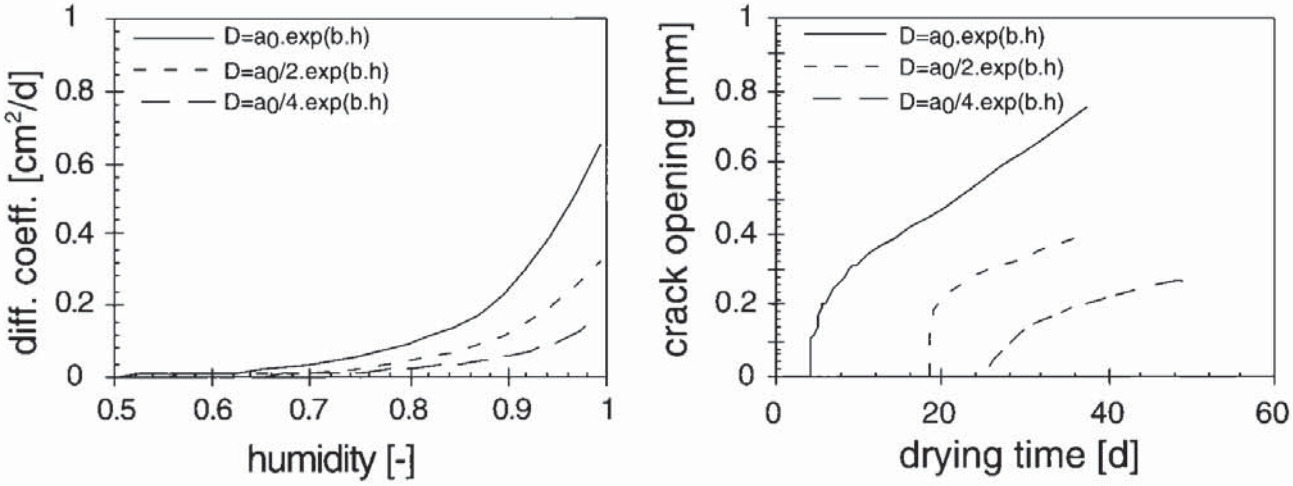

Fig. 16: a) Moisture diffusivities as function of humidity
b) Corresponding crack opening as function of drying time

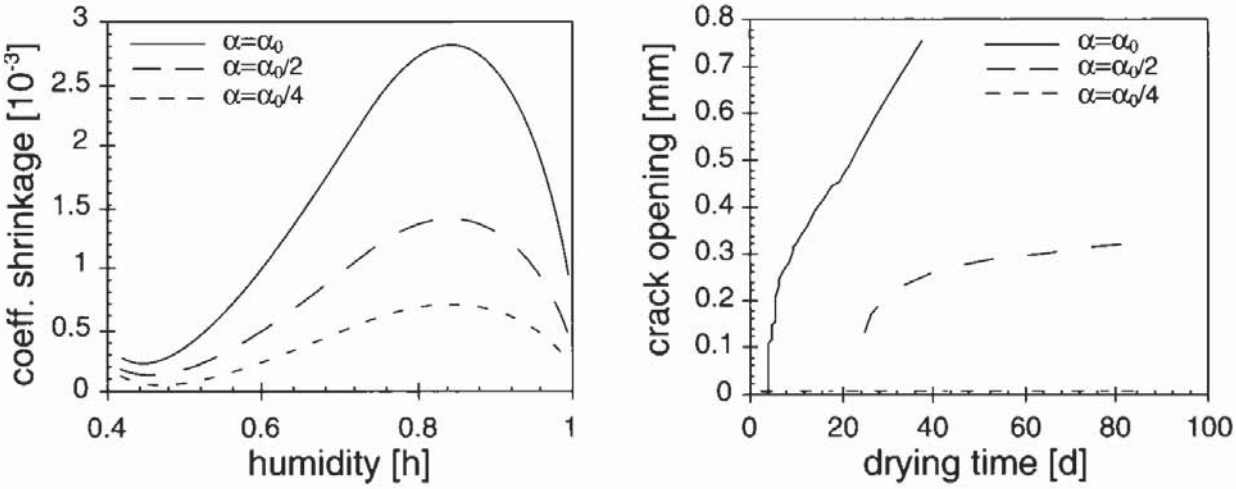

Fig. 17: a) Three different functions for the coefficient of shrinkage as function of humidity
b) Crack opening as function of drying time for the three shrinkage function shown in Figure 17 a)

days. As the drying process progresses, the cracks become wider and wider.

In Figure 18b the same analysis has been performed, but after reducing the maximum coefficient of shrinkage to 50% of its reference value ($a = a_0/2$). In this case, the risk of cracking is strongly reduced. If the Young´s modulus is lower than 25 GPa, the previously formed fictitious cracks tend to close gradually as the drying process advances.

If a is further reduced to 25% of its reference value ($a = a_0/4$), the simulations carried out showed that the cracking is insiginifiant (see Figure 17) even for high Young´s moduls (E=35GPa).

In these last analyses, fracture energy G_f and the coefficient of shrinkage $\alpha(h)$ have been varied simultaneously. Figure 19a shows the two stress-crack-opening bilinear diagrams adopted in these analyses. For both softening diagrams, two values of the shrinkage coefficient $\alpha(h)$ are used. Figure 19b shows the simulated crack evolution as function of drying time. For $\alpha = \alpha_0$, an increase of the fracture energy G_{f1} to 350 N/m retards the apparition of the cracking, but the severity of the damage (evolution of the crack opening) remains roughly the same for more advanced drying times. In case of a reduced shrinkage coefficient, the situation is different. For both fracture energies, the cracking severity is reduced as compared to previous cases. But if in case of a reduced $\alpha(h) = \alpha_0(h)/2$, the fracture enegy is increased to G_{f1}=350 N/m the risk for a real crack becomes practically zero.

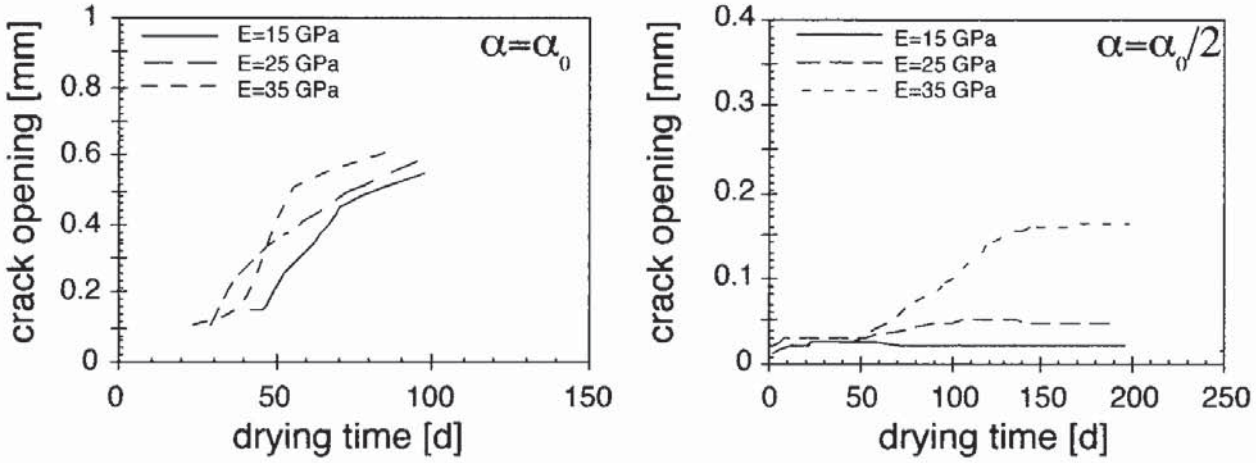

Fig. 18: Crack opening as function of drying time for three different Young modulii a) $a = a_0$, b) $a = 0.5\ a_0$

During drying and autogeneous shrinkage, which are displacement controlled phenomena, the tensile strength plays a minor role only with respect to crack formation. In fact this tendency was also confirmed by the sensitivity analysis performed later on. A relation between tensile strength and crack developement was not found.

With the combination of several numerical simulations it is possible to define a diagramm that shows the risk of crack formation as function of fracture energy, Young´s Modulus and the mean coefficient of shrinkage . This mean value is defined as follows:

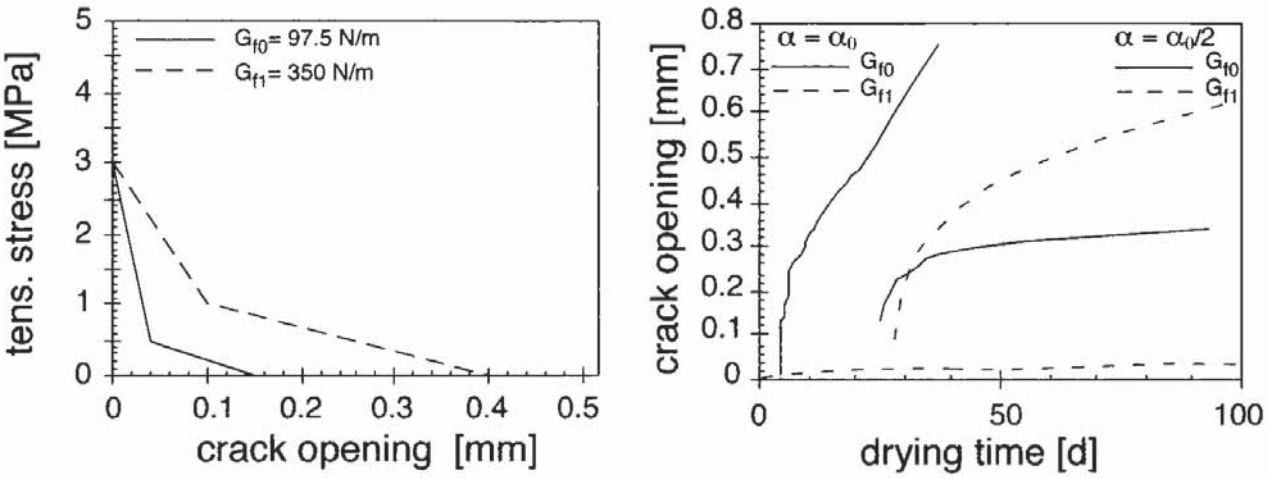

Fig. 19: a) Two softening diagrams with different strain softening and fracture energie
b) Crack opening as function of drying time for 4 different variations of the couple of parameters a(h), G_f

$$\overline{\alpha} = \frac{1}{h_2 - h_1} \cdot \int_{h_1}^{h_2} \alpha(h) \cdot dh \tag{11}$$

with $h_1 = 0.5$ (50% R.H.)
$h_2 = 1.0$ (100% R.H.)

A 3-dimensional representation of this diagramm is shown in Figure 20.

In many standards codes the shrinkage is defined by the strain measured on a specimen during drying from 100% to 50% R.H., its corresponding value according to the presented theorie can be approximated by the following expression:

$$\varepsilon_{meas}(100\% - 50\%) \cong \varepsilon_{t\to 0}^{t\to\infty(100\%-50\%)} = \overline{\alpha} \cdot (h_2 - h_1) \tag{12}$$

with $\varepsilon_{t\to 0}^{t\to\infty(100\%-50\%)}$ final shrinkage shrinkage strain measured when the test specimen is in hygral equilibrium with 50% R.H.

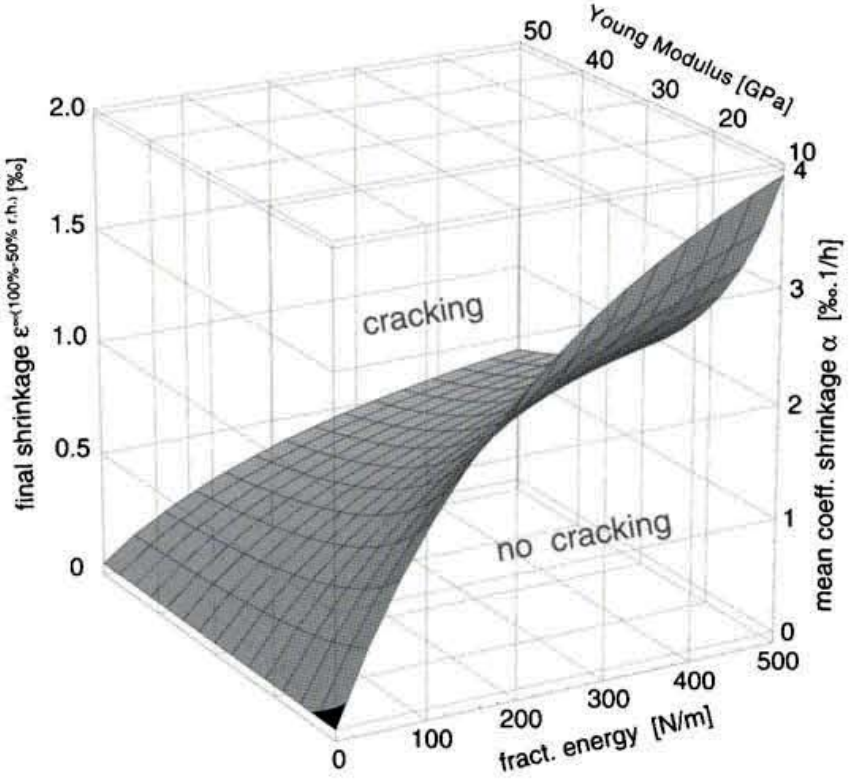

Fig. 20: Risk of crack formation as function of fracture energy, coeff. of shrinkage and Young Modulus

The shrinkage strain is also indicated on the z-axis in Figure 20. Figure 21 shows a 2-dimensional contour plot of the plane fracture energy - shrinkage from Figure 20. In order to guarantee a safte factor for the interpretation and the utilization of the diagram which covers the variation of the results, a transitional area between the cracking and the crack free zone is defined. Using this 2-dim. representation a minimization of the risk of shrinkage cracking of a particular cement-based material is achieved. For instance a mortar with a Young-Modulus of E=25 GPa, a fracture energy Gf=200 N/m and a final shrinkage strain of 0.8 ‰ (see point A1 in Figure 21) will crack during the drying period, in the case of restrained mechanical boundary conditions. In order to avoid crack formation the properties of this mortar have to be changed. Point A1 has to be moved from the critical zone (cracking) to the safe zone (no cracking). In fact there are 3 different possibilities: a) either to reduce the shrinkage strain to 0.6 ‰ (see point A2 in Figure 21) or b) to increase the fracture energy to 300 N/m (see point A3 in Figure 21) or c) to reduce the the Young´s-Modulus to 15 GPa. In practice it is possible to achieve these 3 modifications a) by reducing the cement content b) by addition of fibres c) by using air entraining agents or low Young-Modulus aggregates. All combinations of these parameters, that will lead to a shift of point A1 into the safe zone, are possible of course.

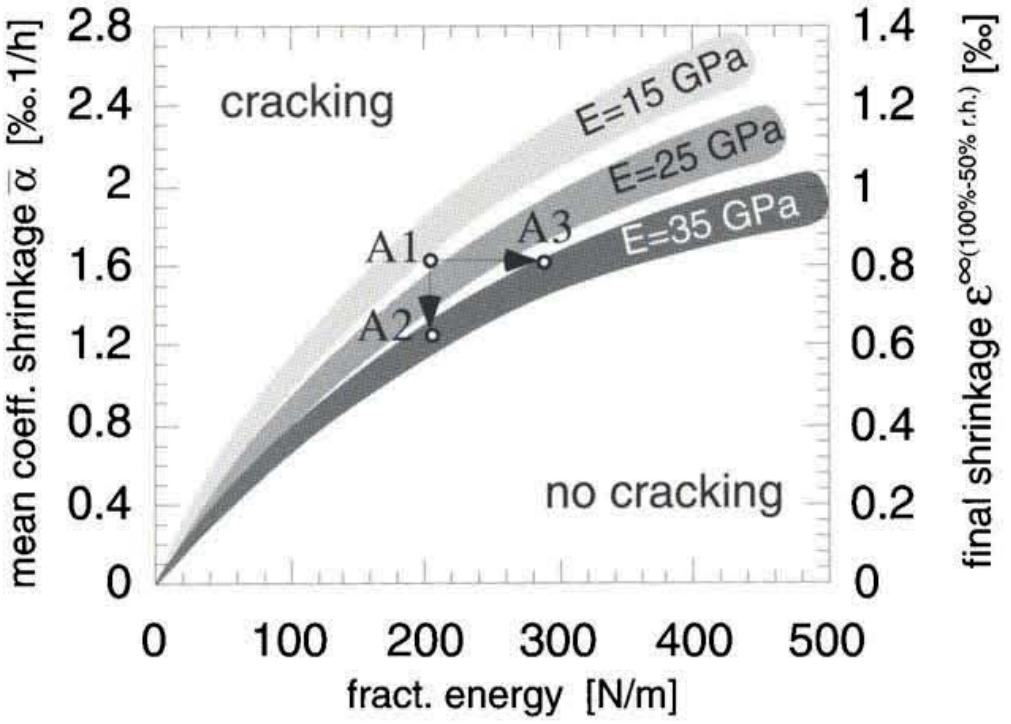

Fig. 21: Risk of crack formation as function of fracture energy, coeff. of shrinkage and Young Modulus

7 Conclusions

- A numerical model based on realtistic materials laws has been developed. This model allows us to study crack evolution in concrete structures subjected to hygral gradients. Time and moisture dependent materials laws can be taken into consideration.
- This numerical model was validated by results from the ring test carried out with two qualities of mortars having totally different hygro-mechanical materials laws.The model can capture the main features observed experimentally, especially the drying time at which the macrocracks will occur.
- By applying this numerical model, an intensive parametric study has been carried out. The relevant results are reported in this contribution.

  In general all parameters have a significant influence on the cracking due to shrinkage.
- A low moisture diffusivity retards the crack formation and slows down the crack opening but it can not avoid cracking.
- Among all materials parameters, the coefficient of shrinkage is the most sensitive parameter with respect to the crack formation and crack extension. A high coefficient of shrinkage will always lead to severe damage.
- The ring test is a powerful technique to study the tendency of cement-based material with respect to hygral cracking.
- The described method, i.e. a combination of experimental and numerical studies is a powerful tool for optimizing cement-based materials in particular to avoid shrinkage cracking.

8 References

1 Alvaredo, A.M.: *Drying Shrinkage and Crack Formation*, Building Materials Reports No.5, Aedificatio Publishers (1994).

2 Shah, S.P., Karaguler, M.E. and Sarigaphuti, M.: *Effects of Shrinkage-Reducing Admixtures on restrained Shrinkage Cracking of Concrete*, ACI Materials Journal, **89**, 289-295 (1992).

3 Martinola, G., Sadouki, H. und Wittmann, *F.H.: Numerisches Modell zur Beschreibung der Eigenspannungen und der Rissbildung in Beschichtungssystemen*, in Proceedings of 4th Intern. Colloq. on Materials Science and Restoration, F.H. Wittmann, editor, Aedificatio Publishers, 393-407 (1996).

4 Carlson, R.W. and Reading, T.J.: *Model Study of Shrinkage Cracking in Concrete Walls",* ACI Structural Journal, **85**, No. 4, 395-404 (1988).

5 Grzybowski, M. and Shah, S.: *Shrinkage Cracking of Fiber Reinforced Concrete*, ACI Materials Journal, **87**, No. 2, 138-148 (1990).

6 Sarigaphuti, M., Shah, S.P., and Vinson, K.D.: *Shrinkage Cracking and Durability Characteristics of Cellulose Fiber Reinforced Concrete*, ACI Materials Journal, **90**, No. 4, 309-318 (1993).

7 Pihalajavaara, S.E.: *On the main features and methods of investigation of drying and related phenomena in concrete.* PhD Thesis, Univ. of Helsinki, Finland, (1965).

8 Bazant Z.P. and Najjar L.J.: *Drying of concrete as a nonlinear diffusion problem.* Cement and Concrete Research, **1**, 461-473 (1971).

9 Hillerborg A., Modéer M. and Petersson P.-E.: *Analysis of crack formation and crack growth in concrete by means of fracture mechanics and finite elements,* Cement and Concrete Research **6**, 773-782 (1976).

10 Bazant Z.P. and Oh B.H.: *Crack band theory for fracture of concrete*, Materials and Structures, **16**, 155-172 (1983).

11 DIANA, *Users Manual - Release 6.1*, Diana Analysis BV, Delft, The Netherlands (1996).

12 Sadouki H. and van Mier J.G.M.: *Simulation of Hygral Crack Growth in Concrete Repair Systems,* Materials and Structures, **30,** 518-526 (1997).

13 Rots J.G.: *Computational modelling of concrete fracture*, Ph.D. thesis, Delft University of Technology, The Netherlands (1988).

14 Wittmann X., Sadouki H., and Wittmann F.H.: *Numerical Evaluation of Drying Test Data*, Trans. 10th Intern. Conf. on Strucutural Mechanics in Reactor Technology, Vol. **Q**, p. 71-79 (1989)

15 Roelfstra P.E. and Wittmann F.H.: *Numerical Method to Link Strain Softening with Failure of Concrete*, Fracture Toughness and Fracture Energy of Concrete, F.H. Wittmann, editor, Elsevier, Amsterdam (1986).

16 Brühwiler E.: *Bruchmechanik von Staumauerbeton unter quasi-statischer und erdbebendynamischer Belastung*, Dissertation No. 739, École Polytechnique Fédéral de Lausanne, (1988).

Article n°6

Damage and Crack Formation in Wood under Mechanical Action

H. Sadouki
Z. Issifou
F.H. Wittmann
Institute for Building Materials
ETH Zürich
Switserland

Abstract

Wood and wooden structures can be damaged or destroyed by a series of different actions. The influence of micro organisms and insects has been studied in detail. In this contribution non-linerar fracture mechanics are applied to describe damage and crack formation as induced by mechanical action. The term mechanical action implies external load as well as eigenstresses. Wood is a strongly anisotropic material and therefore the fracture mechanics parameters have to be determined for each orientation. Prediction of damage and crack formation is possible by means of appropriate numerical models. In this contribution a simple example is given only. It is the aim to point out the potential of application of non-linear fracture mechanics to anisotropic material such as wood in general. More detailed studies are to be performed.

1. Introduction

Wood is generally known to be a very durable material. There are historical wooden structures which date back several hundreds of years and they are still in a remarkable condition. Nevertheless, if wood is exposed to humid conditions for instance it can be destroyed in a comparatively short period by the action of micro organisms. There are also a series of insects which may induce serious damage to wooden structural elements. Both of the just mentioned mechanisms have been studied in the past and we know more or less how to counteract these attacks.

In this contribution damage and crack formation due to mechanical action shall be studied. The ficticious crack model [1] allows us today to simulate damage and crack formation in materials under the influence of high load. Wood is in contrast to other building materials such as concrete very anisotropic. That means that the fracture mechanics parameters depend strongly on the orientation in a wooden element. In this contribution characteristic values for the fracture energy and strain softening as obtained on spruce (epicea) are presented. These values will be compared with a tropical wood i.e. iroko.

Mechanical damage can be induced by locally acting high stresses. The origin of these stresses can be an external load. In this contribution however emphasis is placed on the action of eigenstresses in drying wooden elements.

2. Basic elements for the prediction of damage and crack formation under drying conditions

2.1.Moisture diffusion and shrinkage

If we want to predict shrinkage and shrinkage induced eigenstresses the first step is to determine the moisture gradients during the drying process. This can be simulated numerically if the diffusion coefficient in the main directions is known. Drying experiments have been carried out. From the moisture loss as function of time the diffusion coeffient can then be determined by inverse analysis [2]. In Fig. 1 the radial and tangential diffusivity as observed at a temperature of 20°C is plotted for four different types of wood.

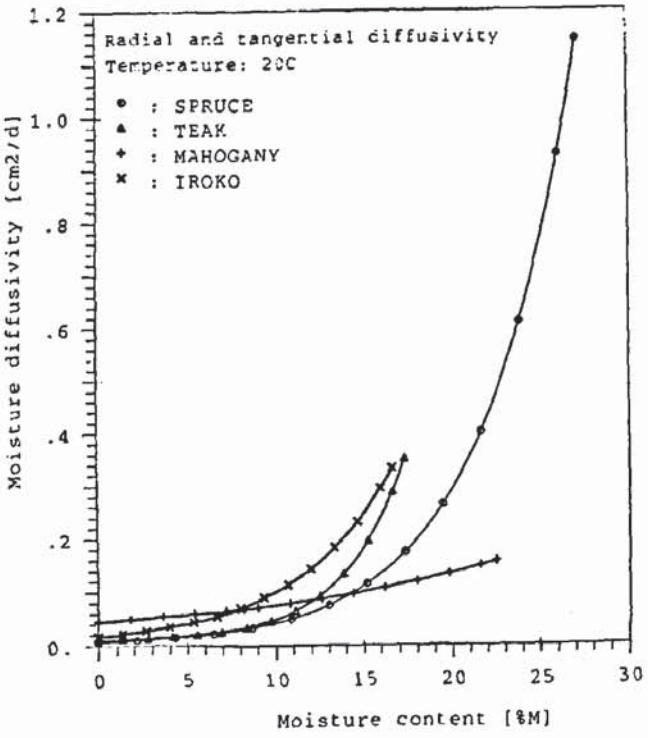

Fig. 1: Hygral diffusivity of four types of different wood as function of the moisture content

It is quite obvious that the diffusion coefficient decreases sharply with moisture content for all types of wood and that the diffusion coefficient of spruce in the humid region is much higher than the diffusion coefficient of the tropical wood.
Knowing the diffusion coefficient enables us to predict moisture profiles in drying samples of wood. In Fig. 2 the moisture profiles are plotted for 5,10,30,60 and 90 days. In this case it is assumed that the initially saturated wood dries out in an environment of 50% RH.

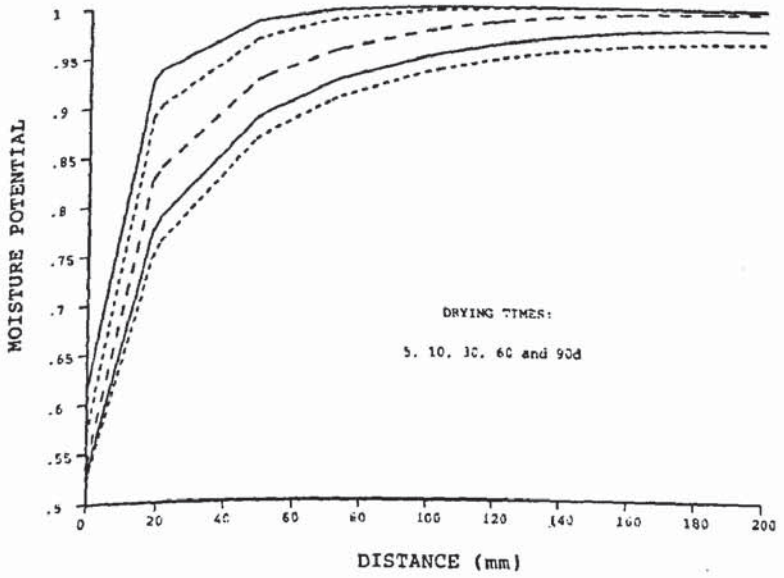

Fig. 2: Moisture profiles as numerically simulated for a drying wood sample after 5,10,30,60 and 90 days.

At any given moisture potential a characteristic moisture content is in equilibrium at constant temperature. This relation is called sorption isotherm. The sorption isotherm is not unique but it depends on the path a given moisture potential is reached. Typical desorption and adsorption isotherms are shown in Fig. 3 a and Fig. 3 b [3].

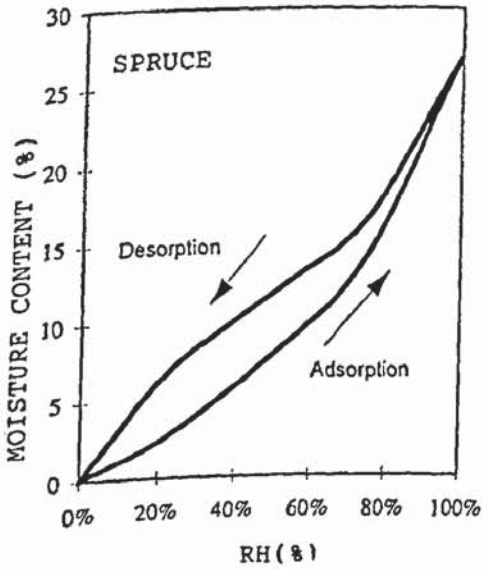

Fig. 3 a: Sorption isotherm for spruce.

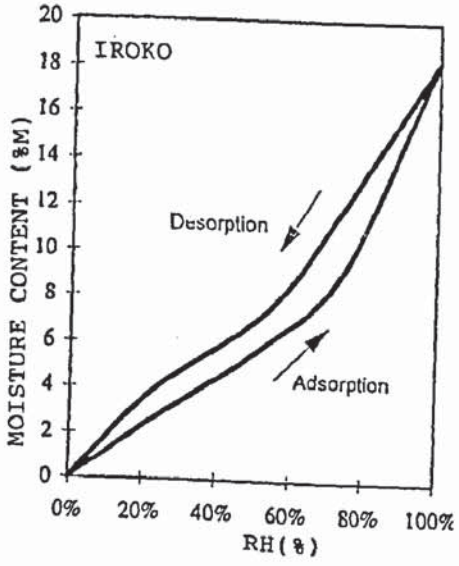

Fig. 3 b: Sorption isotherm for iroko.

Similar to the sorption isotherms exist length change isotherms. In the following we will only present measured equilibrium values for radial shrinkage as observed on four different types of wood if drying occurs from 100 to 0 % RH. Typical results are shown in Fig. 4 [3].

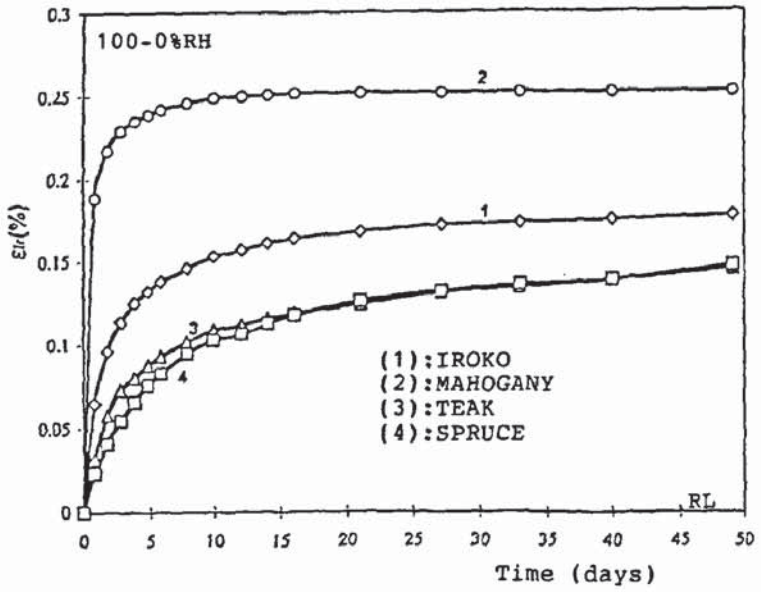

Fig. 4: Shrinkage of four different types of wood as measured on samples which dried from 100% RH down to 0% RH.

2.2.Crack formation under mechanical stress

In a simplified analysis crack formation is sometimes predicted by means of a strength criteria. The non-linear behaviour of wood under high tensile stresses leads to a failure behaviour which cannot be described by a simple strength criteria however. Linear elastic fracture mechanics has also been applied to wood and wooden structures. In case structural elements are very huge linear elastic fracture mechancis may be considered as reasonable approximation. For many standard dimensions however it is mandatory to apply non-linear fracture mechanics.

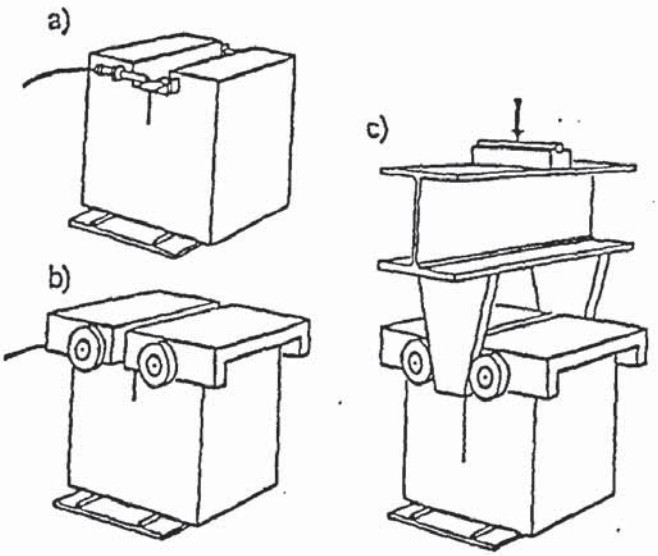

Fig. 5: (a) Geometry of a wooden sample as prepared for the wedge splitting test, (b) two metal plates with two ball bearings each are placed on the test specimen, (c) the wedge is pressed between the two opposite ball bearings.

There are a series of test methods to determine fracture mechanics parameters. The wet splitting test [4] has proved to be particularly suited for the determination of fracture energy and strain softening of wood. The principle of this test method is shown in Fig. 5. A cube or a prism with a central notch is mounted with two metal plates. Both having two ball bearings. A wedge is pressed by means of a well-controlled testing machine between two opposite ball bearings and thus forced the notch to grow. In this way a damage zone and finally crack formation is imposed to the wooden element under strain controlled conditions.

In this test set-up the wooden specimen can be placed in different orientations. In Fig. 6 two examples, i.e. RL and TL are shown.
A typical example again for spruce and iroko tested under the mode RL is shown in Fig. 7. The surface under the measured curve is equivalent to the fracture energy while strain softening is determined from the measured relation by inverse analysis [5]. The obtained strain softening diagram is shown in Fig. 8.

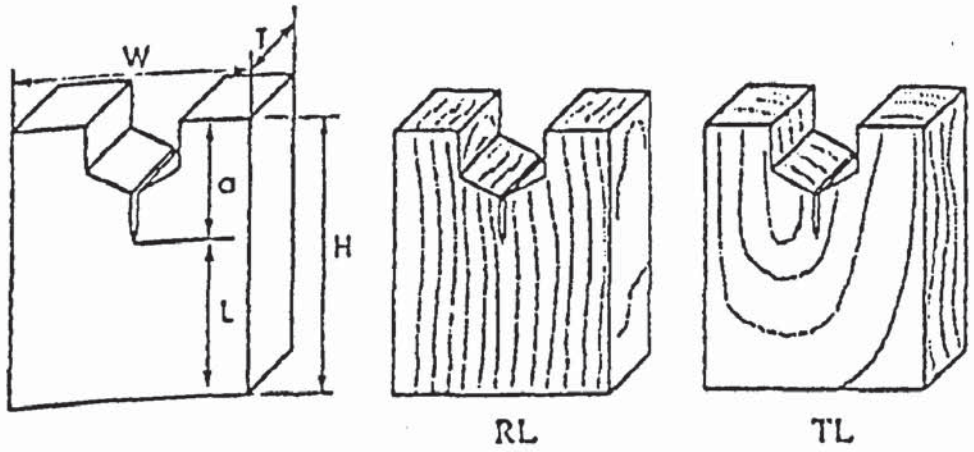

Fig. 6: Schematic representation of the orientation of wooden specimens in the wedge splitting test for mode RL and TL.

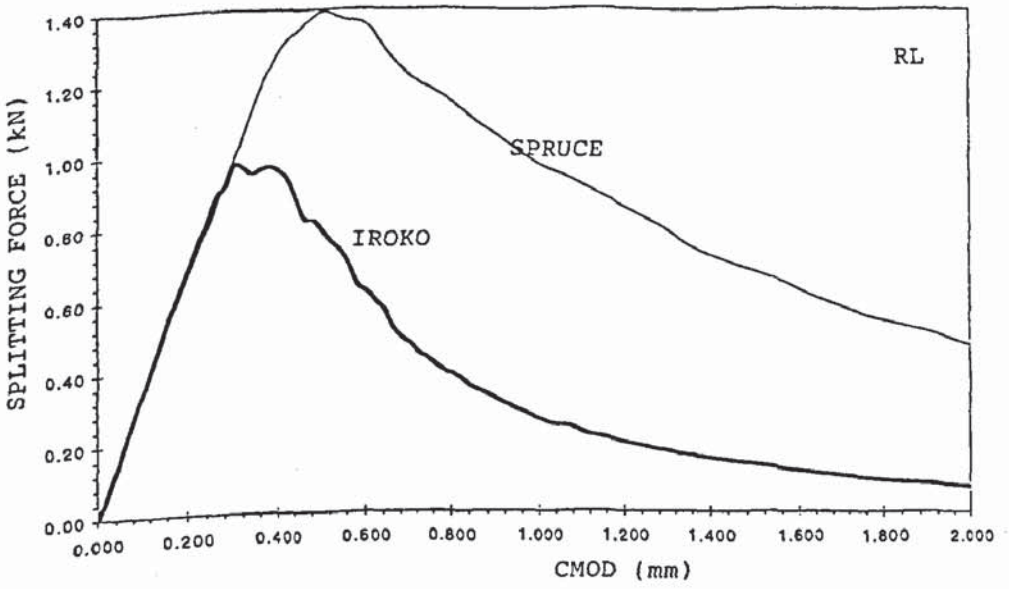

Fig. 7: Measured splitting force as function of the crack mouth opening displacements of the test specimen in the wedge splitting test.

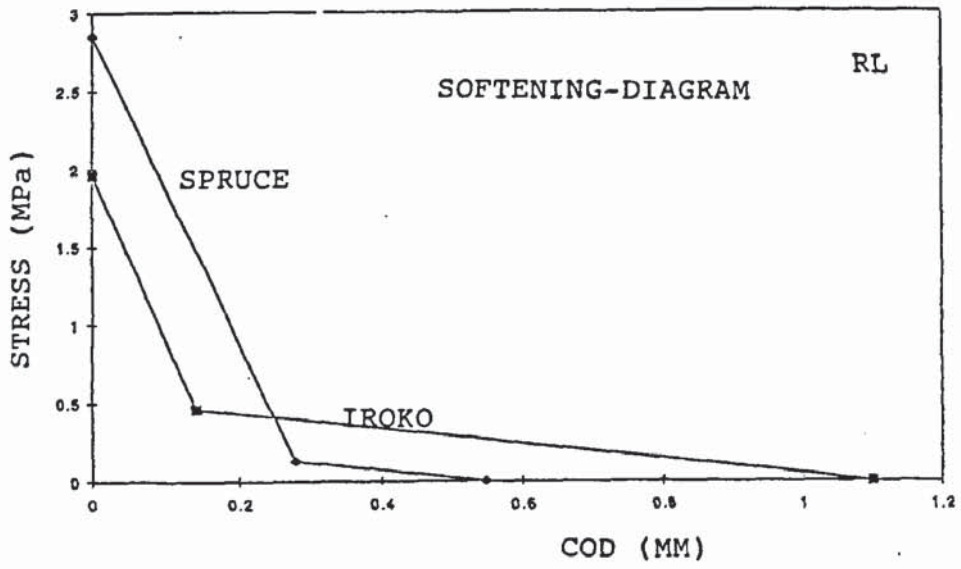

Fig. 8: Strain softening for spruce and iroko as obtained by inverse analysis from experimental data shown in Fig. 7.

3. An example: Simple numerical model for investigating drying of wood.

In the preceding sections we have presented all necessary data for a numerical simulation of damage and crack formation in wooden elements. The first step is to determine the moisture distribution. For this numerical calculation the diffusion coefficient as function of moisture content has to be determined. The next step is to attribute to each moisture potential along the moisture profile the corresponding shrinkage value. As shrinkage is restrained the result will be a three-dimensional state of eigenstresses. In a realistic analysis creep has to be taken into account, too. Here we want to demonstrate the principle of simulation of damage and crack formation and therefore, we have selected a simplified model. The F.E. code DIANA is used to perform the numerical simulation [6].

In Fig. 9 the structure of wood is simulated in a 2D representation. The finite element mesh consists of wide rows which represent the strong fibres in the composite material. They are seperated by narrow rows which are assumed to be much weaker. Therefore, crack formation in this orthotropic simplified model will only take place along the weak plains. A representation of this simple model is shown in Fig. 9. Properties of individual elements are randomly distributed around average values.

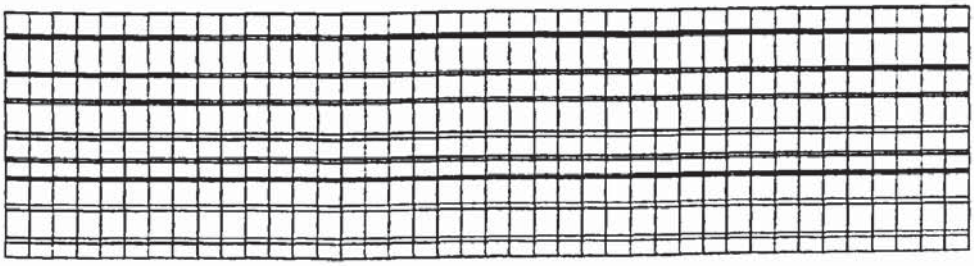

Fig. 9: Simplified representation of wood as an orthotropic material.

Now let us assume that the model material as shown in Fig. 9 is allowed to dry in the vertical direction through the upper surface only. In this case the upper layers have the tendancy to warp upwards and damage is originated in the outer vertical surface. In Fig. 10 the behaviour of the drying model element after 10 days and 90 days of drying is shown. It can be seen that after 10 days drying has introduced damage in two weak layers. The damage in this case is expressed by a local widening of the layer. These layers happen to be the weakest. After 90 days a real crack is observed at about half height of the drying element.

In a subsequent numerical experiment the same orthotropic model material has been studied, but in this case a notch (pre-crack) has been introduced before the drying process starts. It can be seen that the notch concentrates stresses and leads to delamination after 10 days already. After 90 days the delamination is even more pronounced and additional damage is induced in lower regions of the model element.

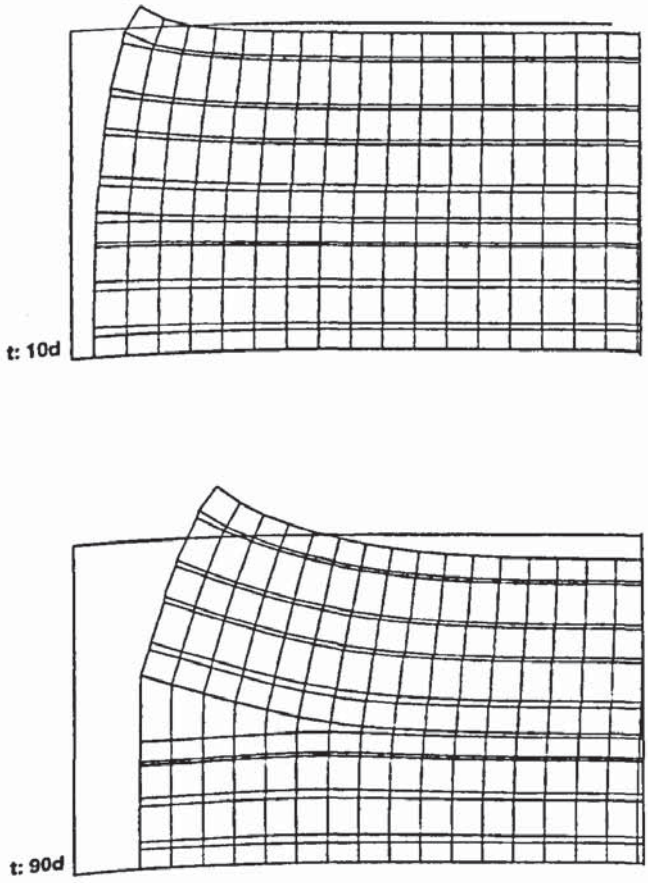

Fig. 10: Damage and crack formation of the model material shown in Fig. 9. Widening of the weak layers indicates the damaged zones.

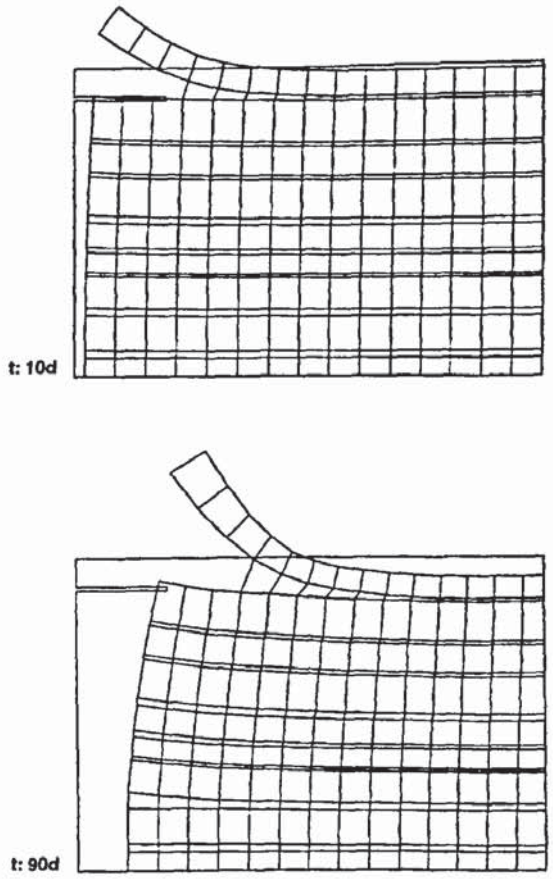

Fig. 11: Damage and crack formation of the model material shown in Fig. 9 but with an additional notch. After 10 days already delamination starts.

4. Conclusions

It has been shown that non-linear fracture mechanics is a powerful tool to simulate damage and crack formation of wood under mechanical load. If all material parameters have been determined adequately the drying process can be predicted in a realistic way. Crack formation under imposed eigenstresses can be simulated. This method can also be applied to find environmental conditions which will not lead to serious damage during the drying process.

5. References

1. A. Hillerborg, M. Modéer and P.E. Petersson, " Analysis of Crack Formation and Crack Growth in Concrete by Means of Fracture Mechanics and Finite Elements", Cement and Concrete Res., **6**, pp. 773-782, 1976.

2. X. Wittmann, H. Sadouki and F.H. Wittmann, "Numerical Evaluation of Drying Test Data", Trans. 10th Int. Conf. On Struct. Mechanics in Reactor Technology, Vol. Q, pp.71-79, 1989.

3. Issifou-Samarou, Z., "Etudes fondamentales des propriétés des essences de bois ouestafricaines en vue de leur utilisation dans le génie civil", Ph-D thesis, to appear.

4. Stanzl-Tschegg, S.E. and Tschegg, E.K., New Splitting Method for Wood Fracture Characterization, Wood Science and Technology, **29**, pp.31-50, 1995.

5. Roelfstra, P.E., and Wittmann, F.H., Numerical Method to Link Strain- softening with Failue of Concrete, in Fracture Toughness and Fracture Energy, ed. By Wittmann, Elsevier, Amsterdam, pp. 163-175, 1986.

6. DIANA, Users manual –Release 7.0, Diana Analysis BV, Delft, The Netherlands, (1998).

Article n°7

NUMERICAL MODEL FOR MINIMIZING RISK OF DAMAGE IN REPAIR SYSTEM

By Giovanni Martinola,[1] Hamid Sadouki,[2] and Folker H. Wittmann[3]

ABSTRACT: New cement-based repair overlays are subject to restraint and eigenstresses that can lead to crack formation and delamination. The origin of this complex state of stresses is found in the dimensional instability of the new coating. Drying shrinkage, autogeneous shrinkage, and temperature gradients are the most important loads acting on the system. In most cases the design of such coating systems is carried out in an empirical way. In this paper a new approach based on a numerical model is proposed to determine the relevant key parameters for the design of repair systems. By means of this model time-dependent moisture distributions and crack evolution in a drying concrete repair system can be simulated in a realistic way. Crack formation and delamination is described, with the smeared and discrete crack models, applying nonlinear fracture mechanics. The relevant material parameters influencing shrinkage cracking and delamination are identified by means of a sensitivity analysis. Finally, this approach is applied to analyze in a rational way the repair measures on a concrete bridge. This study primarily aimed to decide which repair material is more suitable with respect to shrinkage-induced damage and consequently which one provides the highest durability for the rehabilitated structure.

INTRODUCTION

One of the present challenges in civil engineering is the maintenance and the restoration of already existing reinforced concrete structures. In the last 50 years a large number of structures have been built; many of these are now deteriorated and have to be repaired.

In a traditional reinforced concrete element, concrete has to take over two totally different assignments (Wittmann 1998). First, concrete has to provide a structural element with the required strength and stiffness. At the same time, the concrete cover has to prevent corrosion of the steel reinforcement. Whether this second nonmechanical assignment is really fulfilled is rarely checked. As a consequence, many concrete structures have to be repaired after a relatively short service life, although the structural load-bearing capacity is hardly diminished. In many cases, carbonation depth reaches the reinforcement and the chloride content in the vicinity of the steel reinforcement reaches critical values too rapidly. Usually in these cases, the contaminated concrete cover is removed mechanically or by high-pressure water jetting. The reinforcement is freed from corrosion products, and finally the concrete surface is restored. To ensure a mechanical reliability and a long-term durability to the repaired concrete structure, the mechanical and nonmechanical assignments must be fulfilled.

Experience shows that the design of durable concrete repair measures can be more complex than the design of new structures because each damaged structure imposes its own set of necessities. New technology and methodology are in development to provide solutions for this delicate problem. Unfortunately, in most cases, an empirical approach is chosen instead of an engineering analysis and rigorous design. This way too often leads to early failure. Mistakes in design, selection of materials, and execution lead to crack formation, with a drastic reduction of the durability of the repaired structures. One basic problem is that engineers so far have no quantitative tools to evaluate if a proposed repair design is appropriate in a given situation. The use of durable repair materials does not ensure the durability of the system substrate (old concrete) and overlay (repair material), because the effectiveness of a repair measure is also related to the dimensional compatibility between overlay and substrate. If the two components of the system are not compatible, failure in the overlay or debonding at the interface will occur (Emmons et al. 1993). Overlay and substrate are subjected to different external or internal loads or both. If the resulting deformations of both components are different, restraining action will give rise to stresses in the composite system. Failure of the repair system will occur when the stresses due to restraint cannot be absorbed by the system. In this case, crack formation will appear. The capacity of the materials of the system to absorb restraining actions is contained in its elastic deformation, creep deformation, and strain softening. The complex competition between loads and the material is illustrated in Fig. 1.

The most important factor influencing the state of restraint of the system is the hygral load. Usual structural loads can provoke failure of the system only in combination with physical loads. For this reason structural load plays only a secondary role in the mechanism of failure of a repair system. The chemical load can be avoided by the correct choice of the mix

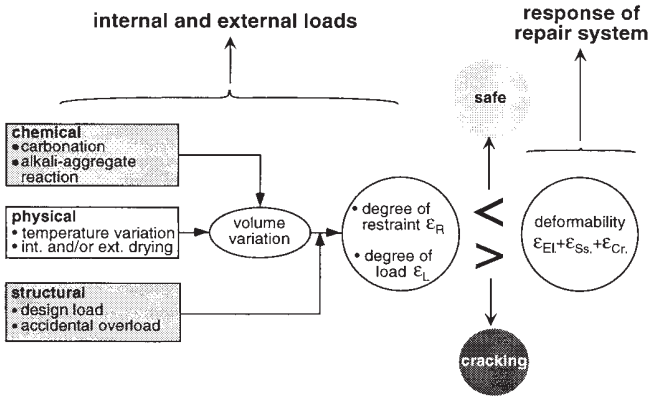

FIG. 1. Analysis of Principal Loads Acting in Repair System and Failure Criteria [ε_{El}, ε_{Ss}, and ε_{Cr} Are Elastic, Crack (Strain Softening), and Creep Strains, Respectively]

[1]Res. Engr., Lab. for Build. Mat., Swiss Fed. Inst. of Technol., Zürich, Switzerland, ETHZ CH-8093 Zürich. E-mail: martinola@ibwk.baug.ethz.ch

[2]Sr. Res. Engr., Lab. for Build. Mat., Swiss Fed. Inst. of Technol., Zürich, Switzerland, ETHZ CH-8093 Zürich.

[3]Prof. and Dir., Lab. for Build. Mat., Swiss Fed. Inst. of Technol., Zürich, Switzerland, ETHZ CH-8093 Zürich.

Note. Guest Editor: Thomas Triantafillou. Discussion open until September 1, 2001. To extend the closing date one month, a written request must be filed with the ASCE Manager of Journals. The manuscript for this paper was submitted for review and possible publication on June 18, 1999; revised February, 15, 2000. This paper is part of the ***Journal of Materials in Civil Engineering***, Vol. 13, No. 2, March/April, 2001. ©ASCE, ISSN 0899-1561/01/0002-0121–0129/$8.00 + $.50 per page. Paper No. 21206.

components of the overlay material and a detailed analysis of the environmental conditions.

In this paper the behavior of repair systems under internal and external drying conditions is investigated first. A numerical model that allows one to calculate time-dependent moisture distribution, crack formation, and crack propagation is proposed. The analysis of thermal loads can be treated in an analogous way. The numerical model is applied for a parametric study. Results of the sensitivity analysis are pointed out to show the relevant material parameters influencing shrinkage cracking. A new approach, which is able to provide solutions for the design of repair of concrete structures, is proposed. Finally the efficiency of the proposed approach is shown by describing a case study.

DAMAGE MECHANISMS IN RESTRAINED CEMENT-BASED MATERIALS INDUCED BY DRYING

If a moist mortar or concrete element is placed in an atmosphere with a low relative humidity (RH), the porous material starts immediately to lose moisture through its exposed surfaces. This drying process generates moisture gradients in the material along cross sections normal to the exposed surfaces. Fig. 2(a) shows a drying concrete element and its transversal (normal to the drying direction) moisture profiles at different drying times. Moisture loss leads to a volume change of the element. The differential drying will cause differential deformations in the material. If the drying element is regarded as a hypothetical superposition of infinitesimally unbounded thin layers, then each layer is free to deform independently from its neighboring layers. Under this condition of unrestrained shrinkage, no stresses can be generated. This hypothetical situation is schematically shown in Fig. 2(b) (Bazant 1988). In reality the layers in the element are monolithically interconnected. Because of the differential shrinkage along the vertical cross section of the element and to the restraint imposed by the bond between layers, internal stresses (eigenstresses) will be induced. Fig. 2(c) shows the state of the induced eigenstresses after a short time of drying. The highest tensile stresses occur in the exposed surface layer where the

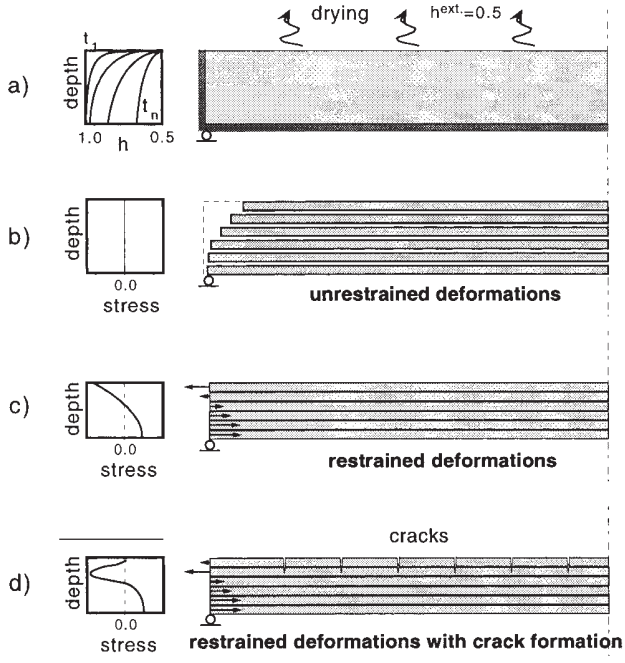

FIG. 2. Stress Distribution and Crack Formation in Drying Concrete Element

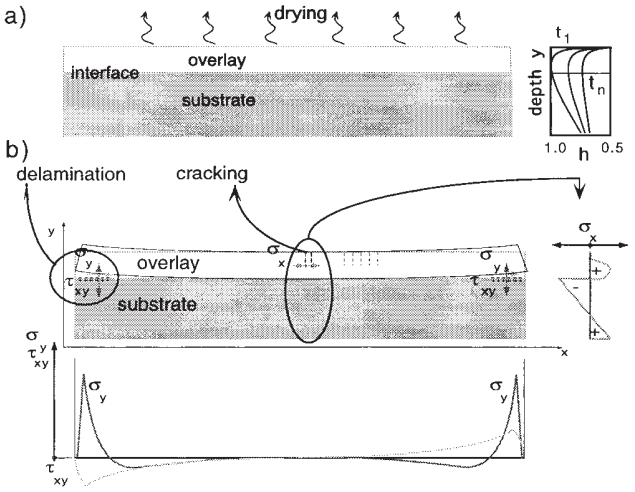

FIG. 3. (a) Schematic Representation of Drying Repair System and Moisture Distributions at Different Drying Times; (b) Hygral-Induced Cracking and Delamination and Stress Distributions

moisture gradients are the highest. As the drying process proceeds, the generated tensile stresses increase. Depending on the mechanical properties of the material and on the severity of the hygral gradients, the tensile stresses can easily overcome the tensile strength of the material. As a consequence, cracks will occur in the upper layers of the element. As the drying process continues, cracks will propagate further along the cross section of the element. Fig. 2(d) shows schematically some cracks formed in the upper layers and the corresponding stress distribution after a longer drying time, as compared with the case shown in Fig. 2(c). As can be seen in Fig. 2(d), the highest tensile stress (peak of the stress-depth curve) is gradually shifted to the inner part of the concrete element, leading to a further propagation of the existing cracks. Simultaneously, the cracked upper layers unload progressively.

In the case of a composite cement-based material, such as a concrete repair system, besides the shrinkage-induced cracks, another type of damage can take place. A typical concrete repair system consisting of a superposition of an old concrete element and a new concrete or mortar repair layer is shown in Fig. 3. Initially, the new material layer is in a quasi-moisture saturated state. Generally the upper surface of the composite system is in contact with the environment. If the surrounding relative humidity is low enough, compared with the pore humidity of the material of the new layer, the system begins immediately to dry out. As has been mentioned above, cracks can occur in the upper layer because of the hygral gradients generated during the drying process. Simultaneously, the entire new layer is subjected to a ''global'' volume change. Depending on the composition of the cement-based material used for the repair layer, the volume variation can be much larger if the material is subjected to endogeneous drying. This volume variation is generally restrained by the old concrete element. It must be emphasized that the degree of restraint depends not only on the compatibility of the hygromechanical parameters of both materials but also on the actual moisture gradient between the two materials and on the thickness of the new layer. As a consequence of the restraint, normal tensile stresses σ_y and bond shear stresses τ_{xy} will be induced in the interfacial zone. Fig. 3(b) shows schematically the state of the stresses and the possible damages, cracking of the overlay, and decohesion of the interface. If the stresses are higher than the bond cohesion, then delamination will occur.

J. Mater. Civ. Eng., 2001, 13(2): 121-129

NUMERICAL MODEL AND ITS EXPERIMENTAL VALIDATION

Basic Concept of Model

Shrinkage damage induced by moisture variations in a drying cement-based material element is a rather complex problem. This is mainly due to the highly heterogeneous nature of the structure of the material. Material properties and laws are often coupled in various ways, and they depend on many factors such as the age of the material, duration of loading, and actual state variables such as strains, stresses, temperature, and moisture content. An ideal model taking into account all possible phenomena, their mutual interaction, and their influence on the material parameters seems to be utopistic and is beyond the scope of this paper. The proposed numerical model dealing with crack formation and crack propagation in a concrete element subjected to drying will be briefly presented (Martinola et al. 1996; Martinola and Sadouki 1998). The relevant material properties and laws and their fundamental mutual interactions only will be considered; for instance, the influence of temperature will not be taken into consideration.

The drying process is a phenomenon to which most concrete structures are subjected during their life spans. The different drying mechanisms force the water initially held in pores of the material to migrate toward the surfaces exposed to a dry atmosphere. To analyze the mechanical behavior of a structural element under moisture changes, the moisture distributions in space and time must be determined first. Nowadays it is well recognized that the transient moisture transfer in porous materials can be described by the nonlinear diffusion equation in a realistic way. The drying process is then given by the following partial differential equation:

$$\frac{\partial w}{\partial t} = \mathrm{div}(D(w)\cdot\nabla w) + q_w(t) \tag{1}$$

in which w = actual moisture content; $D(w)$ = moisture-dependent diffusion coefficient; $q_w(t)$ = rate of the moisture loss due to the endogenous drying. Combined with appropriate boundary and initial conditions, (1) can be solved numerically to obtain the moisture profiles at any drying time. Note that, in (1), moisture content w is used as driving potential. The humidity values h can, in principle, be calculated from the corresponding moisture content values w by means of the desorption isotherm, $w = w(h)$.

The mechanical behavior of the system under hygral loading can be described at any time by the total strain $\varepsilon(t)$, which may be subdivided as follows (*DIANA* 1996):

$$\varepsilon(t) = \varepsilon_{El}(t) + \varepsilon_{Sh}(t) + \varepsilon_{Cr}(t) + \varepsilon_{Ss}(t) \tag{2}$$

in (2) ε_{El} = instantaneous elastic strain; ε_{Sh} = shrinkage (or swelling) strain induced by a hygral variation; ε_{Cr} = creep strain (stress-dependent); and ε_{Ss} = strain that can be attributed to strain softening. The elastic strain ε_{El} is related to the locally acting stress by means of the elastic properties of the material. This relation may be linear or nonlinear. The shrinkage strain ε_{Sh} induced by a moisture variation δw is given by the following expression:

$$\varepsilon_{Sh}(t) = \alpha_{Sh}(w)\cdot\delta w \tag{3}$$

in which α_{Sh} = hygral coefficient of shrinkage (or swelling), which depends on the material composition and on the actual moisture content (or on the actual pore humidity). The creep strain ε_{Cr} is described by the viscoelastic theory. By assuming the principle of superposition, ε_{Cr} can be expressed by the classical Volterra integral equation

$$\varepsilon_{Cr}(t) = \int_0^t J(t,\tau)\cdot\bar{C}\cdot\dot{\sigma}(\tau)\cdot d\tau \tag{4}$$

in which t = time; τ = duration of load; $J(t, \tau)$ = creep function; C = compliance; and $\dot{\sigma}(\tau)$ = stress rate. In this analysis, the creep function is approximated as a sum of exponential functions (Dirichlet series) (*DIANA* 1996).

In this approach, the cohesive crack model (Hillerborg et al. 1976; Bazant and Oh 1983) is used for simulating crack formation and crack propagation. The crack strain is then given by the stress-strain softening diagram of the material. Fig. 4 shows schematically the incorporated fracture mechanics concepts. The multiple-crack model as proposed by Rots (1988) is used. The FEM-Code DIANA has been used as a basis in this modeling (*DIANA* 1996).

Material parameters and laws needed in this model are determined by means of various adequate experiments. Some of them, such as moisture diffusivity (Wittmann et al. 1989) or stress-strain softening diagram (Roelfstra and Wittmann 1986) are determined indirectly from experimental data by means of appropriate inverse analyses. A detailed description of this numerical approach and the experimental determination of the material laws can be found in Martinola and Sadouki (1998).

Validation of Model

The model described briefly above has been already validated by means of two different experiments, namely, a ring-test specimen (Martinola et al. 1998) and a concrete repair system (Martinola et al. 1997). The first experiment is the so-called instrumented ring-test generally used to assess the risk of shrinkage cracking of cement-based materials (Shah et al. 1992). The test specimen consists of casting a mortar (or concrete) ring around a stiff steel ring. Fig. 5 shows a 2D repre-

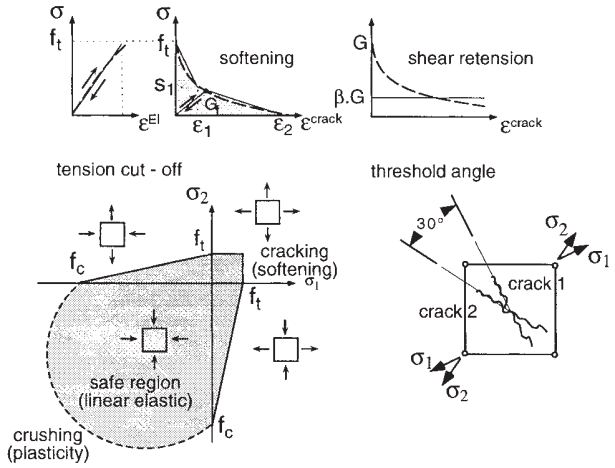

FIG. 4. Characteristics of Fracture Mechanics Model

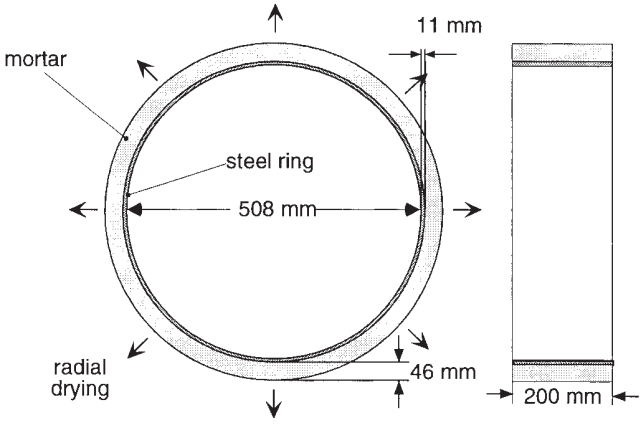

FIG. 5. Ring-Test Setup

J. Mater. Civ. Eng., 2001, 13(2): 121-129

sentation of the ring-test setup. After a preliminary wet curing period, the outer form of the ring is removed and the concrete ring is exposed to radial drying. Because of the generated hygral gradients during the drying process and the high degree of restraint by the steel ring, cracking of the concrete ring will generally occur. By means of an appropriate experimental setup, crack formation and crack growth can be followed as a function of drying time. Two mortars with totally different hygral and mechanical properties have been used to validate the numerical model, namely, a normal mortar and a high-performance mortar (fiber-reinforced mortar). The essential material parameters of both materials have been determined experimentally and then used in the numerical model. By comparing the experimental results obtained by the ring test with the numerically predicted results, it can be concluded that the numerical approach can capture, at least qualitatively, the main features of the shrinkage cracking observed experimentally. The experimental and numerical results are given in detail in Martinola et al. (1998).

The second experiment used to validate the numerical model is a concrete repair system, as shown in Fig. 3(a). A 4-cm-thick layer of fresh mortar has been cast on top of an old concrete beam with a length of 150 cm. After a curing period, the composite system was exposed to a drying atmosphere of 45% RH. Measurement devices have been used, allowing the recording of vertical displacements of the exposed surface of the overlay as a function of the drying time. As usual, the hygral and mechanical parameters of the repair mortar and of the concrete substrate have been experimentally determined. The proposed numerical model was then used to simulate the hygromechanical behavior of this composite system. A good agreement has been found between the numerical and the observed results (Martinola 1997). As an example, a comparison of the measured with the calculated vertical displacement profiles along the exposed surface at three selected drying times is given in Fig. 6.

APPLICATION OF MODEL FOR OPTIMIZING REPAIR SYSTEMS

Repair Material—Criteria for Minimizing Risk of Shrinkage Cracking

Based on the reasonable agreement between the observed results obtained from different experiments performed on different materials and the numerical results, the proposed model has been used to carry out a parametric study. The chosen ''numerical specimen'' is a mortar-steel ring (Fig. 5) subject to radial drying. The objective of this study is to identify the most relevant material parameters influencing shrinkage cracking and consequently to be able to decide which material parameter(s) must be optimized to try to reduce the risk of damage as far as possible.

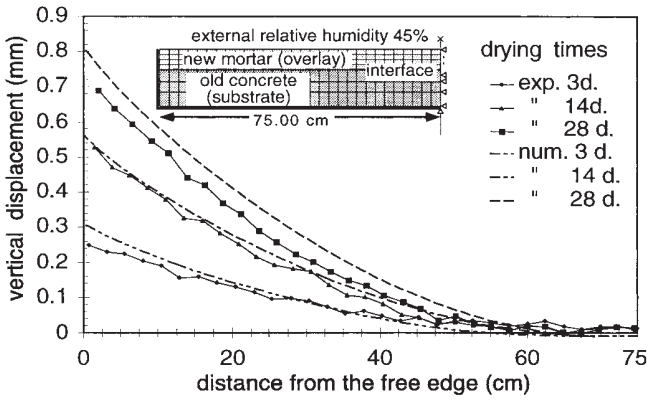

FIG. 6. Experimental and Calculated Profiles of Vertical Displacement along Exposed Surface

The analysis showed that the shrinkage coefficient, the fracture energy, and the Young's modulus are the most important parameters influencing cracking. Note that the tensile strength plays a minor role only in the damage process.

By compiling the obtained numerical results, a diagram that shows the risk of crack formation as a function of the above-mentioned material parameters can be plotted as shown in Fig. 7. In this figure, the z-axis represents the mean value of the coefficient of shrinkage $\bar{\alpha}$, defined as follows:

$$\bar{\alpha} = \frac{1}{h_2 - h_1} \cdot \int_{h_1}^{h_2} \alpha(h) \cdot dh \tag{5}$$

with $h_1 = 0.5$ (50% RH); and $h_2 = 1.0$ (100% RH)

In many standard codes, the shrinkage is defined by the strain measured on a specimen during drying from 100 to 50% RH, and its equivalent value according to the presented theory can be approximated by the following expression:

$$\varepsilon_{meas}(100\% - 50\%) \cong \varepsilon(t \to \infty) = \bar{\alpha} \cdot (h_2 - h_1) \tag{6}$$

with $\varepsilon(t \to \infty)$ being the final shrinkage strain measured when the test specimen, initially at 100% RH, reaches a hygral equilibrium with 50% RH.

Fig. 8 shows a 2D contour plot of the plane fracture energy

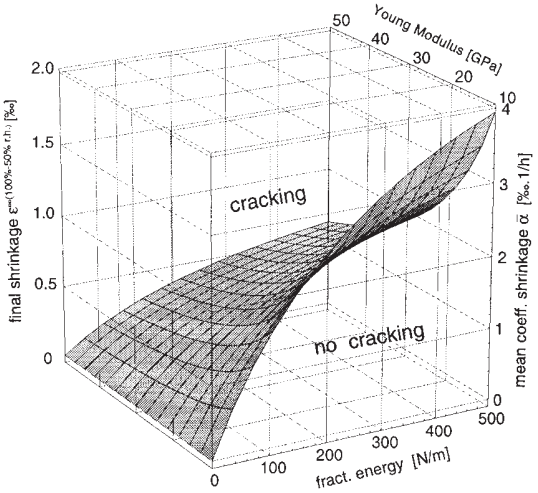

FIG. 7. Surface Separating Conditions for Cracking and No Cracking of Repair Layer as Function of Fracture Energy, Coefficient of Shrinkage, and Young's Modulus

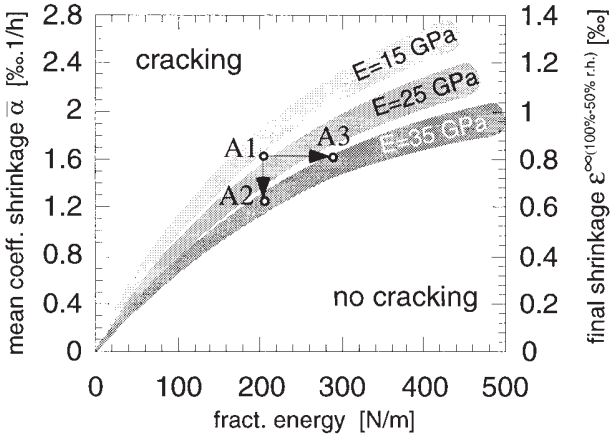

FIG. 8. Two-Dimensional Representation of Risk of Crack Formation as Function of Fracture Energy, Coefficient of Shrinkage, and Young's Modulus

J. Mater. Civ. Eng., 2001, 13(2): 121-129

versus shrinkage obtained from Fig. 7. To introduce a safety factor for the interpretation and the utilization of the diagram that covers the variation of the results, a transitional area between the cracking and the crack-free zone is defined.

Using this 2D representation, a minimization of the risk of shrinkage cracking of a particular cement-based material can be achieved. For instance a mortar with a Young's modulus of $E = 25$ GPa, fracture energy $G_f = 200$ N/m, and final shrinkage strain of 0.8% (Fig. 8, point A1) will crack during the drying period, in the case of restrained mechanical boundary conditions. To avoid crack formation, the properties of this mortar have to be changed. Point A1 has to be moved from the critical zone (cracking) to the safe zone (no cracking). In fact there are at least three different possibilities to reach this goal: (1) the shrinkage strain is reduced to 0.6% (Fig. 8, point A2); (2) the fracture energy is increased to 300 N/m (Fig. 8, point A3); or the Young's modulus is reduced to 15 GPa. In practice it is possible to achieve these three modifications by (1) reducing the cement content or application of a shrinkage reducing agent or both; (2) addition of fibers; or (3) using air entraining agents or low Young's modulus aggregates. All combinations of these parameters that will lead to a shift of point A1 into the safe zone are possible, of course.

Interface between Overlay and Substrate

Parametric Study and Relevant Results

By means of the numerical model, different repair systems, such as the one shown in Fig. 3, have been analyzed. The main objective of this study was to determine the relevant material parameters influencing debonding between the substrate and the repair layer.

It has been found that, if the material parameters of the repair material are optimized with respect to the crack formation in the overlay, the risk of the debonding at the interface is also reduced. This can be explained as follows: a low degree of cracking in the overlay means that the induced stresses in the layer are not so high as to affect the interfacial zone. Nevertheless, this assertion is not any more valid if the bond strength (cohesion) is too low. The performed analyses show that, for given hygromechanical properties of the overlay and of the substrate, the decohesion process is governed only by the mechanical parameters of the interface, namely, the cohesion strength and the fracture energy (Sadouki and van Mier 1997). The resulting conclusion that can be drawn from the analyses can be formulated as follows: the higher the cohesion strength and the fracture energy of the interface, the lower is the likelihood of an interfacial decohesion. Typical results of the analysis are given in Fig. 9 (Martinola and Sadouki 1998). This figure shows the deformed shapes of a repair system at three chosen drying times. As it can be seen in Fig. 9(a), if the bond strength and the fracture energy of the interface are relatively low, 1 MPa and 25 N/m, respectively, then serious debonding occurs along the interface. The delamination is particularly severe at the end faces of the repair system. The analysis was repeated with the same hygromechanical parameters and the same thickness of the overlay, but the bond strength and the fracture energy of the interface were increased to 3 MPa and 95 N/m, respectively. The obtained results are shown in Fig. 9(b), representing the deformed shapes of the repair system at the same drying times as those given in Fig. 9(a). As can be seen, in this case no debonding takes place at the interface, even after a long drying period. These numerical results are confirmed experimentally in a recent research project (Martinola and Sadouki 1998). High mechanical performance of the interface of a concrete repair system can be reached in several ways (Trausch and Wittmann 1996) (for instance, by enhancing the roughness of the old concrete surface).

It must also be emphasized that delamination is not only influenced by the properties of the overlay and of the interfacial zone but also by the properties of the underlying old concrete.

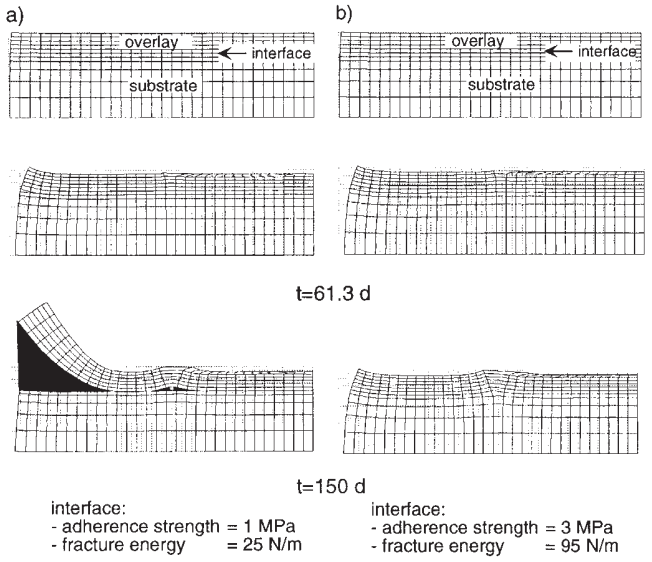

FIG. 9. Evolution of Total Deformation in *x*- and *y*-Directions: (a) Interface with 1-MPa Adhesion Strength and 25-N/m Fracture Energy; (b) Interface with 3-MPa Adhesion Strength and 95-N/m Fracture Energy

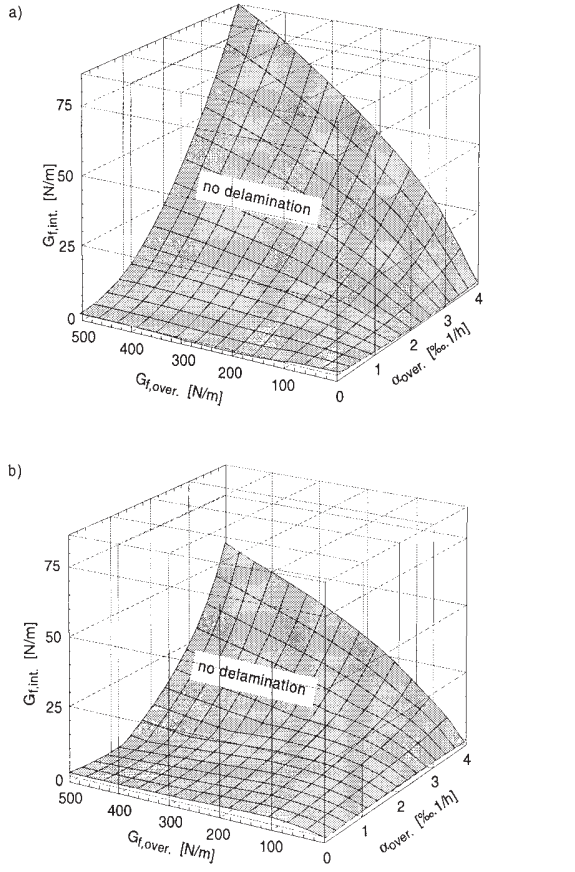

FIG. 10. Risk of Delamination of Overlay as Function of Fracture Energy $G_{f,int}$ of Interface and of Coefficient of Shrinkage α_{over} and Fracture Energy of Overlay $G_{f,over}$: (a) Young's Modulus of Overlay, 30 GPa; (b) Young's Modulus of Overlay, 15 GPa

J. Mater. Civ. Eng., 2001, 13(2): 121-129

Criteria for Minimizing Risk of Delamination

The above parametric study shows clearly that decohesion of the interface is an extremely complex problem. This complexity is because the delamination process depends not only on the mechanical parameters of the interface itself but also on the hygromechanical properties of both materials composing the repair system, namely, the repair and the substrate materials.

Based on the performed parametric analysis, which aimed to identify the most important effects on the delamination process of relevant materials, some criteria for minimizing the probability of delamination can be derived. As an example, one can define a delamination criterion based on the required minimum fracture energy of the interface as a function of the fracture energy and of the coefficient of shrinkage of the overlay material. Fig. 10 shows schematically a 3D representation of the transitional area between the delamination and delamination-free zones for two different Young's moduli of the repair material. The region above the critical surface represents the safe region.

PROPOSED APPROACH FOR DESIGN OF DURABLE REHABILITATION

Based on the combined experimental and numerical method described above, the proposed step-by-step rational approach for a durable concrete repair system is given by the flowchart shown in Fig. 11.

CASE STUDY

Description of Problem

The columns of a 25-year-old concrete bridge, as shown in Fig. 12, have to be repaired. Because of intense traffic and a chemically aggressive surrounding atmosphere, the outer layers of the columns are carbonated and totally contaminated by chlorides and other aggressive ions. The steel reinforcement is no longer protected against corrosion; the load-bearing capacity of the structure is jeopardized. It has been decided to restore the initial state of the structure by removing a 5-cm-thick concrete cover from the damaged columns and then to apply a new mortar (or concrete) as a repair layer.

In a preliminary analysis, the design engineer proposed three variants:

- Variant A: Polyvinyl acetate fiber reinforced mortar with a maximum aggregate size of 3 mm and a water-to-cement ratio of 0.38. The thickness of the layer should be 60 mm. The mortar is to be applied by shotcreting.
- Variant B: Concrete with a maximum aggregate size of 8 mm and a water-to-cement ratio of 0.36. The thickness of the layer should be 70 mm. The concrete is to be cast on the substrate with sliding formwork.
- Variant C: The repair concrete is identical to the one in the case of variant B, but stainless steel reinforcing bars with a cross section of 0.4 mm^2/m are embedded in the repair layer at a distance of 20 mm from the outer surface.

A sketch of the three variants is given in Fig. 13.

Application of Proposed Approach and Results

To decide which of the different variants is most suitable with respect to crack formation under hygral variation, the approach described above is used to analyze and then to compare the cracking of the three variants.

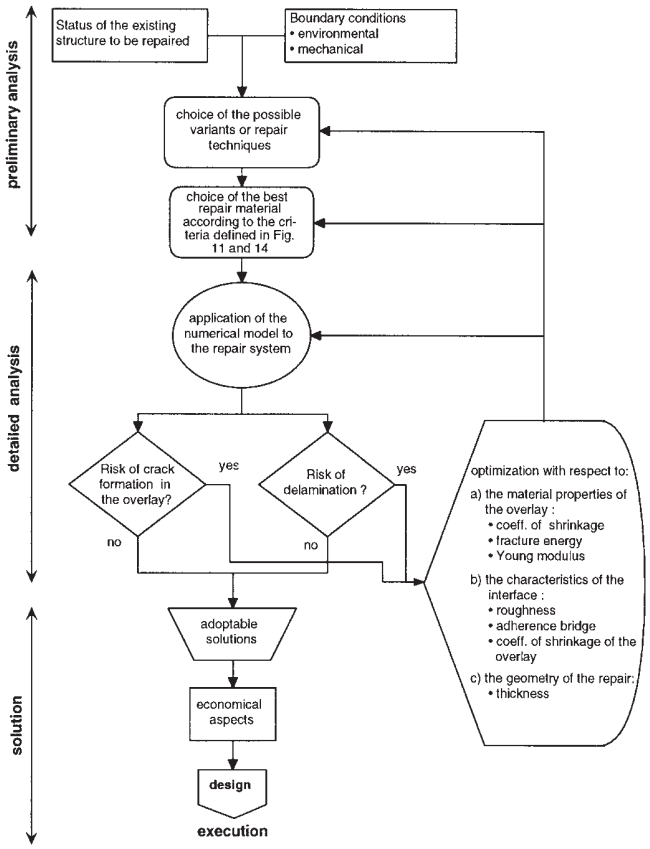

FIG. 11. Schematical Illustration of Proposed Approach for Durable Repair System

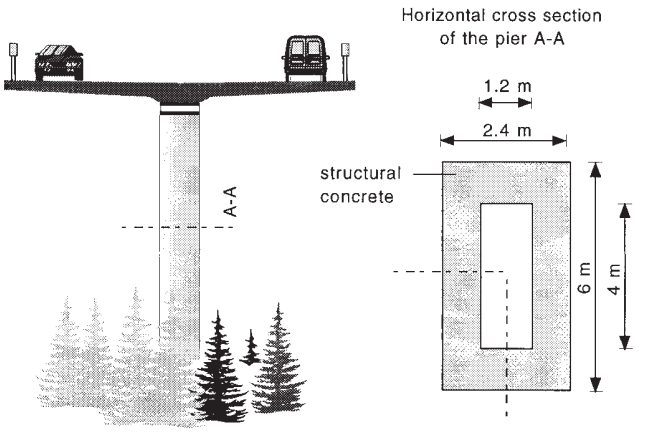

FIG. 12. Schematic Representation of Structure To Be Repaired

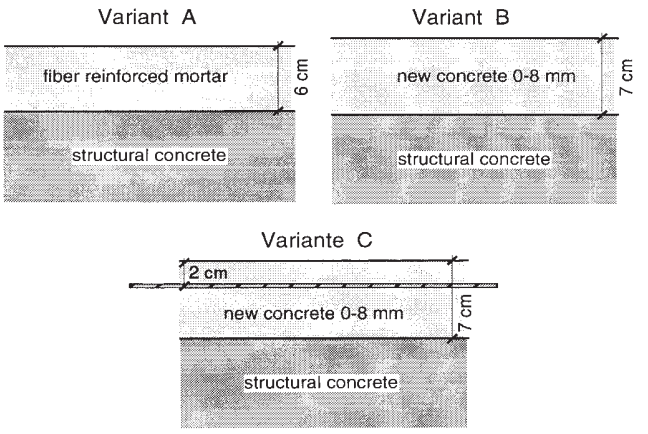

FIG. 13. Three Variants of Pier Repairing System

J. Mater. Civ. Eng., 2001, 13(2): 121-129

TABLE 1. Material Properties of Overlays and Substrates

Material (1)	Young modulus E (GPa) (2)	Fracture energy G_f (N/m) (3)	Tensile strength f_t (MPa) (4)	s_1 (MPa) (5)	w_1 (mm) (6)	w_2 (mm) (7)	Coefficient of shrinkage α (%) (8)
Mortar (A)	14 ± 3	97	3.0 ± 0.6	0.53	0.036	0.164	1.6
Concrete (B) and (C)	40 ± 4	105	5.0 ± 1.0	0.6	0.03	0.105	2.0
Old concrete	41 ± 6	112	3.8 ± 1.2	0.5	0.037	0.17	1.0

TABLE 2. Mechanical Properties of Interface

Interface (1)	Fracture energy G_f (N/m) (2)	Tensile strength f_t (MPa) (3)	Maximum crack opening w (mm) (4)
Variant A	85	2.0 ± 0.8	0.085
Variants B and C	95	2.5 ± 0.9	0.076

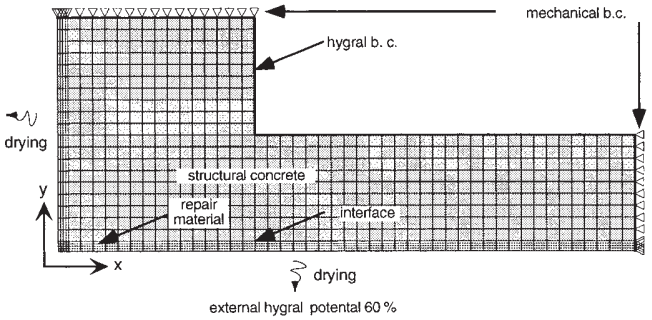

FIG. 14. Finite-Element Modelization of One-Fourth of Column

First, all the relevant material parameters of the repair materials and of the old concrete that are needed in the numerical model have been determined by means of appropriate experiments and subsequent inverse analyses. The determined properties are given in Table 1. Composite specimens consisting of the repair materials were cast on top of a prismatic element of the old concrete of the bridge columns in the laboratory. The mechanical properties of the interface have been determined on these specimens. The measured properties of the interfaces are given in Table 2.

For symmetry reasons, only one-fourth of a horizontal cross section of the column will be considered. Fig. 14 shows the finite-element idealization of the structure to be analyzed. The outer surface of the structure has been exposed to an average RH of 60%, whereas the inner surface has been assumed to be sealed. Furthermore, both materials are assumed to be initially in hygral equilibrium, with 100% RH. The moisture evolution in the structure has been simulated.

Based on the calculated time-dependent moisture distributions, stress and crack analyses have been carried out.

Variant A

Fig. 15 shows the induced hygral stress distribution in the x-direction after a drying time of roughly 4 months. As can be expected, the highest tensile stresses are located in the outer layers of the overlay, regions subjected to the highest hygral gradients.

In Fig. 16 the calculated stress profiles along a cross section are shown for six selected drying times. As can be seen, the tensile strength of the overlay material (3 MPa) was never reached. During the performed analysis, tensile stresses were always <1.6 MPa. The peak value has been reached after a drying time of around 40 days. As the drying process proceeds,

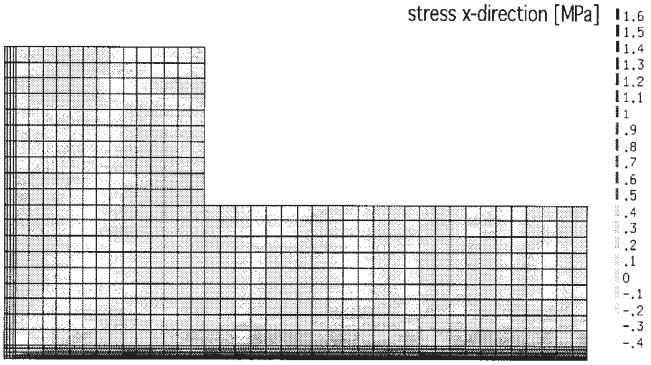

FIG. 15. Stress Distributions σ_x for Variant A after 4 Months of Drying

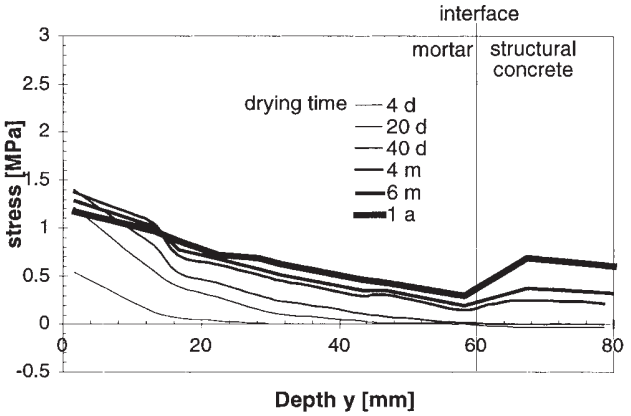

FIG. 16. Stress Distributions σ_x for Variant A at Six Different Drying Times

the peak value of the tensile stresses decreases slowly. This can be explained by the fact that the steepness of the hygral gradient is decreasing. For the case of variant A, cracking and delamination can not occur under the assumed conditions. Damage is avoided because of the relatively low Young's modulus and coefficient of shrinkage, as has already been demonstrated in the sensitivity analysis.

Variant B

The results of the analysis in the case of variant B are totally different. Roughly 7 days after the beginning of the drying process, the first fictitious cracks distributed along the outer layer of the overlay appear. Fig. 17 shows stress profiles along the most damage affected cross section of the system at six different drying times, and Fig. 18 shows the corresponding crack-opening profiles. Some days after the occurrence of the first damage, a limited number of well-defined fracture process zones (FPZs) are formed. As can be seen in Fig. 18, after a drying period of 20 days, a 19-mm-deep FPZ is formed in the overlay. The front of this FPZ corresponds to the peak of the stress curve shown in Fig. 17. The tensile stresses in the FPZ are reduced because of softening of the material. As the drying

J. Mater. Civ. Eng., 2001, 13(2): 121-129

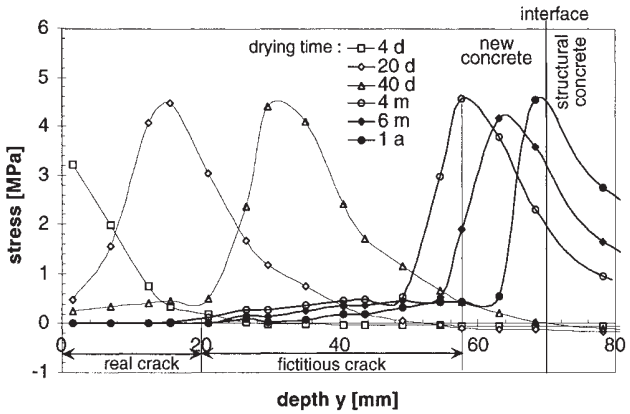

FIG. 17. Stress Distributions σ_x for Variant B at Six Different Drying Times

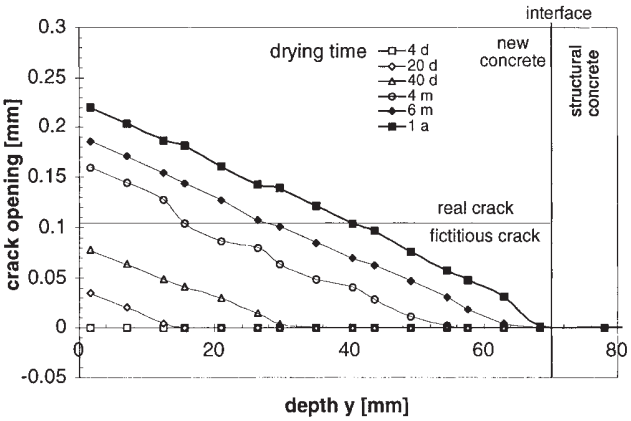

FIG. 18. Crack Opening Profiles for Variant B at Six Different Drying Times

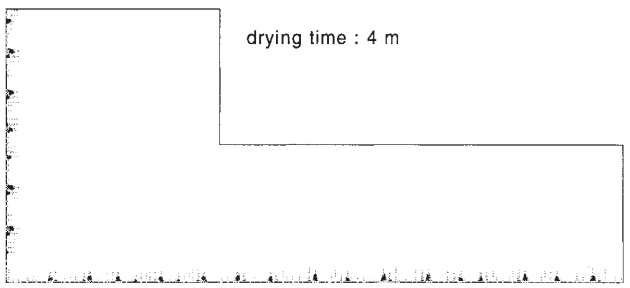

FIG. 19. Crack Distribution in Global System for Variant B after 4 Months of Drying

proceeds, the FPZ becomes wider and wider and moves gradually toward the old concrete. After an advanced drying time (roughly 45 days), a real crack starts to develop in the outer layer of the overlay. As can be seen in Fig. 18, a real crack, approximately 20 mm deep, is created after 4 months. The real crack is a stress-free zone, as can be seen from the corresponding stress profile shown in Fig. 17. At the same period, the total length of the damaged zone (real crack and FPZ) is roughly 55 mm. This length increases to roughly 70 mm after a drying period of 1 year. The maximum crack-mouth opening is 0.27 mm. Fig. 19 shows crack pattern (crack distribution) after a drying time of 120 days.

It can be concluded that the risk of damage in case of variant B is extremely high. The comparatively high Young's modulus and coefficient of shrinkage of the repair layer are responsible for the severity of the damage. Note that the relatively high tensile stress (5 MPa) of this repair material is no advantage with respect to cracking.

Variant C

Because of the identical hygromechanical parameters of the repair concrete of variants C and B, the first damage occurs at roughly 7 days. Because of steel reinforcement, the crack evolution at advanced drying times differs strongly from the previous case (variant B). Stress distributions and crack-opening profiles along the most damaged cross section of the repair system are shown for different drying times in Figs. 20 and 21, respectively. At low drying times (i.e., 25 days), stress distribution and crack opening are nearly the same as in variant B. At this stage of drying, the reinforcing bar is only lightly activated, tensile stresses in the bar are 1.2 and 7.8 MPa at 20 and 25 days, respectively, and the concrete around the reinforcement remains in the linear elastic regime (the region is uncracked). As the crack further propagates and crosses the bars, the stresses in the near-steel zone of the microcracked concrete are partially carried by the reinforcement and partially by the damaged material. After a given state of damage, tensile stresses generated in the bar increase rapidly; the stress values are 17, 39.5, and 76 MPa at 30, 40, and 100 days, respectively. The tensile stresses in concrete at 20 mm from the free surface at 20 days (1.2 MPa in the steel) are the same (roughly 2.5 MPa) as at 40 days (39.5 MPa in the steel), because at 20 days this region is still in a linear elastic regime whereas at 40 days this zone is already microcracked, which means that the material is in a softening regime. As can be seen from Fig. 21, which shows crack-opening profiles, the presence of the reinforcing steel slows down considerably the crack propagation toward the substrate. After a drying period of roughly 4 months, the crack propagation rate is extremely reduced as compared to the previous case (variant B). A second effect of the reinforcement with respect to damage is that the maximum

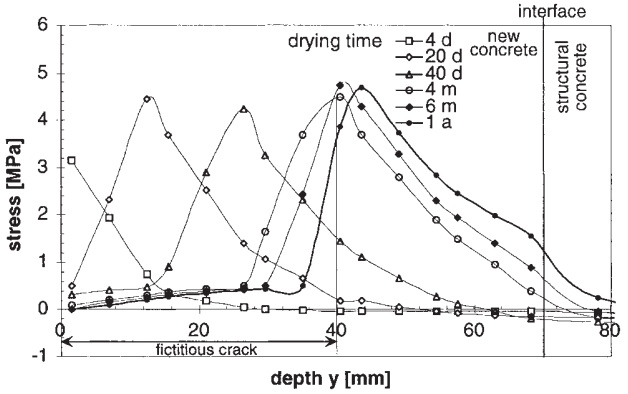

FIG. 20. Stress Distributions σ_x for Variant C at Six Different Drying Times

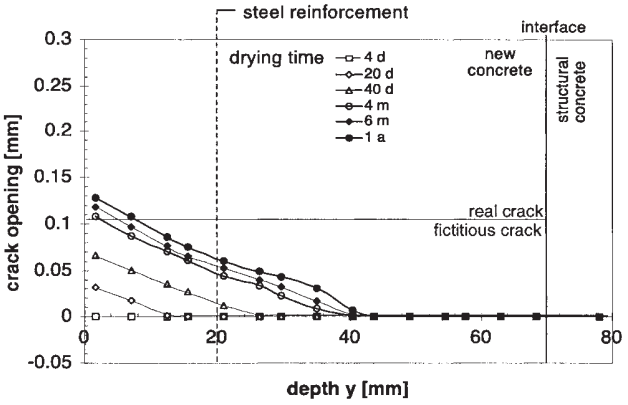

FIG. 21. Crack Opening Profiles for Variant C at Six Different Drying Times

J. Mater. Civ. Eng., 2001, 13(2): 121-129

crack opening is remarkably reduced, roughly by a factor of 2. At the same time the number of macrocracks per unit length increases. These benefic effects are also observed in practice. Because of the simultaneous reduction in width and length of the cracks, their shapes are roughly similar for both variants. Embedding steel bars in the repair concrete clearly decreases the severity of the drying-induced damage. It must be stated, however, that the risk of corrosion of the reinforcement cannot be neglected. Finally it can be concluded that variant A (fiber-reinforced mortar) is the most suitable for a durable rehabilitation of the columns.

CONCLUSIONS

A numerical model based on realistic material laws has been developed. This model allows one to study damage evolution in concrete structures subjected to hygral gradients. Time-dependent and moisture-dependent material laws can be taken into consideration. This model was validated by two different experiments (i.e., the instrumented ring test and a concrete repair system). By applying this numerical model, an intensive parametric study has been carried out. The relevant results are reported in this contribution. Based on the performed sensitivity analysis, criteria for risk of damage are derived. The proposed numerical method can be applied to the design of a concrete repair layer for arbitrary initial and boundary conditions. This approach was applied to a case study. The described method (i.e., a combination of experimental and numerical studies) is a powerful tool for optimizing cement-based materials in particular to avoid shrinkage cracking and delamination.

APPENDIX I. REFERENCES

Bazant, Z. P. (1988). ''Material models for structural analysis.'' *Mathematical modelling of creep and shrinkage of concrete*, Z. P. Bazant, ed., Wiley, New York.

Bazant, Z. P., and Oh, B. H. (1983). ''Crack band theory for fracture of concrete.'' *Mat. and Struct.*, Paris, 16, 155–172.

DIANA Users' manual—Release 6.1. (1996). Diana Analysis BV, Delft, The Netherlands.

Emmons, P. H., McDonald, J. E., and Vaysburd, A. M. (1993). ''Some compatibility problems in repair of concrete structures—A fresh look.'' *Proc., 3rd Int. Colloquium on Mat. Sci. and Restoration*, Vol. 1, Expert Verlag, 836–857.

Hillerborg, A., Modéer, M., and Petersson, P. E. (1976). ''Analysis of crack formation and crack growth in concrete by means of fracture mechanics and finite elements.'' *Cement and Concrete Res.*, 6, 773–782.

Martinola, G. (1998). ''Entwicklung zuverlässiger zementgebundener Beschichtungen auf Beton, KTI Project (1994–1998).'' *Internal Rep. IBWK-ETHZ*, Swiss Federal Institute of Technology, Zürich, Switzerland (in German).

Martinola, G., and Sadouki, H. (1998). ''Combined experimental and numerical study to assess shrinkage cracking of cement-based materials.'' *Int. J. for Restoration of Build. and Monuments*, Freiburg, Germany, 4(5), 479–506.

Martinola, G., Sadouki, H., and Wittmann, F. H. (1996). ''Numerisches Modell zur Beschreibung der Eigenspannungen und der Rissbildung in Beschichtungssystemen.'' *Proc., 4th Int. Colloquium on Mat. Sci. and Restoration*, Vol. 1, Aedificatio Verlag, Freiburg, Germany, 393–407 (in German).

Martinola, G., Sadouki, H., and Wittmann, F. H. (1997). ''Fissuration et délamination d'une couche de réparation appliquée sur un élément de béton.'' *Proc., 15th Rencontres Universitaires de Génie Civil: Expérimentation et Calcul, EC. 97*, Vol. 2, 267–276 (in French).

Martinola, G., Trausch, J. L., and Sadouki, H. (1997). ''The ring test for optimizing low shrinkage concrete.'' *Proc., RILEM-WTA-Seminar on High Perf. of Cement-Based Mat. WTA-Rep. Ser. No. 15*, 173–194.

Roelfstra, P. E., and Wittmann, F. H. (1986). ''Numerical method to link strain softening with failure of concrete.'' *Fracture toughness and fracture energy of concrete*, F. H. Wittmann, ed., Elsevier Science, Amsterdam, 163–175.

Rots, J. G. (1988). ''Computational modeling of concrete fracture.'' PhD thesis, Delft University of Technology, Delft, The Netherlands.

Sadouki, H., and van Mier, J. G. M. (1997). ''Simulation of hygral crack growth in concrete repair systems.'' *Mat. and Struct.*, Paris, 30, 518–526.

Shah, S. P., Karaguler, M. E., and Sarigaphuti, M. (1992). ''Effects of shrinkager-reducing admixtures on restrained shrinkage cracking of concrete.'' *ACI Mat. J.*, 89, 289–295.

Trausch, J. L., and Wittmann, F. H. (1996). ''Einfluss der Grenzfläche auf das Haftvermögen zementgebundener Beschichtungen.'' *Proc., 4th Int. Colloquium on Mat. Sci. and Restoration*, Vol. 1, Aedificatio Verlag, Freiburg, Germany, 409–424 (in German).

Wittmann, F. H. (1998). ''Application of fracture mechanics to optimize repair systems and protective coatings for reinforced concrete structures.'' *Proc., FRAMCOS-3, Fracture Mech. of Concrete Struct.*, Vol. 3, Aedificatio Publishers, Freiburg, Germany, 1707–1714.

Wittmann, F. H., and Müller, T. (1994). ''Adherence and fracture energy.'' *Adherence of young on old concrete*, Aedificatio Publishers, Freiburg, Germany, 97–106.

Wittmann, X., Sadouki, H., and Wittmann, F. H. (1989). ''Numerical evaluation of drying test data.'' *Proc., 10th Int. Conf. on Struct. Mech. in Reactor Technol.*, Vol. Q, 71–79.

APPENDIX II. NOTATION

The following symbols are used in this paper:

$\mathbf{C}$ = compliance matrix;
$D(h)$ = moisture transfer coefficient;
E = Young's modulus;
f_t = tensile strength;
G = shear modulus;
G_f = fracture energy;
h = hygral potential;
$J(t, \tau)$ = creep function;
$q(t)$ = rate of endogeneous drying;
s_1 = stress, parameter of softening diagram;
t = time;
w = moisture potential;
w_1 = crack opening, parameter of softening diagram;
w_2 = crack opening, parameter of softening diagram;
x, y = space variables;
$\alpha(h)$ = hygral coefficient of shrinkage;
β = shear retention factor;
ε = strain;
σ = stress; and
τ = duration of loading or shear stress.

J. Mater. Civ. Eng., 2001, 13(2): 121-129

Article n°8

Control of Cracking in Early Age Concrete, -Mihashi & Wittmann (eds.)
© 2002 Swets & Zeitlinger, Lisse, ISBN 90 5809 506 1

Material properties influencing early cracking of concrete

F.H.Wittmann, G.Martinola & H.Sadouki
Institute for Building Materials, Swiss Federal Institute of Technology, Zürich, Switzerland

ABSTRACT: Maintenance free service life of concrete structures is often limited by crack formation. Hygral and thermal gradients are most often the origin of cracks in concrete. On the basis of a numerical model it is shown that optimum values for different material properties such as moisture diffusivity, coefficient of shrinkage, elastic modulus and fracture energy, have to be identified in order to avoid cracking. Combinations of these material properties, which certainly lead to crack formation, are determined. Numerical results are verified by means of an instrumented ring test. A combination of properties of concrete, which will certainly not lead to crack formation, is obtained. Results are compared with properties of conventional concrete. This approach can be extended to take into consideration thermal cracking and combinations of hygral and thermal stresses.

1 INTRODUCTION

The durability of concrete structures is strongly related to the penetration of water into the porous concrete structure. Water often contains substances, which once transported into the porous system of concrete can damage the concrete structure by various external or internal mechanisms. To increase the durability of concrete structures means essentially to abate the penetration of water into the structure. This means also a reduction of the number of cracks and in case of unavoidable cracks,, a minimal crack opening. Because of their specific applications in service, some concrete structures like cellars or water containers need to be completely free of cracks. In the domain of building restoration, deteriorated or contaminated concrete layers have often to be removed from existing structural elements and subsequently replaced by new concrete or mortar. In most cases an empirical approach is chosen instead of an engineering analysis and rigorous design, so that failure of some systems, e.g. cracks in the overlay and delamination of the overlay may occur requiring further repair of already repaired systems.

Fresh concrete is mixed with typically 120 to 170 litres of water per cubic meter. Part of this water is consumed during hydration; the remaining part is still enough to supply the young porous concrete with moisture content, which is in hygral equilibrium with 95-100% relative humidity. This means that pores with a radius smaller than 100 nm will remain water filled by capillary condensation. Concrete structures are usually exposed to a much lower humidity. As a consequence, a long-lasting drying process starts immediately after demoulding. A free concrete layer contracts drying the drying process. In a drying layer, a hygral gradient originates a stress field if the concrete layer is restrained in a statically indeterminate system. Tensile eigenstresses can exceed the tensile strength even for moderate environmental drying conditions. In this case crack formation occurs. So cracking in concrete structures due to shrinkage is a complex matter involving the shrinkage rate, the restraint level, the creep properties, the Young's modulus and fracture mechanics parameters of concrete. All of these material properties develop with time. One major aim of a concrete designer should be to generate a concrete mix with reduced shrinkage in order to guarantee a low probability of crack formation (Alvaredo 1994).

In this contribution a restrained shrinkage ring test, (Shah, Karaguler & Sarigaphuti 1992), Carlson & Reading 1988, Grzybowski & Shah 1990, Sarigaphutti, Shah & Vinson 1993) which allows to quantify the risk for crack formation under shrinkage, is presented. A sensitivity analysis of the material properties is carried out in order to identify the influence of these properties on shrinkage cracking. The analysis and the evaluation of the test results give us the possibility to optimise cement-based materials with respect to crack formation.

2 THEORETICAL BASIS OF THE HYGRO-MECHANICAL BEHAVIOUR OF CEMENT-BASED MATERIALS

2.1 *Physical description of drying*

Moisture variations in cement-based materials may result from internal drying induced by the hydration reaction of cement and water at early age (self-desiccation), and from drying caused by climatological conditions of the environment during the life-span of the structure. The knowledge of moisture distributions in space and time in a structure is of utmost importance for analysing crack formation and further crack growth.

The size and the shape of pores present in a porous material exert a direct influence on the transport mechanism of water. Despite the knowledge of the basic individual phenomena involved, such as capillary transport, diffusion, surface diffusion, it is not yet possible to determine quantitatively the influence of each of them on the global moisture transfer in a porous material such as concrete or mortar. At the macroscopic level (i.e. in a representative finite volume of the porous and heterogeneous structure) the aforementioned difficulty can be circumvented by defining a concentration-dependent transfer coefficient, which integrates all contributions of the different mechanism in the global mass transfer. In this phenomenological description, the transient moisture flow can be described according to the second Fick's law (Pihalajavaara 1965, Bazant & Najjar 1971). If h represents the relative humidity held in the pores, then the Fick's law is described by the following partial differential equation:

$$\frac{\partial h}{\partial h} = div\left[D(h)\cdot grad(h)\right] \tag{1}$$

in which $D(h)$ is the moisture transfer coefficient depending on the pore humidity h and on the composition of the cement-based material.

Equation (1) describes in a realistic way the transient moisture flow in normal matured concretes with relatively high water-cement ratio in which self-desiccation can be neglected (w/c≥0.5). However, for young cement-based materials with low w/c ratio, the available water is less than required to maintain equilibrium with a relative humidity of around 100%, self-desiccation then plays an important role. In order to take into account the contribution of the endogenous drying in the description of the drying process, a moisture-sink term $q(t_0,t)$ as function of the hydration time t_0 is added to the right-hand side of Equation 1. The extended equation governing the global drying process is then written as follows:

$$\frac{\partial h}{\partial h} = div\left[D(h)\cdot grad(h)\right] + q(t_0,t) \tag{2}$$

For calculating the drying process of a porous system exposed to a given atmosphere, equation (2) must be solved taking adequate boundary conditions and initial conditions into consideration. In general, convective boundary conditions are used to describe the exchange of humidity between the exposed surfaces of the system and the surrounding atmosphere. This condition is expressed as follows:

$$j_n = \gamma\cdot(h_\Gamma - h_0)\cdot n \tag{3}$$

with j_n = moisture flux normal to the exposed surface Γ, γ= hygral convection coefficient, h_Γ= humidity on the surface Γ, h_0 = humidity of the surrounding atmosphere.

In general, γ depends on many factors, such as the actual humidity, the temperature and the speed of the wind at the convective surface. In this analysis, a constant mean value of γ will be

used; this is justified in our case because the specimens are assumed to be exposed to a constant atmosphere.

The initial condition describing the spatial humidity field in the porous structure at the beginning of the exposure to a drying atmosphere is given by means of the following set of equations:

$$h(t=0, x_i, y_i, z_i) = h_i \tag{4}$$

with (x_i,y_i,z_i) = localisation of a point in the volume, h_i = corresponding humidity potential value at the beginning of the analysis.

This value takes into account the moisture loss induced by the autogenous desiccation before the structure being exposed to the atmosphere.

2.2 *Description of the hygro-mechanical behaviour*

In this contribution, hygral variations induced by endogenous and/or exogenous desiccation are considered as the only driving force for crack formation and propagation. During drying of a cement-based material, hygral gradients develop, inducing differential deformations in the specimen. If a hypothetical fibre of the material is allowed to shrink under an infinitesimal drop Δh in equilibrium humidity, the resulting shrinkage strain can be expressed as follows:

$$\Delta\varepsilon_{h.sh.} = \alpha_{h.sh.}(h) \cdot \Delta h \tag{5}$$

with $\Delta\varepsilon_{h.sh.}$ = infinitesimal free shrinkage, $\alpha_{h.sh}(h)$ = coefficient of shrinkage depending on the material composition and on the actual pore humidity.

If the drying material is restrained with respect to shrinkage strain, tensile eigenstresses will develop. Often, these tensile stresses are large enough to cause cracking, and adequate fracture mechanics tools must then be applied. Elastic softening models can describe crack formation and crack growth in cement-based materials in a realistic way. Models incorporating softening are mostly based on the Fictitious Crack Model (FCM) originally developed by Hillerborg and co-workers (Hillerborg, Modéer & Petersson 1976).

In this model, the stress-deformation diagram under tension subdivided into a pre-peak stress-strain diagram, which is characterised by the Young's modulus E of the material and the tensile strength f_t, and a post-peak behaviour. After the maximum stress is reached bifurcation occurs. Within the fracture process zone (FPZ) strain softening takes place while outside this zone the material continues to react as linear elastic. The post-peak relation is fully characterised by the shape of the softening curve. The area under this curve is the fracture energy G_f. The model is shown schematically in Figure 1.

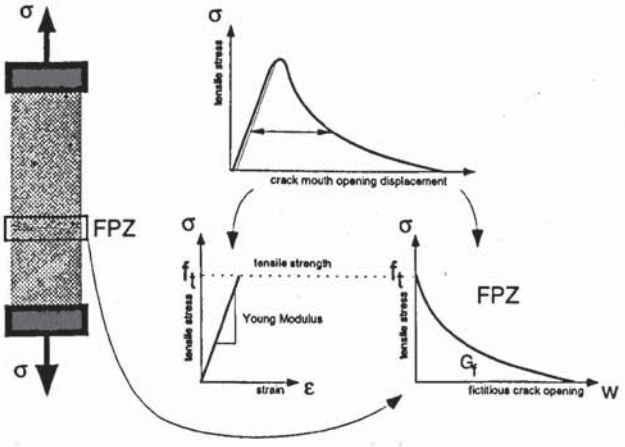

Figure 1. Basic elements of the fictitious crack model (FCM) according to (Hillerborg, Modéer & Petersson 1976).

The Crack Band Model (CBM) as developed by Bazant and Oh (Bazant & Oh 1983) is quite similar, except that it assumes that the crack growth occurs in a band, rather than along a line. The CBM forms the basis for the smeared crack model in the finite element code DIANA (Martinola, Sadouki & Wittmann 1996, DIANA 1996, Sadouki & van Mier 1997) used in this work.

During the period of the hygral loading, the deformations of the material increase due to creep. Creep can be described by means of visco-elastic models (Kelvin chains). The visco-elastic relation between strain and stress is derived in our case from measured creep curves, which describe the instantaneous and transient strain after a unit force loading. The properties of Kelvin chains are then obtained by curve fitting of the measured creep function (DIANA 1996).

3 DESCRIPTION OF THE RING-TEST

3.1 *Experimental set-up*

Different experimental techniques are used to assess the resistance against cracking of cement-based materials when subjected to restrained drying shrinkage. The restrained ring type test is used in our case (Shah, Karagulaer & Sarigaphuti 1992, Carlson & Reading 1988, Grzybowski & Shah 1990, Sarigaphutti, Shah & Vinson 1993).

The technique consists of casting a ring of mortar or concrete around a very stiff steel ring. Figure 2 shows schematically a two-dimensional (2D) representation of the ring specimen. After a preliminary curing period, the two opposite flat sides of the mortar ring are sealed. The ring is exposed to a given drying atmosphere (T=20°C, 45% relative humidity (R.H.)). Under these conditions, drying is allowed through the outer circumferential surface only. Due to hygral shrinkage, the mortar ring attempts to contract against the restraint of the steel ring.

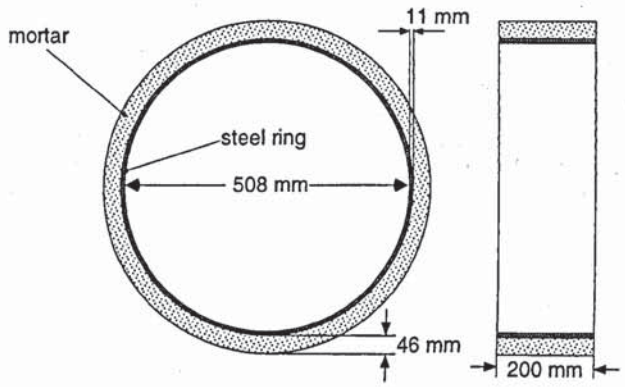

Figure 2. 2D representation of the ring specimen

The mortar rings are 46 mm in radial thickness and 200 mm in height. The internal and external diameters of the steel ring are 508 and 519 mm respectively. Several strain gauges are placed at different positions on the inner surface of the steel ring. Figure 3 shows the positions of the strain gauges and of the thermocouples. Deformations on the steel are then measured automatically as function of the drying time.

3.2 *Numerical modelling*

As mentioned before the non-linear finite element program (DIANA 1996) has been used to simulate the combined flow-stress analysis. The analysis is performed in 2D (radial moisture diffusion only). Figure 4 shows the finite element idealization of the steel-mortar ring specimen. During the flow analysis, finite elements representing the steel are removed and no moisture flux is allowed through the inner surface of the mortar ring.

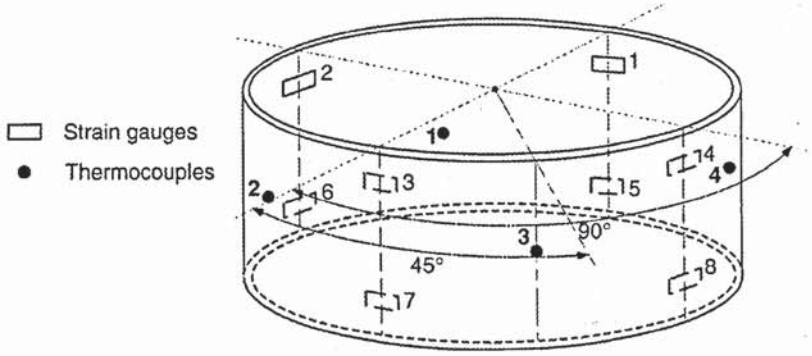

Figure 3. Localization of the thermocouples and of the strain gauges on the inner surface of the steel ring

In DIANA, the global deformation field ε is separated into four components as follows:

$$\varepsilon = \varepsilon^{el.} + \varepsilon^{crack} + \varepsilon^{creep} + \varepsilon^{h.sh.} \tag{6}$$

with: $\varepsilon^{el.}$: elastic strain, ε^{crack} : crack strain, ε^{creep} : creep strain, $\varepsilon^{h.sh.}$: hygral shrinkage strain

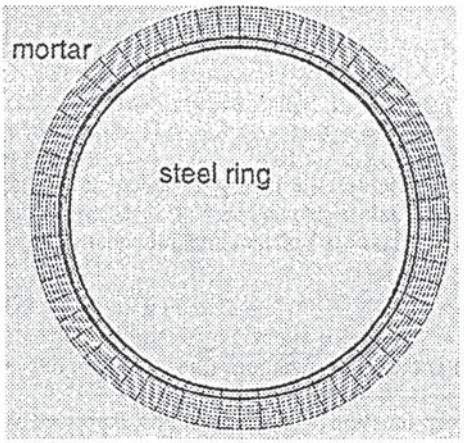

Figure 4. FE idealization of the ring specimen

The time-dependent humidity distribution, calculated from the transient analysis, is stored in a file for every time step Δt. For the stress and fracture analysis, the incremental hygral load Δh is converted into a strain field ($\varepsilon^{h.sh.}$) via the hygral shrinkage coefficient $\alpha(h)$. The two analyses are uncoupled, meaning that it has been assumed that the moisture flow is not affected by cracking.

The multiple fixed smeared crack approach developed by Rots (Rots 1988) is used to simulate the crack formation and growth in the mortar ring. The strain is decomposed into an elastic part and a crack strain. The crack strain is obtained by dividing the crack opening by the crack bandwidth, which is the size of the finite element. Due to the cracking of the material the shear stiffness is usually reduced. This is taken into consideration by correcting the shear modulus G using a reduction factor β. Crack initiation is governed by a linear tension cut-off criterion and a threshold angle between two consecutive cracks. A detailed description of the model can be found in Rots (Rots 1988). The shape of the stress-crack opening is assumed to be bilinear. The parameters are obtained by an inverse analysis of the load-displacement diagram measured on wedge-splitting test specimens. The main characteristics of the crack modelling are schematically shown in Figure 5.

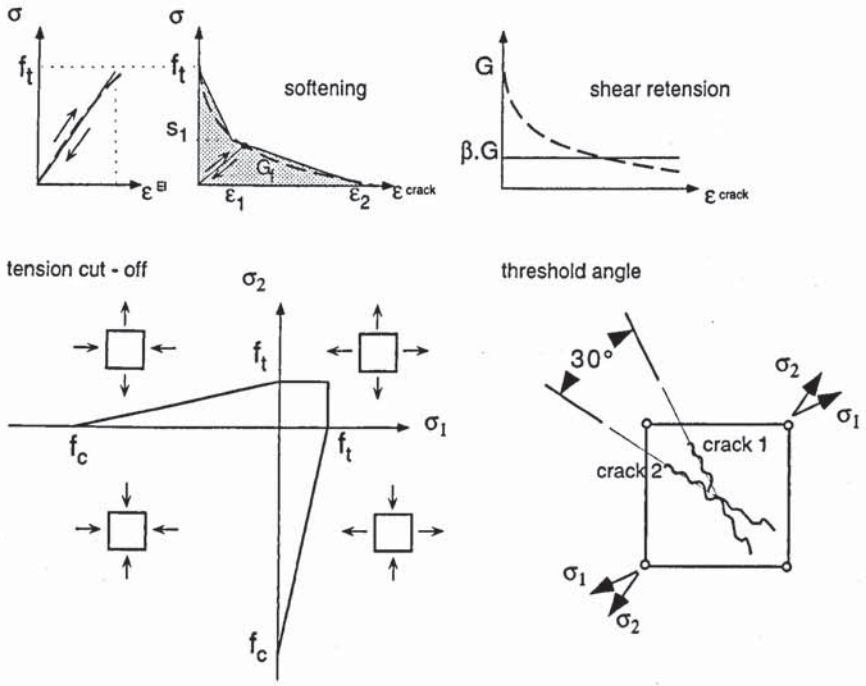

Figure 5. Characteristics of the crack model

As it has been mentioned, creep is described by the visco-elastic theory. In calculating time dependent strains, the history of the stresses must be taken into account. By assuming the principle of superposition (Boltzmann), one obtains the classical Volterra integral equation:

$$\varepsilon(\tau)=\int_{-\infty}^{t} J(t,\tau)\overline{C}\dot{\sigma}(\tau)d\tau \tag{7}$$

where t is the time, τ is the duration of load, $J(t,\tau)$ is the creep function, $\overline{C}$ is the compliance matrix and $\dot{\sigma}(t)$ is the stress rate.

The material behaviour is characterized by the creep function $J(t,\tau)$. This can be expressed as sum of exponential functions (Dirichlet series). The Dirichlet series can be physically interpreted as a Kelvin chain model.

$$J(t,\tau)=\sum_{\alpha=0}^{\infty}\frac{1}{E_\alpha}\left[1-e^{\frac{t-\tau}{\lambda_\alpha}}\right] \quad \text{with} \quad \lambda_\alpha=\frac{\eta_\alpha}{\eta_\alpha} \tag{8}$$

where: E_α is the equivalent stiffness, λ_α is the retardation time and η_α is the viscosity.

The stiffness E_α and retardation time λ_α of the units in the chain are estimated from the measured creep curve by a non-linear least squares method. More details on this approach can be found in (DIANA 1996).

In this numerical simulation statistically distributed mechanical properties of the mortar are introduced. This leads to realistic localisation processes. The Young's modulus E and the tensile strength f_t are assumed to be randomly distributed over all finite elements representing the mortar. Scatters of 10% and 20% of the mean values of E and f_t respectively are assumed, in accordance with the measured standard deviations of these properties. The random variables E and f_t are adequately correlated.

Table 1: Composition of standard and optimised mortar

	Aggregate Size [mm]	w/c [-]	cement [kg/m3]	aggregate [kg/m3]	fibers [%]*	PD [%]	SP [%]*	AEA [%]*
Stand. Mortar	0-4	0,5	500	1500 -	-	-	-	-
Opt. Mortar	0-6	0,36	375	1620	1	15	1.2	0.2

*of the cement weight
[PD is the polymer dispersion, SP is the high performance plasticiser, AEA is the air entraining agents]

4 MATERIAL PROPERTIES FOR THE NUMERICAL ANALYSIS

4.1 *Composition of mortar*

As an example in this contribution two different mortars are investigated. The first one is a standard mortar with a maximum aggregate size of 4 mm. The second one is a special mortar developed for repair of concrete structures. In this case the mechanical properties are optimised in order to reach low elastic modulus and high fracture energy. Carbon fibres, superplasticisers (SP), air-entraining agents (AEA) and polymer dispersions (PD) were added. The mix-design of the two mortars is shown in Table 1.

4.2 *Hygral properties*

Cylindrical specimens were drilled two days after hydration and prepared for radial drying. These specimens were stored in different degrees of surrounding humidity with constant temperature. The moisture loss was measured periodically as function of drying time. The experimental data were used for the determination of the diffusion coefficient by means of an inverse analysis (Wittmann, Sadouki & Wittmann 1989). The moisture diffusivity is described by an exponential function of humidity with two parameters a and b:

$$D(h) = a \cdot e^{(b \cdot h)} \tag{9}$$

with a, b being Parameters, h being the Humidity potential. The moisture diffusion coefficients of the two mortars are given in Figure 6.

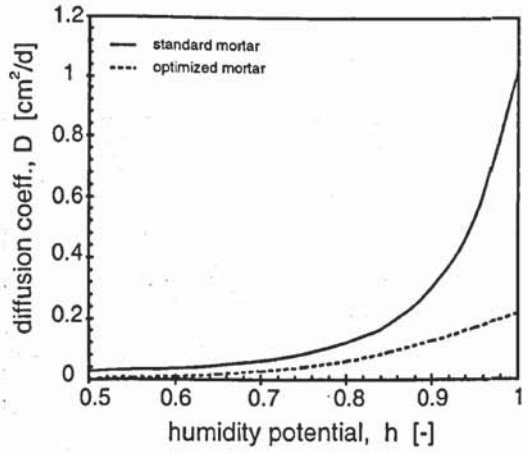

Figure 6. Moisture diffusion coefficients of the standard and optimised mortar

Mortars with a low water-cement rare subject to internal drying. This phenomenon was measured on sealed specimens with capacity sensors. The standard mortar does not undergo self-desiccation, because of its comparatively high water-cement ratio.

Figure 7 shows the evolution of the pore humidity as function of the age for both mortars. In the optimised mortar, the endogenous drying will finally reduce the internal humidity to approximately 75%.

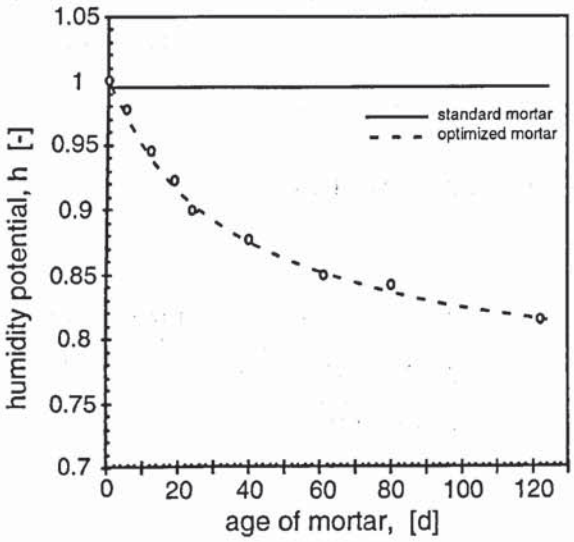

Figure 7. Evolution of pore humidity under sealed conditions due to self-desiccation

The moisture sink term $q(t_0,t)$ is obtained by derivation of the time dependent humidity decrease function (see Figure 7):

$$q(t)=\frac{dh}{dt}=-\frac{0.358}{(43.8+t)^2}+\frac{0.358}{43.8+t} \tag{10}$$

The total hygral deformation is induced by both the external drying shrinkage and the internal autogenous shrinkage. The humidity-dependent final shrinkage was measured on cylindrical specimens, which were exposed to different degrees of relative humidity. The obtained experimental data are fitted. The results are given in figure 8(a).

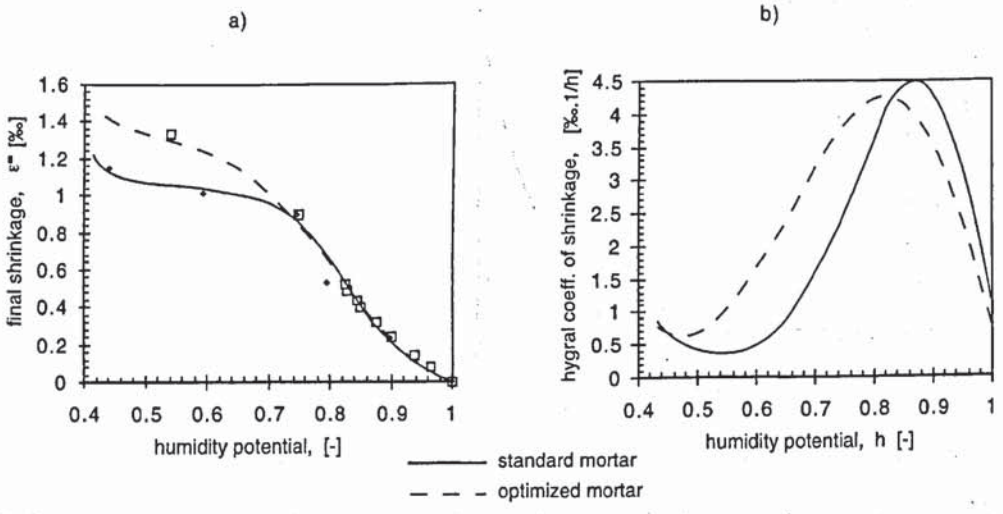

Figure 8. (a) Final shrinkage and (b) hygral shrinkage coefficient as function of humidity

The hygral shrinkage coefficient, as shown in Figure 8(b) is given as the first derivative of the final shrinkage curve with respect to humidity potential h:

$$\alpha_{sh.}(h) = \frac{d\varepsilon^{\infty}(h)}{dh} \tag{11}$$

4.3 *Mechanical properties*

The moduli of elasticity of the mortars are measured on cylindrical specimens tested under compression. The determination of fracture parameters such as fracture energy and strain softening has been performed by means of the wedge splitting test, as described in (Roelfsta & Wittmann 1986). The inverse analysis allows the computation of the parameters of the bilinear softening diagram (Brühwiler 1988). The parameters f_t, σ_1, w_1, w_2 are indicated in Figure 9.

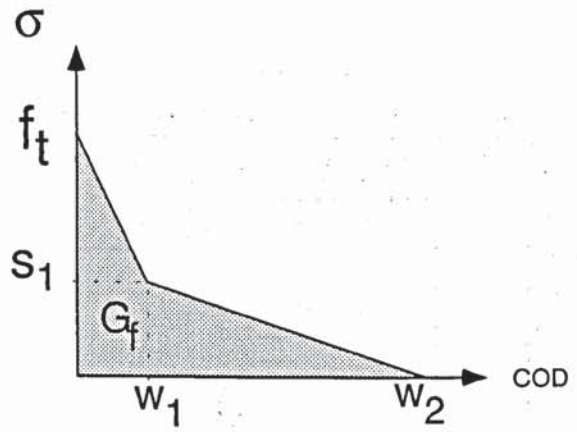

Figure 9. Parameters of the bilinear stress crack-opening diagram

Mechanical properties of the two mortars measured at the age of 7 days are shown in Table 2.

Table 2: Mechanical properties of standard and optimised mortar

	G_f [N/m]	E [GPa]	f_t [Mpa]	s_1 [MPa]	w_1 [mm]	w_2 [mm]
Stand. Mortar	52	29.0±2.9	2.1±0.39	0.37	0.026	0.134
Opt. Mortar	288	20.0±1.9	4.4±0.42	0.53	0.090	0.350

Creep functions were measured on prismatic specimens. The mortars were 3 days old at the time of loading. Half of the number of the specimens were completely sealed, the others were exposed to a drying atmosphere relative humidity of 70%. The specimens were then loaded in compression with a stress level with 35% of their expected compressive strength and the deformation were recorded as function of loading time. The measured basic creep and drying creep curves are given in Figure 10.

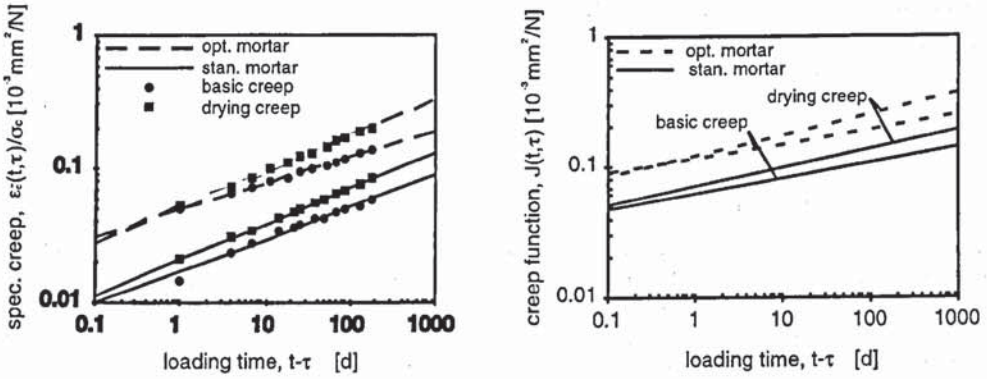

Figure 10. Basic and drying creep functions

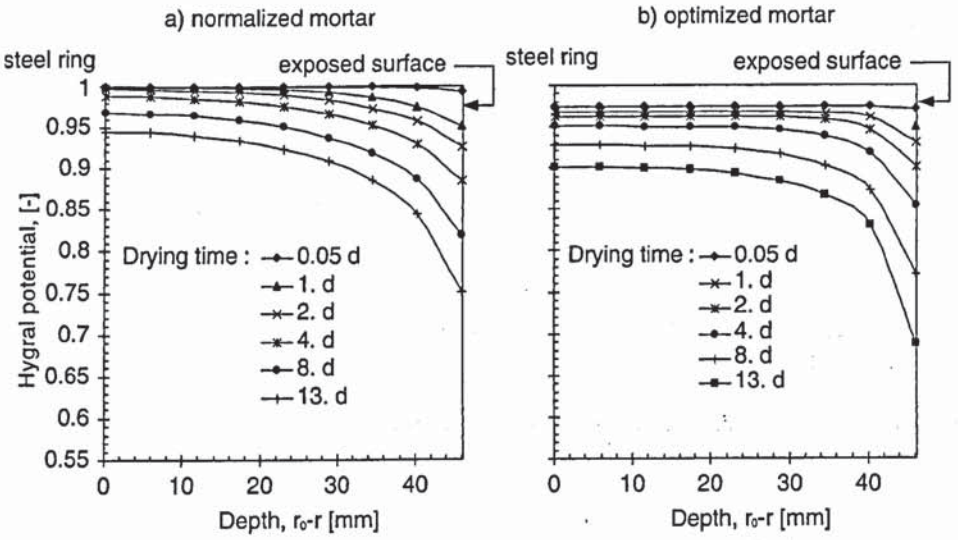

Figure 11. Moisture distribution at different drying times of the standard mortar, (b) Moisture distribution at different drying times of the optimised mortar (with endogenous drying)

5 NUMERICAL SIMULATION AND VALIDATION OF THE PROPOSED MODEL

5.1 *Humidity distribution*

Figures 11(a) and 11(b) show the simulated radial humidity profiles in the two mortar ring specimens for six drying times. In the case of the standard mortar shown in Figure 11(a), the pore humidity at the beginning of drying exposure was in equilibrium with a relative humidity of 100%. In the case of fibre-reinforced mortar, this value was 97.5% only, due to the self-desiccation during the curing period (see Figure 11(b)). By comparing the profiles of the materials, one can clearly see that in case of the standard mortar the hygral gradient, at a given drying time, increases slowly from the inner to the outer surface. In the second case, because of the self-desiccation of the material (low w/c), humidity distributions show a large plateau region, but high hygral gradients occur at the outer layers near the exposed surface.

5.2 *Crack formation and propagation*

5.2.1 *Standard mortar*

Results of the numerical simulation are described elsewhere (Martinola & Sadouki 1998). In the standard mortar ring, the first fictitious cracks appear on the outer layer of the ring, which is the region with the highest hygral gradients, already at $t = 0.9$ day after exposure. Note, that since these cracks still can transfer load, they must be regarded as local fracture process zones where microcracking and crack bridging occur. During the next time steps the fictitious cracks gradually increase in width. As the drying process proceeds, cracking is governed by two phenomena, (a) a number of cracks, closely positioned with respect to one another disappears (close) again, (b) other more distantly distributed cracks continue to grow at certain integration points of the elements of the outer layers of the ring. This is due to the well-known fact that cracks unload the immediate vicinity depending on their length. At $t = 5.6$ days, a well-defined micro-cracking band is formed and runs radially from the outer surface of the mortar to the inner steel ring. From this cracked band the first macro-cracking is developed. About 2.2 days later ($t = 7.8$ days), a second macrocrack is formed in another region of the ring nearly opposite the first crack.

After that the two macro-cracks increase gradually in width and micro-cracking occurs in the interface between the mortar and the steel ring. This type of crack evolution is similar to that obtained for a concrete repair system subjected to drying (Sadouki & van Mier 1997).

In the corresponding experiment, the first macro-crack appeared after 5.2 days and a second one after 11 days. With the experimental set-up it was not possible to follow the evolution of the crack opening precisely. An estimation of the width of the visible cracks was possible only. The exact occurrence of the two real cracks was made possible by analysing the time evolution of the strains recorded at different positions on the inner surface of the steel ring.

5.2.2 *Optimised mortar*

A similar numerical analysis has been performed for the fibre-reinforced mortar ring. The evolution of the cracking process is analogue to the former case (standard mortar). Nevertheless, the first dispersed fictitious cracks appeared later, more precisely 7 days after the beginning of drying of the specimen. This is due to several reasons, namely lower moisture diffusivity, higher tensile strength, and lower elastic modulus as compared to the standard mortar. The first real macro-crack (band of real cracks) occurred at $t = 17.8$ days. Two days later a second fictitious crack has grown significantly, but only 9 days later became a real crack. After further drying, most of the dispersed fictitious micro-cracks close and the two real macro-cracks have increased in width.

In the case of the corresponding experiment, one macro-crack occurred only and suddenly after a drying time of 17.5 days with a measured width of 2 mm. The second crack was not observed. In the meantime many experiments have been carried out using the ring test.

6 PARAMETRIC STUDY

A numerical parametric study has been carried out based on the good agreement between the experimental results, performed on two mortars with totally different hygro-mechanical properties, and on the corresponding numerical results obtained by the proposed model.

The main aim of this study is to define the most relevant material parameters influencing shrinkage cracking and, consequently, to be able to decide which material parameters must be optimised in order to reduce the first of damage as much as possible.

Because of the large number of the material parameters involved in the cracking process and their mutual interaction one or two material parameters are varied only while the others are kept constant and equal to the reference values in each simulation. The material parameters, considered as variables, are changed in a reasonable way, meaning that a real mortar having these hypothetic properties can be made.

The reference values of the hygro-mechanical properties are listed below:

- Young modulus	E	=	25 Gpa
- Tensile strength	f_t	=	3.0 N/mm^2
- Fracture energy	G_f	=	97.5 N/mm
- Softening parameters	s_t	=	0.5 N/mm2
	w_1	=	0.04 mm
	w_2	=	0.15 mm
- Diffusion coeff.	$D(h)$	=	$a_0 \cdot \exp(b_0 \cdot h)$ cm^2/d
	a_0	=	0.00005
	b_0	=	10
- Coeff. of shrinkage	$\alpha_0(h)$	=	$-a \cdot (h-c)/b^2 \cdot \exp(-0.5 \cdot ((h-c)/b)^2)$ ‰/h
	a	=	0.953
	b	=	0.204
	c	=	1.042

In the following parametric study, the material parameters, which were varied, are given in the corresponding figures. The final result of each study consists of curves showing the evolution of the crack opening of the dominant crack in the mortar ring as function of the drying time.

In a first analysis, the influence of the moisture diffusivity on the crack evolution has been studied. Three different moisture diffusivities are considered as it can be seen in Figure 12(a). In Figure 12(b), the resulting crack opening is described as function of the drying time. It is evident from this figure that the moisture diffusivity plays an important role in the crack formation. The apparition of the first damage (first fictitious crack) is delayed at low moisture diffusivity and the crack opening increases with the moisture diffusivity. In order to measure the importance of the moisture-dependent coefficient of shrinkage $\alpha(h)$ with respect to the risk of cracking, the peak value (a_0) of the function $\alpha = \alpha(h)$ has been varied. The resulting curves are shown in Figure 13(a). In Figure 13(b), the corresponding results regarding the crack evolution as function of the drying time are shown.

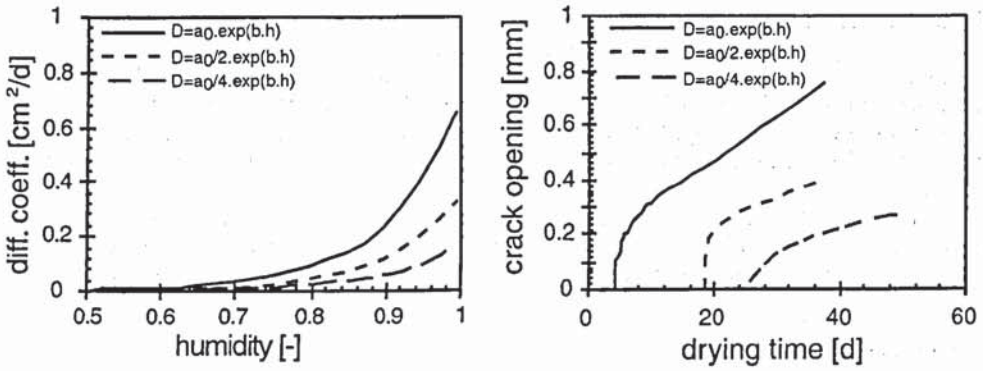

Figure 12. (a) Moisture diffusivities as function of humidity, (b) Corresponding crack opening as function of drying time

It can clearly be seen as it can be anticipated that the coefficient of shrinkage has a very strong influence on the crack formation. For low values ($\alpha \leq \alpha/4$) of this material parameter, cracking becomes insignificant.

In a next study, two parameters are varied at the same time, the Young's modulus E and the coefficient of shrinkage α (h). In Figure 14 is equal to the reference value and three different values are assumed for the Young's modulus. As it can be seen in this figure, in all cases the cracking is extremely severe, depending on the Young's modulus at least one real crack (crack-opening w higher than w_2 of the bilinear diagram) is formed after a drying time between 45 and 60 days. As the drying progresses, the cracks become wider and wider.

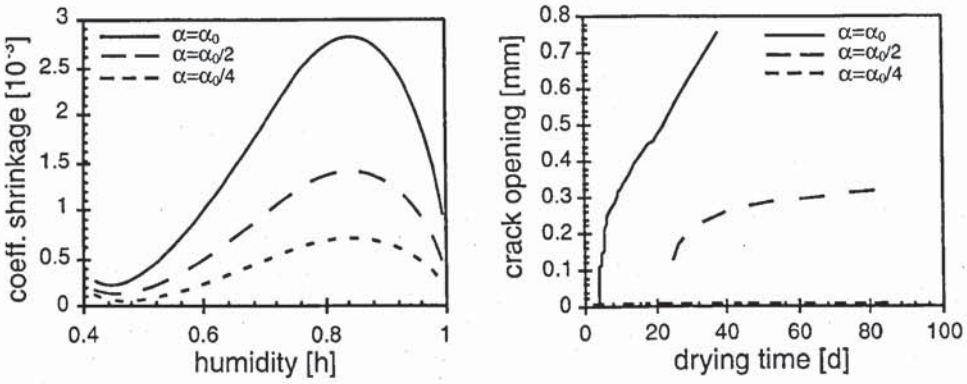

Figure 13. (a) Three different functions for the coefficient of shrinkage as function of humidity; (b) Crack opening as function of drying time for the three shrinkage function shown in Fig. 13 (a).

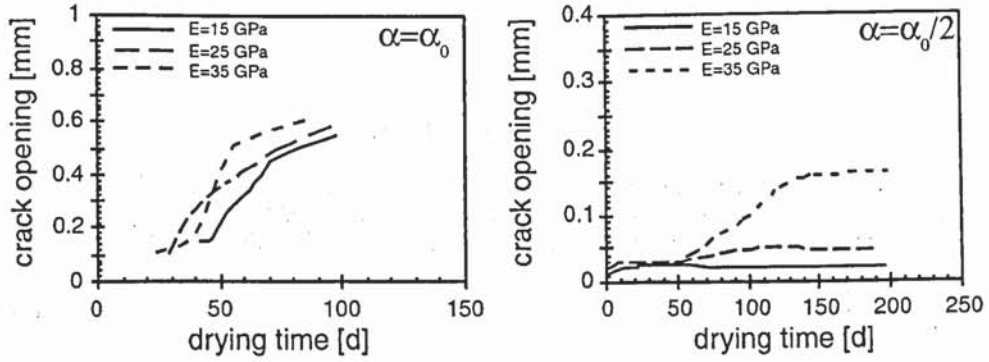

Figure 14. Crack opening as function of drying time for three different Young's moduli: (a) $a = a_0$, (b) $a = 0.5\ a_0$.

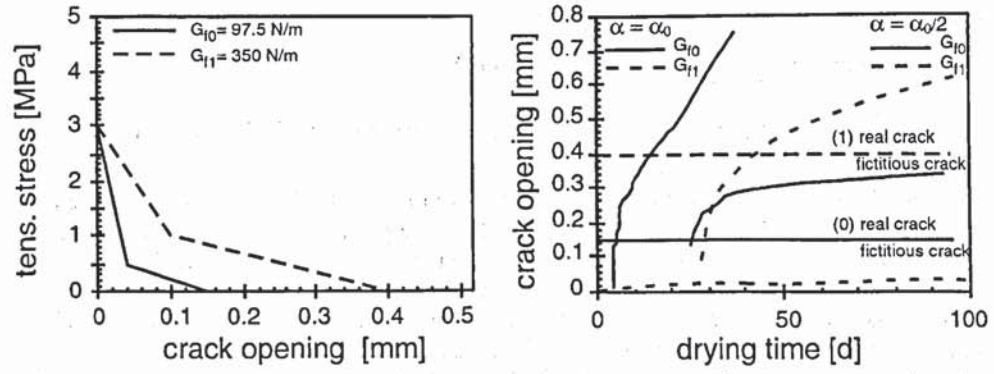

Figure 15. (a) Two softening diagrams with different strain softening and fracture energy, (b) Crack opening as function of the drying time for 4 different variations of the couple of parameters $a(h)$, G_f.

In Figure 14 the same analysis has been performed, but after reducing the maximum coefficient of shrinkage to 50% of its reference value ($\alpha = \alpha_0/2$). In this case, the risk of crack formation is strongly reduced. If the Young's modulus is lower than 25 GPa, the previously formed fictitious cracks tend to close gradually as the drying advances.

If α is further reduced to 25% of its reference value ($\alpha = \alpha_0/4$), the simulations carried out showed that the cracking is insignificant (see Figure 13) even for a high Young's modulus (E = 35GPa).

In the last analyses, fracture energy G_f and the coefficient of shrinkage $\alpha(h)$ have been varied simultaneously. Figure 15(a) shows the two bilinear diagrams, adopted for stress-crack-opening in these analyses. For both softening diagrams, two values of the shrinkage coefficient $\alpha(h)$ are used. Figure 15(b) shows the simulated crack evolution as function of the drying time. For $\alpha = \alpha_0$, an increase of the fracture energy G_f to 350N/m retards the formation of the first crack, but the severity of the damage (evolution of the crack opening) remains roughly the same at later drying times. In case of a reduced shrinkage coefficient the situation is different.

For both fracture energies, the risk of cracking is reduced as compared to most previous cases. But if in case of a reduced $\alpha(h) = \alpha_0(h)/2$, the fracture energy is increased to G_f =350N/m the risk of a real crack is practically vanished.

During drying and autogenous shrinkage which both are displacement controlled phenomena, tensile strength plays a minor role with respect to crack formation. In fact, this tendency was also confirmed by the sensitivity analysis performed later. A relation between tensile strength and crack development could not be found.

7 RESULTS OF AN EXTENSIVE PARAMETRIC STUDY

With the combination of results of numerous numerical simulations it is possible to build a diagram, which indicates the risk of crack formation as function of fracture energy, Young's modulus and mean coefficient of shrinkage. The latter mean value is defined as follows:

$$\overline{\alpha} = \frac{1}{h_2 - h_1} \cdot \int_{h_1}^{h_2} \alpha(h) \cdot dh \tag{12}$$

with $h_1 = 0.5$ (50% R.H.) and $h_2 = 1.0$ (100% R.H.)

A 3-dimensional representation of this area is shown in Figure 16.

In many standard codes the shrinkage is defined by the strain measured on a specimen during drying from 100% to 50% R.H. The corresponding value according to the presented theory can be approximated by the following expression:

$$\varepsilon_{near}(100\% - 50\%) \cong \sum_{t\to 0}^{t\to\infty(100\%-50\%)} = \overline{\alpha} \cdot (h_2 - h_1) \tag{13}$$

with $\sum_{t\to 0}^{t\to\infty(100\%-50\%)}$ representing the final shrinkage strain measured when the test specimen is in hygral equilibrium with 50% R.H.

The shrinkage strain is also indicated on the z-axis in Figure 16. Figure 17 shows these two-dimensional sections of the area shown in Figure 16 in the plane fracture energy – shrinkage. In order to introduce a safety factor for the interpretation and the utilization of the diagram which covers the variation of the results, a transitional area between the cracking and the crack free zone is defined. Using this 2-dimensional representation a minimization of the risk of shrinkage cracking of a particular cement-based material can be achieved.

A mortar with a Young's modulus (E) 25 Gpa, a fracture energy G_f=200N/m and a final shrinkage strain of 0.8‰ (see point A1 in Figure 17) for instance will crack during a drying period, in case of restrained mechanical boundary conditions. In order to avoid crack formation the properties of this mortar have to be changed. Point A1 has to be moved from the critical zone (cracking) to the safe zone (no cracking). There are 3 different possibilities: (a) either the shrinkage strain is reduced to 0.6‰ (see point A2 in Figure 17); (b) the fracture energy is increased to 300 N/m (see point A3 in Figure 17); or (c) the Young's modulus is reduced to 15

GPa. In practice, it is possible to achieve all these 3 modifications by (a) reducing the cement content; (b) by addition of fibers; and (c) by using air-entraining agents or low-modulus aggregates. All combinations of these parameters that lead to a shift of point A1 into the safe zone, are also possible.

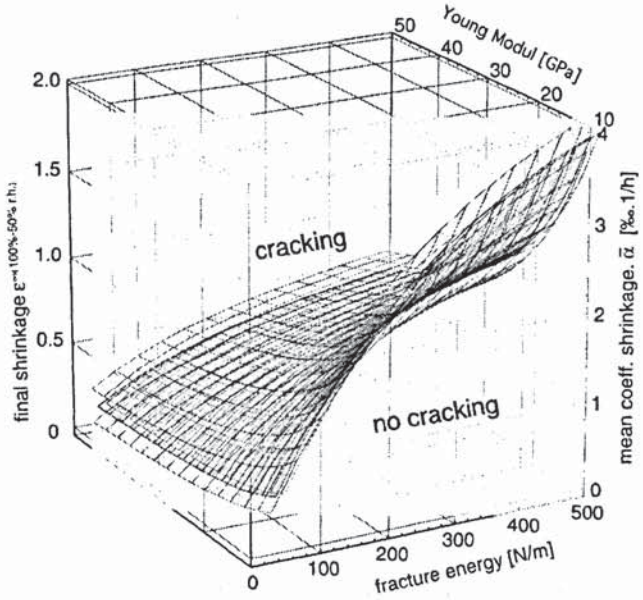

Figure 16. Risk of crack formation as function of fracture energy, coefficient of shrinkage and Young's modulus

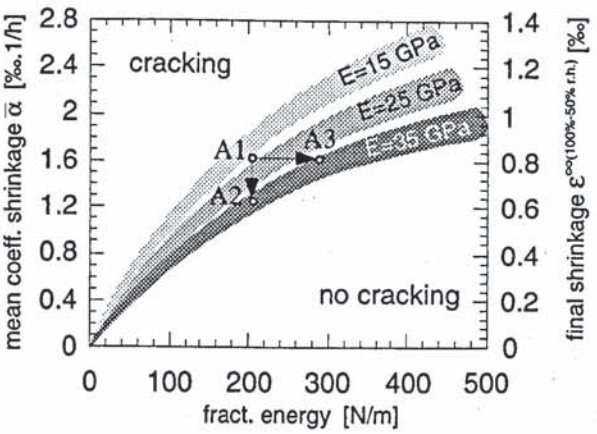

Figure 17. Risk of crack formation as function of fracture energy, coefficient of shrinkage and Young's modulus

8 CONCLUSIONS

A numerical model based on realistic material laws has been developed, which allows us to study early crack evolution in concrete structures subjected to hygral gradients. Time and moisture dependent material laws can be taken into consideration.

This numerical model was validated by comparison with results from the ring test carried out with two qualities of mortars having totally different hygro-mechanical material laws.

Based on the results described in this contribution, the importance of different material properties for early crack formation in concrete can be quantified. The following conclusions can be drawn:

- By applying this numerical model, an intensive parametric study has been carried out. An area separating safe parameter combinations from those which imply high risk for crack formation has been identified.
- The model can capture the main features observed experimentally, especially the drying time at which the macro-cracks will occur.
- A low moisture diffusivity retards crack formation and slows down crack opening but in can not avoid cracking alone.
- Among all material parameters the coefficient of shrinkage is the most sensitive parameter with respect to crack formation and crack extension. A high coefficient of shrinkage will always lead to severe damage.
- The instrumented ring test is a powerful technique to study the tendency of cement-based materials with respect to their risk of hygral cracking.
- The described method, i.e. a combination of experimental and numerical studies is a powerful tool to optimize cement-based materials and in particular to avoid shrinkage cracking.

REFERENCES

Alvaredo, A.M. *Drying Shrinkage and Crack Formation.* Building Material Reports No. 5. Aedificatio Publishers (1994)

Bazant, Z.P. & Najjar, L.J. *Drying of concrete as a nonlinear diffusion problem.* Cement and Concrte Research, 1, 461-473 (1971)

Bazant, Z.P. & Oh, B.H. *Crack band theory for fracture of concrete*, Materials and Structures, 16, 155-172 (1983)

Brühwiler, E. *Bruchmechanik von Staumauerbeton unter quasi-statischer und erdbebendynamischer Belastung*, Dissertation No. 739, Ecole Polytechnique Fédéral de Lausanne (1988)

Carlson, R.W. & Reading, T.J. *Model Study of Shrinkage Cracking in Concrete Walls*, ACI Structural Journal, 85, No. 5, 395-404 (1988)

DIANA, Users Manual – Release 6.1, Diana Analysis BV, Delft, The Netherlands (1996)

Grzybowski, M. & Shah, S. *Shrinkage Cracking of Fiber Reinforced Concrete*, ACI Materials Journal, 87, No. 2, 138-148 (1990)

Hillerborg, A., Modéer, M. & Petersson, P.E. *Analysis of crack formation and crack growth in concrete by means of fracture mechanics and finite elements*, Cement and Concrete Research, 6, 773-782 (1976)

Martinola, G., Sadouki, H. & Wittmann, F.H. *Numerisches Modell zur Beschreibung der Eigenspannungen und der Rissbildung in Beschichtungssystemen*, in Procedings of 4th Intern. Colloq. On Materials Science and Restoration, F.H. Wittmann, editor, Aedificatio Publishers, 393-407 (1996)

Martinola, G. & Sadouki, H. Combined Experimental and numerical study of shrinkage cracking of cement-based materials, Int. J. Restoration 4, 1-15 (1998)

Pihalajavaara, S.E. *On the main features and methods of investigation of drying and related phenomena in concrete*, PhD thesis, Univ. of Helsinki, Finland (1965)

Roelfstra, P.E. & Wittmann, F.H. *Numerical Method to Link Strain Softening with Failure of Concrete*, Fracture Toughness and Fracture Energy of Concrete, F.H. Wittmann, editor, Elsevier, Amsterdam (1986)

Rots, J.G. *Computational modelling of concrete fracture*, PhD thesis, Delft University of Technology, The Netherlands (1988)

Sadouki, H. & van Mier, J.G.M. *Simulation of Hygral Crack Growth in Concrete Repair Systems*, Materials and Structures, 30, 518-526 (1997)

Sarigaphutti, M., Shah, S.P. & Vinson, K.D. *Shrinkage Cracking and Durability Characteristics of Cellulose Fiber Reinforced Concrete*, ACI Materials Journal, 90, No. 4, 309-318 (1993)

Shah, S.P., Karaguler, M.E. & Sarigaphuti, M. *Effects of Shrinkage-Reducing Admixtures on restrained Shrinkage Cracking of Concrete*, ACI Materials Journal, 89, 289-295 (1992

Wittmann, X., Sadouki, H. & Wittmann, F.H. *Numerical Evaluation of Drying Test Data*, Trans. 10th Intern. Conf. On Structural Mechanics in Reactor Technology, Vol Q, 71-79 (1989)

Article n°9

9th International Conference on Fracture Mechanics of Concrete and Concrete Structures
FraMCoS-9
V. Saouma, J. Bolander and E. Landis (Eds)

DOI 10.21012/FC9.221

DEVELOPMENT OF A COMPUTATIONAL MULTI-PHYSICAL FRAMEWORK FOR THE USE OF NONLINEAR EXPLICIT APPROACH IN THE ASSESSMENT OF CONCRETE STRUCTURES AFFECTED BY ALKALI-AGGREGATE REACTION

BEN FTIMA M.[*], SADOUKI H.[†] AND BRÜHWILER E.[††]

[*]École Polytechnique de Montréal
B.O. Box 6079, Station Centre-ville
e-mail: mahdi.ben-ftima@polymtl.ca

[†]École Polytechnique Fédérale de Lausanne
EPFL ENAC IIC MCS, GC B2 386, Station 18
e-mail: hamid.sadouki@epfl.ch

[††] École Polytechnique Fédérale de Lausanne
EPFL ENAC IIC MCS, GC B2 386, Station 18
e-mail: eugen.bruehwiler@epfl.ch

Key words: Alkali-aggregate reaction, multi-physical, concrete model, nonlinear, explicit.

Abstract: This paper proposes an innovative methodology for the use of the explicit approach in the assessment of concrete structures affected by alkali-aggregate reaction (AAR). Efficiency of the explicit approach has been proven in previous works for the case of large concrete structural models with high degree of nonlinearity. In the proposed methodology, the strain is decomposed into mechanical, thermal, creep, shrinkage and AAR strain components. The AAR component is computed according to Saouma and Perotti model [1] for the anisotropic distribution of the volumetric expansion and according to Larive model [2] for the AAR kinetics. One advantage of the approach is that it can be used with any existing concrete model that has undergone a rigorous verification and validation (V&V) process for the mechanical part. In this work the EPM3D concrete model [2] implemented as a user-subroutine in Abaqus-Explicit is used. The general methodology is based on three different finite element analyses: thermal implicit, hygral implicit and the final nonlinear multi-physical explicit analysis. An innovative formulation to address the problem of time scale difference between the implicit and explicit approaches is presented. A new incremental numerical formulation is presented to correctly handle the dependency of the AAR kinetics on the temperature field in case of cyclic temperature variation. A verification example is presented at the material level, along with qualitative assessment of the cracking pattern of an existing hydraulic structure affected by AAR. This last application at structural level demonstrates the efficiency of the suggested methodology and the feasibility within an industrial context.

1 INTRODUCTION

Alkali-aggregate reaction (AAR) is an acid-base chemical reaction known to occur in concrete for certain types of aggregates and under certain moisture, confinement and temperature conditions. Structural manifestation of this reaction is due to the expansive nature of the alkali-silica gel, product

of this reaction, when it comes in contact with moisture. This internal expansion generally leads to micro-cracking, loss of strength and stiffness at the material level. Major distortions can occur at the structural level leading to functional problems of the onboard installation. As an example, expansion in hydraulic structures like dams and powerhouses can interfere with the operation of the flow gates or turbines. Macro-cracking and failure may occur when the deformations are prevented or when concrete structural components are unable to accommodate these large deformations.

Numerical models can be carried out to predict structural displacements, stresses and damage resulting from AAR. Finite elements linear analyses have been successfully applied to predict displacement field in structures and were validated with field monitored data (e.g. [4]). The analyses based on fictitious thermal loading conditions found on a trial-and-error basis using the past monitored data were successfully applied in the engineering community. These analyses predict quite reasonably the displacement field of structures affected by AAR but cannot be used to predict the stress field or the damage pattern. More recently, a new family of models called coupled chemo-mechanical models started to emerge ([5], [1], [6], [7], [8]). In these models, kinetics of the chemical reaction is simulated within the nonlinear mechanical constitutive model. Experimental works were performed in order to characterize the parameters needed in these models. Among these works, the experiments of Larive [2] and Multon [9] carried out at the LCPC Laboratory in France are of great importance since they characterized for the first time both the kinetics and the anisotropy of the swelling process depending on stress and environmental conditions. AAR in concrete structures is still considered as a complex phenomenon mainly due to its multi-physical nature. The lack of experiments to validate available numerical models on the element and structural level is obvious. Based on past investigations, it can be concluded that the major influencing factors that need to be considered within a constitutive model are: kinetics of the reaction and of gel swelling process, effects of humidity and temperature fields, effects of the stress field and confining conditions on the anisotropy of swelling, effects of cracking, intrinsic degradation of material and creep effects. Considering all of these aspects within a nonlinear finite element framework and for a real structural model can result in computational challenges and makes questionable the feasibility of these sophisticated analyses within a real industrial context. Furthermore, it is known that AAR results over time in a generalized cracking pattern and highly nonlinear behavior when compared to conventional mechanical loading. Cracking in concrete is handled numerically by the softening behavior on the stress-strain curve of the constitutive law which generally results in numerical difficulties with the conventional implicit and iterative numerical resolution algorithms. Non convergence issues can occur for large concrete models with no or light reinforcement as it is the case for example for hydraulic structures [10]. According to authors past experience, mesh refinement in a concrete model can result in a numerical damage pattern very close to the real cracking pattern even when the smeared crack approach is used. Convergence difficulties may again arise when using finer mesh and force analyst to use a coarse mesh making difficult the comparison between model and reality. The objective of this work is to develop a new computational framework suitable for the multi-physical simulation of AAR within concrete structures. For the first time, the explicit quasi-static approach which was initially developed within metal forming field is used. The approach is based on three constitutive analyses: thermal analysis, hygral analysis and a final multi-physical analysis. An innovative time scaling technique is presented in order to deal with the

time scale difference between these three analyses. The efficiency and feasibility of the approach are demonstrated via a real industrial example of a hydraulic structure. This work is a part of a larger long term research program that addresses the issue of practical use of nonlinear finite elements for the assessment of hydraulic structures affected by AAR.

2 EXPLICIT QUASI-STATIC APPROACH

The explicit dynamics approach has been developed and successfully applied in the industrial field of metal forming, at the beginning of the nineties [11]. Following this approach, the nonlinear problem is solved in a dynamic manner and conventional nodal forces are converted into inertia forces by assigning lumped masses into the nodes. With comparison to the conventional implicit approach, no iterations are performed, the algorithm advances explicitly in time using a very small time increment to ensure stability. This increment Δt depends on the smallest element of the mesh and can be as low as 10^{-5} to 10^{-7} fraction of the total analysis time. This approach has been successfully extended to the case of civil engineering concrete structures [10] and applied to the industry of hydraulic structures. The original nonlinear static problem is solved in a quasi-static manner by applying all the loads slowly enough with respect to the first mode, to ensure that kinetic energy is negligible compared to the internal strain energy. For a typical civil engineering structure with a fundamental period T_1 ranging from 0.05 sec to 2 sec, this involves a period of analysis t_{exp} ranging from 1 sec to 40 sec considering a ratio of 20 for t_{exp}/T_1. Hence, the approach is more efficient for stiff structures considering the small stable increment time. It was possible for the first time to analyse complex nonlinear models (nonlinear constitutive model and contact condition with friction) with more than three millions degrees of freedom. The parallel computing technique was investigated and benchmark tests showed that computation time can be almost inversely proportional to the number of cores used in the computation. Unlike implicit approach, the global model is divided into N domains corresponding to the number of cores available. This is possible in the explicit approach since there is no need to consider the assembly of the global stiffness matrix as it is the case in the conventional implicit approach. Figure 1 shows an example of domain subdivision of the structural model considered in this work, each color represents a domain. In this case computations are done on a conventional quad-core computer. The model has more than 140 000 elements.

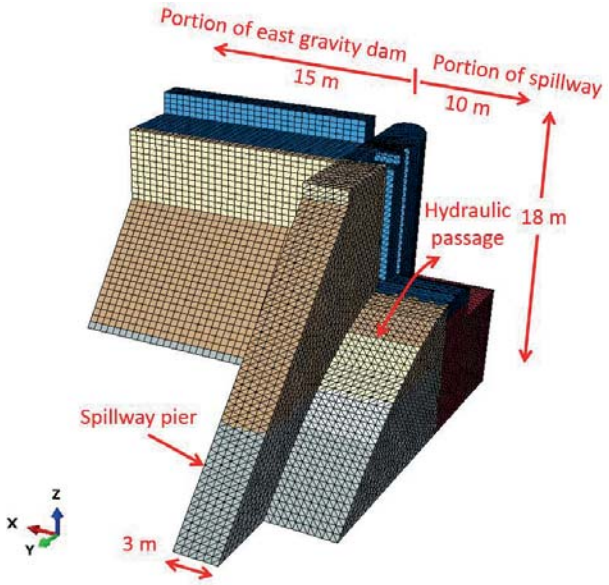

Figure 1: Finite element model of the hydraulic structure

3 EPM3D CONCRETE MODEL

The EPM3D concrete model [3] is a 3D constitutive model that uses the smeared-crack approach and can model tensile cracking and concrete crushing of concrete. EPM3D is an orthotropic 3D strain-rotating crack model. It was programmed under Abaqus-Explicit [12] using the VUMAT user-subroutine interface [13]. It can handle both unreinforced and reinforced concrete applications using, respectively, a G_f law and tension-stiffening

law for the post-cracking regime in the presence of reinforcement. As shown in Figure 2, the model was originally implemented as a purely mechanical constitutive law updating at each increment of time the stress tensor σ_1 and the state dependent variable vector SDV_1, given the stress tensor σ_0 of the previous increment, the state dependent variable vector SDV_0 of the previous increment and the given incremental strain tensor $\Delta\varepsilon$. Over the past ten years, the mechanical constitutive law of EPM3D has undergone a rigorous verification and validation process (V&V) and was used in the hydraulic structures and bridge engineering industries ([14] and [15]). More recently, the participation using this model was ranked the second out of sixty six within an international prediction contest organized by the University of Toronto on the deepest reinforced concrete beam ever tested (4 meters). Over the sixty six participants, only the two first entries predicted the failure loads of both the east and shear span and the west span within 10% of the experimental values [16]. A large coefficient of variation was observed during this contest though the simplicity of the geometry which clearly demonstrates that validation of a purely mechanical constitutive concrete is still an issue in the field of lightly reinforced or non-reinforced concrete structures. This finding supports the decision to include the AAR model within the existing mechanical constitutive law. To the best of author's knowledge, the only AAR model that can be implemented with an existing constitutive model and at the same time handles the major influencing factors cited in the introduction is the one proposed in [1]. This will be developed in the next section.

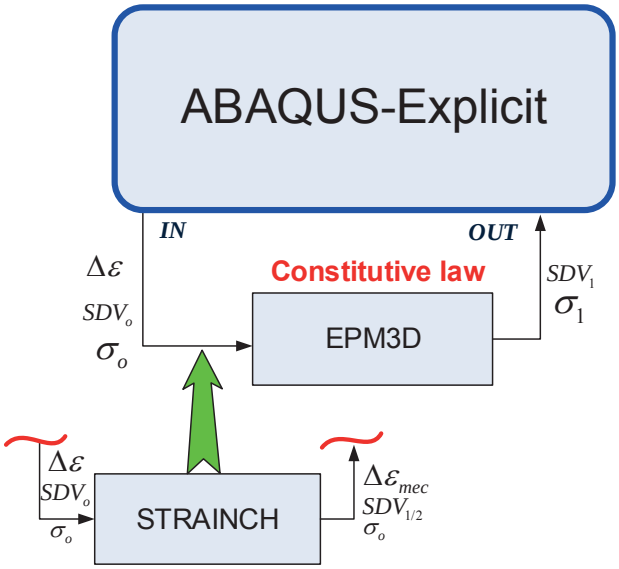

Figure 2: User subroutine implementation and modifications of the existing EPM3D constitutive law

4 MULTI-PHYSICAL SIMULATION OF AAR IN CONCRETE STRUCTURES

4.1 Multi-physical approach

The multi-physical approach developed in this work uses three different analyses as shown in Figure 3 and involves a sequential coupling between thermal, hygral and chemo/mechanical fields. Two transient thermal and hygral analyses are firstly performed in order to compute the thermal and relative humidity fields T(t) and H(t). The thermal analysis is a conventional heat transfer analysis involving conduction and convection heat transfer modes and body heat flux to simulate the exothermic hydration process. The hygral analysis is performed in a similar way using the analogy between heat and hygral flux and using the concept of diffusivity with unit values of densities and specific heat [17]. In both cases, the simulation period of time can be as large as the lifetime span t_{life} of the structure. These two fields are than imported into the final multi-physical analysis which is actually the nonlinear structural analysis involving the modified EPM3D model. This last analysis involves computation over time of the stress field $\sigma(t)$ and the AAR kinetic progress

parameter $\xi(t)$ using the notation and equations of Larive [2]. The first two analyses are performed in a conventional implicit framework. Even if the constitutive equation of the heat transfer law is nonlinear in the case of hygral analysis, due to the dependency of the diffusivity on the hygral field, no convergence difficulties are anticipated. In fact numerical difficulties arise only when a softening behavior exist in the constitutive law. The final analysis however is performed in the dynamic explicit framework. This difference between implicit and explicit frameworks involves a challenging problem of difference in time scales: in the order of several years for the implicit analyses and of few seconds in case of the explicit analyses. This problem will be treated in a later section.

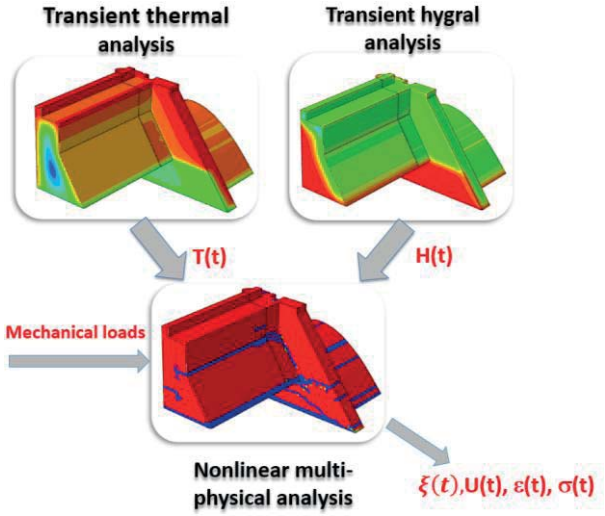

Figure 3: Multi-physical approach.

4.2 Strain decomposition

Similarly to the work of Pan et al. [18], the total strain is decomposed into mechanical, thermal, creep, shrinkage and AAR strains according to the following equation in the incremental form:

$$\Delta\epsilon(t,T,H) = \Delta\epsilon_{mec}(t,T,H) + \Delta\epsilon_{th}(t,T) + \Delta\epsilon_{cr}(t,\sigma_0) + \Delta\epsilon_{sh}(t,H) + \Delta\epsilon_{aar}(t,\xi,T,H,\sigma_0) \quad (1)$$

This equation shows inter alia the coupling between the four fields considered in the study. As shown schematically in Figure 2, the methodology involves at each stable increment time, the computation of the mechanical strain increment from the total strain increment given by Abaqus-Explicit and the remaining thermal, creep, shrinkage and AAR strains as shown in Eq. 1. This is performed via the new subroutine STRAINCH shown in Figure 2. This subroutine additionally updates the state variables vector *SDV* required for the mechanical constitutive law EPM3D.

The following equations are used for the estimation of thermal, creep, shrinkage and AAR strains:

Thermal:

$$\Delta\epsilon_{th}(t,T) = \alpha(T(t) - T_{ini})\delta \quad (2)$$

where α is the coefficient of thermal expansion; T_{ini} is the initial reference temperature and δ is the Konecker's delta.

Creep:

Kelvin-Voigt viscoelastic model (damper η_{ve} and elastic spring E_{ve}) is used, similarly to Pan et al. 2013.

$$\Delta\epsilon_{cr}(t,\sigma_0) = \left(e^{\frac{-E_{ve}}{\eta_{ve}}} - 1\right)\left(\epsilon_{cr}(t-\Delta t) - \frac{[A]\sigma_0}{E_{ve}}\right) \quad (3)$$

Where $[A] =$

$$\begin{bmatrix} 1 & -\nu & -\nu & & & \\ -\nu & 1 & -\nu & & 0 & \\ -\nu & -\nu & 1 & & & \\ & & & 2(1+\nu) & 0 & 0 \\ & 0 & & 0 & 2(1+\nu) & 0 \\ & & & 0 & 0 & 2(1+\nu) \end{bmatrix}$$

and ν is the Poisson's coefficient.

Shrinkage:

Similarly to [17]:

$$\Delta\epsilon_{sh}(t,H) = \alpha_{sh}(H)(H(t) - H(t-\Delta t))\,\delta \quad (4)$$

where α_{sh} is the shrinkage coefficient that depends nonlinearly on the relative humidity field H.

AAR:

Using the same notations as in [1]:

$$\Delta\epsilon_{aar_i}(t,\xi,T,H,\sigma_0) = \Gamma_t(SDV_0).\Gamma_c(\sigma_0).g(H).W_i(\sigma_0).\Delta\xi(t,T,\sigma_0).\varepsilon_{v\infty} \quad (5)$$

where i is a given stress principal direction, Γ_t and Γ_c are retardation factors that depend on the tensile, compressive damage and stress field of the material point in the previous increment, $g(H) = H^8$ is a reduction function that accounts for the influence of humidity, $W_i(\sigma_0)$ is the weighting for redistribution of volumetric AAR expansion in the principal direction i, depending on the stress field as described in [1], $\varepsilon_{v\infty}$ is the long term volumetric AAR strain and $\Delta\xi(t,T,\sigma_0)$is the rate of the AAR reaction given by the following equation:

$$\Delta\xi(t,T,\sigma_0) = \frac{e^{\frac{t}{\tau_c}}(e^{\frac{\tau_l}{\tau_c}}+1)}{\frac{\tau_l}{\tau_c}(e^{\frac{\tau_l}{\tau_c}}+1)}\Delta t \quad (6)$$

where $\tau_l = \tau_l(T)$ is the latency time that depends on temperature field and $\tau_c = \tau_c(T,\sigma_0)$ is the characteristic time that depends on temperature and stress field as described in [1]. Hence, an incremental formulation of the kinetics of AAR in terms of $\Delta\xi$ is used in lieu of a total or secant formulation in terms of ξ, as recommended by [19]. However, special care need to be taken for the case of rapid cyclic variation of temperature as it will be shown in section 5.

4.3 Time scaling

Two different time scales are used in the analyses as shown in Figure 4. The "real" time scale is used for implicit transient analyses: $t \in [0, t_{life}]$. As explained before, a different time scale is used for the final explicit analysis: $\tilde{t} \in [0, t_{exp}]$. In order to handle this difference, the time scale factor $\alpha_{sc} = \frac{t_{life}}{t_{exp}}$ is introduced and a change in the stress field variable is done by introducing $\tilde{\sigma}(\tilde{t}) = \sigma(t) = \sigma(\alpha_{sc}\tilde{t})$. Going back to the differential equations describing the multi-physical problem (Eqs. 1 to 6), it is possible to define a new system of equations with regards to the new scaled stress field variable $\tilde{\sigma}$. Hence, it is easy to demonstrate that new "scaled" parameters have to be defined whenever kinetic of the time is involved: $\widetilde{\tau_l} = \frac{\tau_l}{\alpha_{sc}}$, $\widetilde{\tau_c} = \frac{\tau_c}{\alpha_{sc}}$ and $\widetilde{\eta_{ve}} = \frac{\eta_{ve}}{\alpha_{sc}}$ respectively for AAR and creep strains.

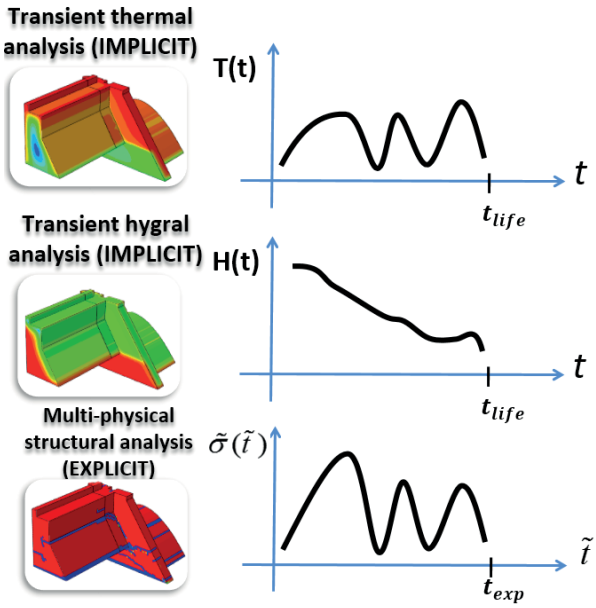

Figure 4: Difference in time scales

4.4 Incremental formulation

Due to the small increment size, the equation 6 can be rewritten as: $\dot{\xi}(t,T,\sigma_0) = f(t,T,\sigma_0)$.

A first possible and simple incremental formulation is to compute the rate of advancement of AAR $\dot{\xi}$ at each increment, knowing the value of T and stress state σ_0 and then use the integral to compute the total amount of AAR advancement:

$$\xi(t) = \int_0^{t'} f(t',T,\sigma_0)\,dt' \quad (7)$$

This will be called the first incremental formulation. As it will be seen later, this formulation ignores the cyclic variation of T and the high dependency of AAR advancement on it. Figure 5 demonstrates clearly this dependency for three different temperature values and more particularly the effect of temperature change which causes a shift of the rate of expansion to the right or left side. This temperature change can clearly result in an integral value of the rate (Eq. 7) more or less than the value of 1.0 that would be obtained in an isothermal case.

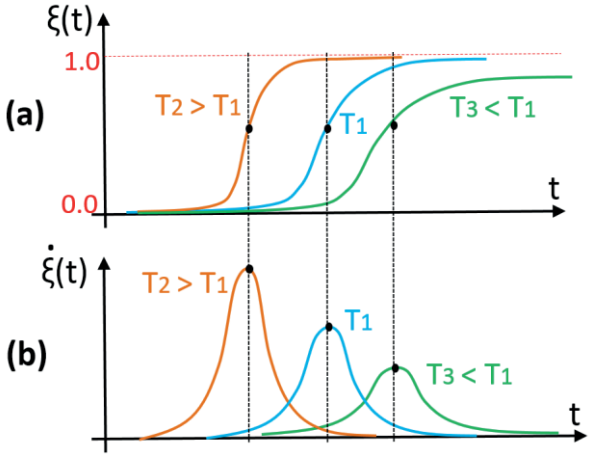

Figure 5: Effect of temperature variation

A new incremental numerical formulation is presented to correctly handle the dependency of the AAR kinetics on the temperature field in case of cyclic temperature variation. It will be called in this paper the second formulation. The idea is to compute at each new step $t_0 + \Delta t$ the increment $d\xi$ of AAR advancement by using the isothermal curve ξ at the previous increment t_0. A fictitious time t_0^* is computed by equating the total AAR advancement between the two isothermal curves at steps t_0 and $t_0 + \Delta t$: $\xi(t_0^*, T(t_0)) = \xi(t_0, T(t_0 + \Delta t))$. This method is shwon schematically in Figure 6 for the case of a sudden temperature drop between the steps t_0 and $t_0 + \Delta t$.

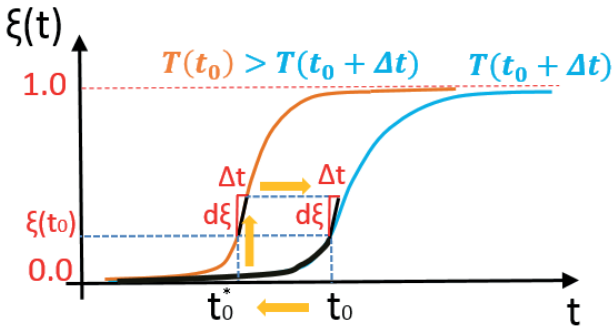

Figure 6: Effect of temperature variation

5 VERIFICATIONS AT MATERIAL LEVEL

A verification example is considered at the material point level of a single cubic element as shown in Figure 7.a. The example is taken from [19] page 53 with the same input data. All the corresponding results are shown in continuous lines in Figures 7.b to 7.c. A cyclic temperature field T(t) is used as input to the multi-physical model. The time span used in the original reference model was 10 years whereas in the explicit model a 0.2 s analysis time is used, the time scale factor is therefore $\alpha_{sc} = 1.58\ 10^9$. The variations of the rate of the AAR $\dot{\xi}(t)$ and the total advancement of the AAR $\xi(t)$, outputs of the multi-physical model, are shown in Figures 7.c and 7.d. The results of the first formulation are represented in black whereas those of the second formulation are red-colored. The results using the first formulation match closely those reported in [19]. The use of the second formulation did not affect greatly the results for this case due to the small amplitude of temperature variation. The conclusions are different when the amplitude is increased from 1^oC to 20^oC which could be the case for example, for hydraulic structures in northern regions of Canada. This case is referred as modified example in Figure 7 and all the corresponding results are in dashed lines. A clear difference is seen in this case between the two formulations (Figures 7c and 7d). It can be demonstrated that the first formulation gives

erroneous results by considering simpler examples of ramped temperatures. The problem occurs more precisely when the temperature change is "rapid" comparatively to the change in the value of the latency time affected by temperature according to Larive laws [2]. The change in latency time τ_l with respect to high or low values of temperatures (represented schematically by horizontal shift in Figure 5b) is also questionable.

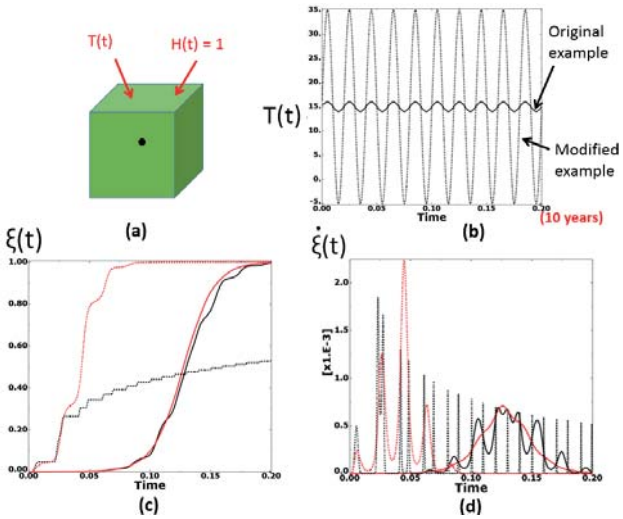

Figure 7: Verification example

6 APPLICATION AT STRUCTURAL LEVEL

The finite element model is shown in Figure 1 along with some dimensions. It is a portion of an existing hydroelectric facility that suffers from AAR. Only portions of the east gravity dam and the spillway are considered. The common structural problem in this case is the abrupt change in the lateral stiffness due to the presence of the hydraulic passage of the spillway. The pier of the spillway is subjected to the thrust action of the dam due to swelling reaction and behaves as a cantilever beam. Fixity condition is assumed at the bottom faces of the model and plain strain conditions are imposed at the lateral vertical faces of the dam and the spillway steed. Hydraulic loads are applied at the upstream faces with the normal closed condition of the spillway gates. The upstream water level is located 1.2 meters below the crest of the dam. The total period of analysis is 100 years. For the explicit model, the period of analysis was set to 10 s. The fundamental mode of the model is around 0.05 s (upstream/downstream bending). It was decided to apply the mechanical loads (gravity and hydrostatic loads) quasi-statically within the first 1 s of the analysis, thus assuming a quasi-linear behaviour of the model in this first interval. The time scale factor is therefore $\alpha_{sc} = 3.15\ 10^8$. As a first approximation, only the AAR strains are considered additionally to the mechanical strains in Eq. 1. All other strains were neglected for this preliminary study. It is important to note here that preliminary data was used and that refinement of the model will be performed in future works. The objective here is to validate the feasibility of the methodology. For the mechanical constitutive law, the main input parameter used was the compressive strength of concrete of the real structure, all other parameters were derived accordingly. Table 1 gives some of the input data required by the STRAINCH and EPM3D subroutines. Latency and characteristic times were chosen in order to achieve 100% of AAR advancement within the analysis period of 100 years, under the computed temperature and relative humidity conditions (see Figure 8).

Table 1: Preliminary input data used for the multi-physical analysis

Property	Symbol	Value	Unit
Mass density	ρ	2350	kg/m3
Young modulus	E	25000	MPa
Compressive strength	f_c'	25.0	MPa
Tensile strength	f_t'	2.3	MPa
Poisson's ratio	ν	0.18	-
Mode I fracture energy	G_F	0.2	kN/m
Long term volumetric AAR strain	$\varepsilon_{v\infty}$	0.002	-

Reference temperature	T_0	20	$\circ C$
Latency time	τ_l	1150	days
Characteristic time	τ_c	350	days
Activation energy for characteristic time	U_c	5400	$\circ K$
Activation energy for latency time	U_L	9400	$\circ K$
Compressive limiting stress for AAR	σ_u	10.0	MPa

Input data required for the implicit transient analyses correspond to normal concrete in northern Canada environmental conditions. They are not exposed herein due to space limitation. Contrarily to most of previous works on hydraulic structures, a variable relative humidity H(t) is considered in this work. Sensitivity studies showed an important impact of this parameter on the damage pattern of the spillway pier. Figure 8 shows the evolution of the relative humidity and temperature fields with respect to virtual time for a given node on the dam. The advancement of the AAR, output of the multi-physical model is also shown in Figure 8.b.

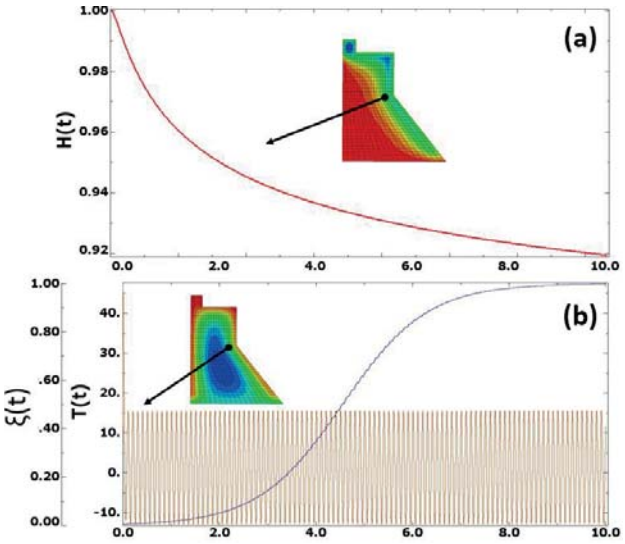

Figure 8: Evolution of: (a) relative humidity field; (b) temperature field and advancement of AAR

Some results are given in the following figures. The computation time for the multi-physical model was around eight hours on a standard quad-core laptop. Figure 9 shows the damage pattern evolution during the total analysis period of 100 years. The cracked elements are blue-colored whereas non-cracked elements are red-colored. A deformation scale factor of 50 is used for the deformed shape, which clearly shows the lateral bending of the pier due to thrust effect from the dam. Figure 10 shows a comparison between the real cracking pattern record (on a 3D virtual geometry) and the damage pattern of the multi-physical model. The similarity between the two is interesting though very preliminary data was used. This similarity was also observed for other hydraulic structural applications under study. As stated before, Figures 9 and 10 show a generalized damage pattern due to AAR, which is believed to cause convergence problems for conventional implicit solvers.

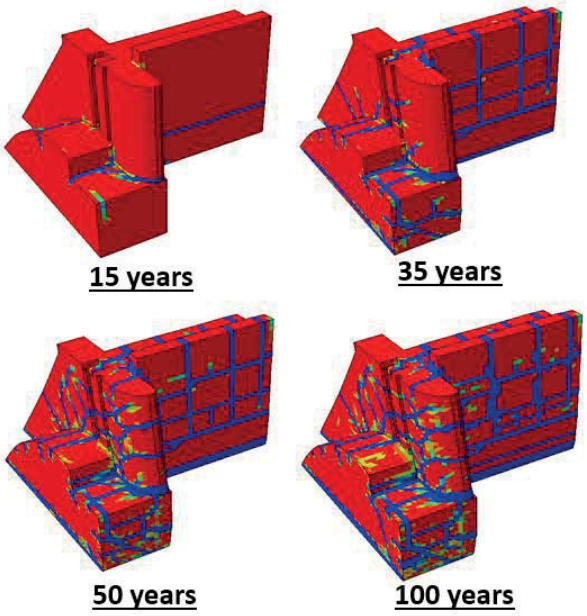

Figure 9: Damage pattern of the multi-physical model

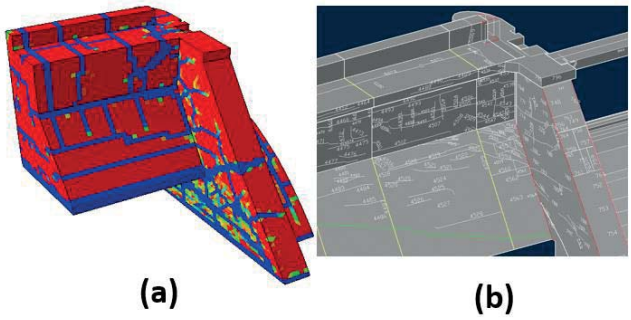

Figure 10: Comparison between: (a) damage pattern in the multi-physical model and (b) real cracking pattern record

7 CONCLUSIONS

A new computational framework is developed in this work for the multi-physical simulation of AAR in concrete structures using the explicit approach. A new scaling technique is developed in order to solve the problem of small time scale of the approach. The effectiveness and feasibility of the overall methodology is demonstrated via a real application example of a hydraulic structure.

REFERENCES

[1] Saouma, V., and Perotti, L. 2006. Constitutive model for alkali aggregate reactions. *ACI Materials Journal*, 103(3):194–202.

[2] Larive, C. 1998. *Apports combinés de l'expérimentation et de la modélisation à la compréhension de l'Alcali-Réaction et de ses effets mécaniques*. Thesis, *LCPC, Paris*.

[3] B. Massicotte, B., Nour, A., Ben Ftima, M., Yildiz, E., and Conciatori, D. 2012. *EPM3D v 2.0, A user-supplied constitutive model for the nonlinear finite element analysis of concrete structures.* Research report, École Polytechnique de Montréal.

[4] Léger, P., Côte, P., and Tinawi, R. (1996). Finite element analysis of concrete swelling due to alkali-aggregate reactions in dams. *Computers&Structures*, 60(4), 601–611.

[5] Ulm, F., Coussy, O., Kefei, L. and Larive, C. 2000. Thermo-chemo-meachanics of asr expansion in concrete structures. *ASCE Journal of Engineering Mechanics*, 126(3): 233–242.

[6] Grimal, E., Sellier, A., LePape, Y. and Bourdarot, E. 2008. Creep, shrinkage, and anisotropic damage in alkali-aggregate reaction swelling mechanism part I: A constitutive model. *ACI Materials Journal*, 105(3).

[7] Comi, C., Fedele, R. and Perego, U. 2009. A chemo-thermo-damage model for the analysis of concrete dams affected by alkali-silica reaction. *Mechanics of Materials*, 41(3): 210–230.

[8] Sellier, A., Bourdarot, E., Multon, S., Cyr, M. and Grimal, E. 2009. Combination of structural monitoring and laboratory tests for assessment of alkali aggregate reaction swelling: application to gate structure dam. *ACI Material Journal*; pp 281–290.

[9] Multon, S. 2004. *Évaluation expérimentale et théorique des effets mécaniques de l'alcali-réaction sur des structures modèles*. Thesis, Université de Marne la Vallée, France.

[10] Ben Ftima, M. 2014. *Utilisation de la méthode des éléments finis non-linéaires pour la conception des structures en béton armé : application aux structures massives*, PhD thesis, École Polytechnique de Montréal, Canada.

[11] Prior, A. 1994. Applications of implicit and explicit finite element techniques to metal forming. *Journal of Materials Processing Technology*, 45(4): 649-656.

[12] Hibbitt, H.D., Karlson, B.I. and Sorensen, E.P. 2016. *ABAQUS version 2016, finite element program*. Hibbitt, Karlson and Sorensen, Providence, R.I., USA.

[13] Ben Ftima, M. and Massicotte, B. 2004. *Introduction du modèle de Bouzaiene et Massicotte (1995) dans ABAQUS (Version 6.4.1 Standard et Explicit)*. Internal Report, École Polytechnique de Montréal, Canada.

[14] Ben Ftima, M. and Massicotte, B. 2015 a. Utilization of nonlinear finite elements for the design and assessment of large concrete

structures, part I: Calibration and Validation. *ASCE Journal of Structural Engineering*, 141, 2015.

[15] Ben Ftima, M. and Massicotte, B. 2015 b. Utilization of nonlinear finite elements for the design and assessment of large concrete structures, part II: Applications. *ASCE Journal of Structural Engineering*, 141, 2015.

[16] Collins, M.P., Bentz, E.C., Quach, P. and Proestos, G. 2015. The challenge of predicting the shear strength of very thick slabs. *Concrete International*, November, 29-37.

[17] Martinola, G., Sadouki, H. and Wittmann, F. 2001. Numerical model for minimizing risk of damage in repair system. *ASCE Journal of materials in civil engineering*, November, 29-37.

[18] Pan, J., Feng, Y., Jin, F. and Zhang, C. 2013. Numerical prediction of swelling in concrete arch dams affected by alkaliaggregate reaction. *European Journal of environmental and Civil Engineering*, 17(4): 231-247.

[19] Saouma, V.E. 2014. *Numerical Modeling of AAR*. CRC Press Taylor & Francis Group, London, UK. (300 pp.)

HAMID

Tome 1: Béton numér'hic

Tome 2: Trans-pores

Tome 3: Crack des fissures

Tome 4: BEEEFUP

La Compil' des publications en 4 tomes

Hamid Sadouki

MCS éditions
2016